TIME INTEGRATION OF EVAPOTRANSPIRATION USING A TWO SOURCE SURFACE ENERGY BALANCE MODEL USING NARR REANALYSIS WEATHER DATA AND SATELLITE BASED METRIC DATA

A Dissertation

Presented in Partial Fulfillment of the Requirements for the

Degree of Doctorate of Philosophy

with a

Major in Civil Engineering

in the

College of Graduate Studies

University of Idaho

by

Ramesh Dhungel

May 2014

Major Professor: Richard G. Allen, Ph.D., P.E.

Authorization to Submit Dissertation

This dissertation of Ramesh Dhungel, submitted for the degree of Doctorate of Philosophy with a Major in Civil Engineering and titled "Time integration of evapotranspiration using a two source surface energy balance model using NARR reanalysis weather data and satellite based METRIC data" has been reviewed in final form. Permission, as indicated by the signatures and dates given below, is now granted to submit final copies to the College of Graduate Studies for approval.

Major Professor: _____ Date: _____
Richard G. Allen, Ph.D.

Committee Members: _____ Date: _____
Fritz R. Fiedler, Ph.D.

_____ Date: _____
Karen Humes, Ph.D.

_____ Date: _____
Ricardo Trezza, Ph.D.

Department Administrator: _____ Date: _____
Richard Nielsen, Ph.D.

Discipline's College Dean: _____ Date: _____
Larry Stauffer, Ph.D.

Final Approval and Acceptance

Dean of the College of Graduate Studies: _____ Date: _____
Jie Chen, Ph.D.

Abstract

A backward averaged two source accelerated numerical solution (BATANS) of surface energy fluxes was developed that utilizes satellite-based Mapping Evapotranspiration at High Resolution using Internalized Calibration (METRIC) data and NARR reanalysis weather data. BATANS simulates surface energy fluxes and surface temperature for surface energy balance when no thermal based surface temperature is available. BATANS was able to partition both satellite based Metric ET at the time of satellite overpass and time-integrate ET between the satellite overpass dates. In addition, BATANS was able to time integrate ET every three hours with the partitioned surface energy fluxes. Partitioned ET on the satellite overpass day was used to estimate soil surface moisture and root zone moisture based on the soil and canopy resistances. Estimated soil moisture at the start of the satellite overpass was used in soil water balance while time integrating ET. A Jarvis type canopy resistance model was utilized by BATANS to estimate the canopy transpiration. An irrigation module was developed to simulate irrigation in agricultural lands when soil moisture falls below a set threshold. The time integrated ET was calibrated and validated using METRIC ET at the start of simulation period and at the next satellite overpass date. Any difference between the simulated and METRIC ET at the end of the simulation period was adjusted linearly assuming that error grows at the same rate over the time. Result showed good agreement between simulated and Metric derived surface energy fluxes and surface temperature in most of the agricultural lands. However, the agreement in the surface temperature was not as good in desert and dry areas. Daily time integrated ET from BATANS between the satellite overpass was also compared to reference ET from AgriMet weather station which showed a reasonable trend. The simple FAO-56 soil water balance model was compared to the advance numerical

solution based Hydrus-1D model to validate the soil water balance between the satellite overpasses. Results showed that both models estimated similar soil water balance.

Acknowledgements

I would like to acknowledge my advisor Dr. Richard G. Allen for his generous support and providing me this opportunity. This work would not have been possible without his help and guidance. I want to acknowledge Dr. Ricardo Trezza and Mr. Clarence Robison for their valuable suggestions. I would like to thank Dr. Fritz Fiedler and Dr. Karen Humes for continuous support and critical review of this thesis. I want to thank Dr. Timothy Link, Mr. Jeremy Greth, Mr. John Stewart, Mr. Carlos Kelly and Mr. Wesley Kelly for their suggestions. I am thankful to Water Resources Department at Kimbelry R & E center and Department of Civil Engineering, University of Idaho. I am also thankful to ARS, Kimberly for providing me working space.

I am grateful to my entire family members, especially my mother Geeta and my late father Chandra Raj for their support and inspiration, sister Rama and her husband Kailash, Rachana and her husband Bikash, and my brother Ranjan and his wife Sweta for their help. Last but not the least; I am thankful to my wife Bibha and my loving son Ayush for supporting me in the entire study period.

Dedication

This dissertation is dedicated to my parents, Geeta and the late Chandra Raj

Table of Contents

List of Figures

List of Tables

Chapter 1: Parameterization of Moisture at the Soil Surface and Root Zone with a Two Source Surface Energy Balance Model using NARR Reanalysis Weather and Satellite Based METRIC Data Set at a Satellite Overpass Time

By

Ramesh Dhungel and Richard G. Allen

Abstract

A backward averaged two source accelerated numerical solution (BATANS) of surface energy balance model was developed to partition evaporation and transpiration coupled with the soil surface and root zone soil moisture for two 2008 satellite overpass dates in southern Idaho. The model was applied to estimate soil surface and canopy temperatures for nearly 500,000 pixels using available climatic NARR reanalysis data and METRIC ET images produced with Landsat. An iterative procedure was used for convergence of the surface energy balance flux with an aerodynamic equation for latent and sensible heat flux. An innovative inversion technique was developed to compute soil moisture at the surface and root zone. This technique utilizes soil surface and canopy resistances that were derived by inverting the two-source model. The model is able to predict the expected small canopy resistances (60-120 s/m) in well-watered, fully-transpiring agricultural fields. The predicted soil moisture was about 0.18-0.22 m^3/m^3 in the root zone for agricultural lands and sagebrush deserts for the May 17, 2008 overpass. This value reflects that the sagebrush desert and grassland were not fully dry on that date. The sensible heat flux between the simulated and METRIC model had R^2 values of about 0.76-0.95 across the 30,000 pixels for the AOIs compared. The combined surface temperature (T_b) had R^2 values of about 0.69-0.89 for different AOIs. The maximum RMSE values for sensible heat flux and temperature were

about 71 W/m^2 and 13 K respectively across the 30,000 pixels. The large temperature difference between the surface of the sagebrush desert and the air above resulted in a sharp temperature profile. This fact, coupled with difficulties in the parameterization of the Jarvis-type (Jarvis, 1976) model for sagebrush desert, caused the simulated combined temperatures for sagebrush desert to be about 10 K lower than the thermal-band-based surface temperature from Landsat.

1.0 Overview

SEBAL (Bastiaanssen et al., 1998), SEBS (Su, 2002), ALEXI (Norman et al., 2003) and METRIC (Allen et al., 2007) are some of the most widely used evapotranspiration (ET) models that utilize remote sensing. These models use the surface energy balance method to compute ET from satellite images taken on overpass dates. Surface temperature is the most important parameter used to complete the surface energy balance. SEBAL and METRIC use the surface temperature derived from the thermal band of Landsat images to compute ET using the surface energy balance method. The traditional SEBAL and METRIC models are single source model. They compute ET from a parameter that includes the bulk contribution of soil and vegetation parameter without partitioning surface energy fluxes. Along with satellite images, SEBAL and METRIC need different roughness parameters and vegetation indices to compute combined ET. These models are able to compute relatively accurate ET values using satellite images from satellite overpass dates without quantifying other complex hydrological parameters, such as soil moisture. But when satellite images are not available, these methods face difficulties.

The main objective of this paper is to estimate soil surface moisture (θ_{sur}) and root zone moisture (θ_{root}) at satellite overpass dates. These soil moisture values are needed to

compute the soil-water balance while extrapolating ET between satellite overpass dates (Dhungel and Allen, 2014b). To accomplish this objective, a two source surface energy balance method is adopted, rather than a single source method. A two source surface energy balance method partitions surface energy fluxes as well as surface temperature into soil and canopy values separately. The success of partitioning surface energy fluxes into soil and canopy values ultimately helps to estimate θ_{sur} and θ_{root}. The challenge is to conduct a complex two source surface energy balance without using thermal band based surface temperature. The primary reason for not using the thermal band based surface temperature at satellite overpass dates is to ascertain whether surface temperature can be computed accurately enough inside the surface energy balance with an iterative process. Secondly, surface temperature from the satellite based thermal band is bulk surface temperature, and difficulties arise when partitioning this bulk surface temperature into soil and canopy portions. Finally, the success of estimating surface temperature inside the surface energy balance is important when extrapolating ET between the satellite overpass dates, when no satellite images and thermal based surface temperatures are available.

Some of the earlier studies that used two source surface energy balances were Raupach, 1989, McNaughton and Van den Hurk, 1995, Shuttleworth and Wallace, 1985, Choudhury and Monteith, 1988, Norman et al., 1995, Li et al., 2005 and Colaizzi et al., 2012. BATANS estimates soil surface temperature (T_s) and canopy temperature (T_c) iteratively using the aerodynamic equation of the sensible heat fluxes for soil and canopy portions, respectively. A two-source surface energy balance aerodynamic equation is adopted, as opposed to the widely used Penman-Monteith ET equation. This is because the Penman-Monteith equation collapses to surface energy balance when the slope of saturated vapor

pressure (Δ) is computed using actual surface temperatures. The aerodynamic method requires resistances and temperatures of different sources and sinks to compute latent and sensible heat fluxes. In this study, relatively accurate METRIC ET data are utilized as a boundary condition of ET for partitioning surface energy fluxes at satellite overpass. To complete the surface energy balance, North American Regional Reanalysis (NARR) weather based meteorological data is used along with METRIC ET.

Soil moisture can be measured directly in the field, but difficulties arise when these kinds of data are needed in greater spatial and temporal resolution. Limited research had been done to estimate θ_{root} with remote sensing technology. Current remote sensing technology does not have the capability to measure soil moisture directly at the rooting zone. Scott et al., 2003 used evaporative fraction to estimate θ_{root} using the SEBAL model in different parts of the world. Das et al., 2006 assimilated aircraft-based remotely-sensed surface soil moisture into a distributed Soil–Water–Atmosphere–Plant (SWAP) model to compute θ_{root}. Albergel et al., 2008 used near-surface soil moisture to estimate θ_{root} using an exponential filter. Microwave technology is most commonly used to estimate soil moisture for a few centimeters below the ground surface. Most of these above mentioned methods have different limitations; a new innovative method was adopted to accomplish the objective of this study.

Soil moisture at surface (θ_{sur}) and θ_{root} are measures of resistances at the soil surface and canopy respectively, which are needed while computing ET with the aerodynamic method. In this developed procedure, θ_{sur} and θ_{root} are computed from a two-source surface energy balance by an indirect inversion of resistances. In general, soil moisture is used to estimate r_{ss} and r_{sc} because soil moisture can be measured directly and quantified easily. In this approach, resistances are initially estimated based on partitioned METRIC ET, and soil

moistures are back calculated based on these partitioned resistances.

2.0 Methodology

This procedure is accomplished in three phases.

1) **Phase 1 Inversion:** METRIC generated ET is partitioned into soil surface evaporation (E_{ss}) and transpiration (T) to calculate soil surface moisture (θ_{sur}) and root zone moisture (θ_{root}) at the satellite overpass time. The partitioning of ET and calculation of θ_{sur} and θ_{root} at the satellite overpass time is achieved by a two-step procedure.
    a) **Step 1:** Estimate T and θ_{root} by assuming the soil is completely dry and letting the canopy transpire fully, if the conditions allow, using surface energy balance. In this process, a minimum value of r_{sc} limits the maximum T while inverting Jarvis-type function.
    b) **Step 2:** Back calculate T, E_{ss} and θ_{sur} with an estimated r_{sc} that defines T of Step 1.
2) **Phase 2 Interpolation:** Estimate θ_{sur} and θ_{root} every three hours, using the θ_{sur} and θ_{root} values of Phase 1 as an initial starting point of the simulation of soil-water balance, in order to extrapolate ET between two satellites overpass dates with METRIC and NARR (Mesinger, F., and Coauthors, 2006) reanalysis data sets.
3) **Phase 3 Correction:** Correct simulated ET using METRIC ET at the next satellite passing date.

This paper discusses Phase 1. Phase 2 and 3, which involve the extrapolation and correction of ET, will be discussed in Dhungel and Allen, 2014b. There are two models (Step 1 and Step 2) associated with Phase 1.

2.1 Model Description

BATANS applies the Monin-Obukhov similarity theory from canopy height to

blending height over all contained 30 m pixels. Meteorological conditions, such as surface roughness, atmospheric stability and heterogeneity length scales, govern the blending height (Essery et al., 2003), which often varies between 50 m and 100 m above the surface (Wieringa, 1986; Mason, 1988 ; Raupach and Finnigan, 1995). SEBAL (Bastiaanssen et al., 1998) and METRIC (Allen et al., 2007) use 200 m as the blending height, while ALEXI (Norman et al., 2003) uses 50 m. Suñén et al., 2012 tested a 30-60 m blending height. This study uses a blending height of 30 m because of the availability of different meteorological data from NARR reanalysis.

Aerodynamic resistance from substrate to canopy height (r_{as}) is computed for the soil portion and aerodynamic resistance from canopy height to blending height (r_{ah}) is computed for the soil and canopy portion combined (fig. 1.1). The H is computed separately for the soil and canopy portions and blended together at the $d + z_{om}$ height (fig. 1.1). This model is similar to a parallel or patch model proposed by Norman et al, 1995, as no intermediate temperature is computed at height $d + z_{om}$. In this study, both T_s and T_c are computed iteratively within the surface energy balance, so introduction of another intermediate temperature, as in a series model, creates difficulties in the solution and convergence of the two source surface energy balance. It is assumed that use of bulk sensible heat flux for computing r_{ah} with a combined stability correction will carry the properties of the soil and canopy portions. Table 1.1 shows the fluxes, parameters, and boundary conditions that are applied in the model.

Table 1.1. Fluxes, parameters, variables, and boundary conditions used in BATANS

Parameters	**Symbol**	**Min**	**Max**	**Units**
Incoming solar radiation	$R_{S\downarrow}$	-	-	W/m^2
Incoming longwave radiation	$R_{L\downarrow}$	-	-	W/m^2
Net Radiation	R_n	-	-	W/m^2
Measurement height (Blending height)	Z	-	-	m
Stability correction parameter	ψ	-	-	-
Soil surface temperature	T_s	265	350	K
Canopy temperature	T_c	265	350	K
Combined temperature	T_b	265	350	K
Air Temperature at blending height	T_a	-	-	K
Wind speed at blending height	u_z	-	-	m/s
Specific humidity at blending height	q_a	-	-	kg/kg
Soil surface evaporation	E_{ss}	0.0001	1.4 Ref_ET	mm/hr
Canopy transpiration	T	0.0001	1.4 Ref_ET	mm/hr
Combined (bulk) Sensible heat flux	H	-200	500	W/m^2
Sensible heat flux for soil portion	H_s	-200	500	W/m^2
Sensible heat flux for canopy portion	H_c	-200	500	W/m^2
Ground heat flux	G	-200	700	W/m^2
Latent heat flux for soil	(LE_s)	-	-	W/m^2
Latent heat flux for canopy	(LE_c)	-	-	W/m^2
Friction velocity	u*	0.01	500	m/s
Aerodynamic resistance from canopy height to blending height	r_{ah}	1	500	s/m
Normalized difference vegetation Index (NDVI) for fraction of cover	NDVI	0.15	0.8	-
Albedo soil	α_s	0.15	0.28	-
Albedo canopy	α_c	0.15	0.24	-
Leaf area index	LAI	f_c	LAI_{METRIC}	-
Single area leaf equivalent bulk stomatal resistance	r_l	80	5000	s/m
Fraction of vegetation cover	f_c	0.05	1	-
Mean boundary layer resistance per unit area of vegetation	r_b	0	-	s/m
Roughness length of momentum	z_{om}	0.01	-	m
Roughness length of heat	z_{oh}	-	-	m
Minimum roughness length	z_{os}	0.01	-	m
Bulk boundary layer resistance of the vegetative elements in the canopy	r_{ac}	0	5000	s/m
Canopy resistance	r_{sc}	0	5000	s/m
Soil surface resistance	r_{ss}	35	5000	s/m
Aerodynamic resistance between the substrate and canopy height $(d + z_{om})$	r_{as}	-	-	s/m
Height of canopy	h_c	-	-	m
Manageable allowable depletion	MAD	0	0.95	-
Relative Evaporative fraction (ET_rF)	Rel_ETrF	0.55	1	-
Soil moisture at surface	θ_{sur}	-	-	m^3/m^3
Soil moisture at root zone	θ_{root}	-	-	m^3/m^3
Available water fraction	AWF	0	1	-
Soil moisture at wilting point	θ_{wilt}	-	-	m^3/m^3
Soil moisture at field capacity	θ_{fc}	-	-	m^3/m^3

Figure 1.1 shows the model for H with the parameters of surface energy balance fluxes.

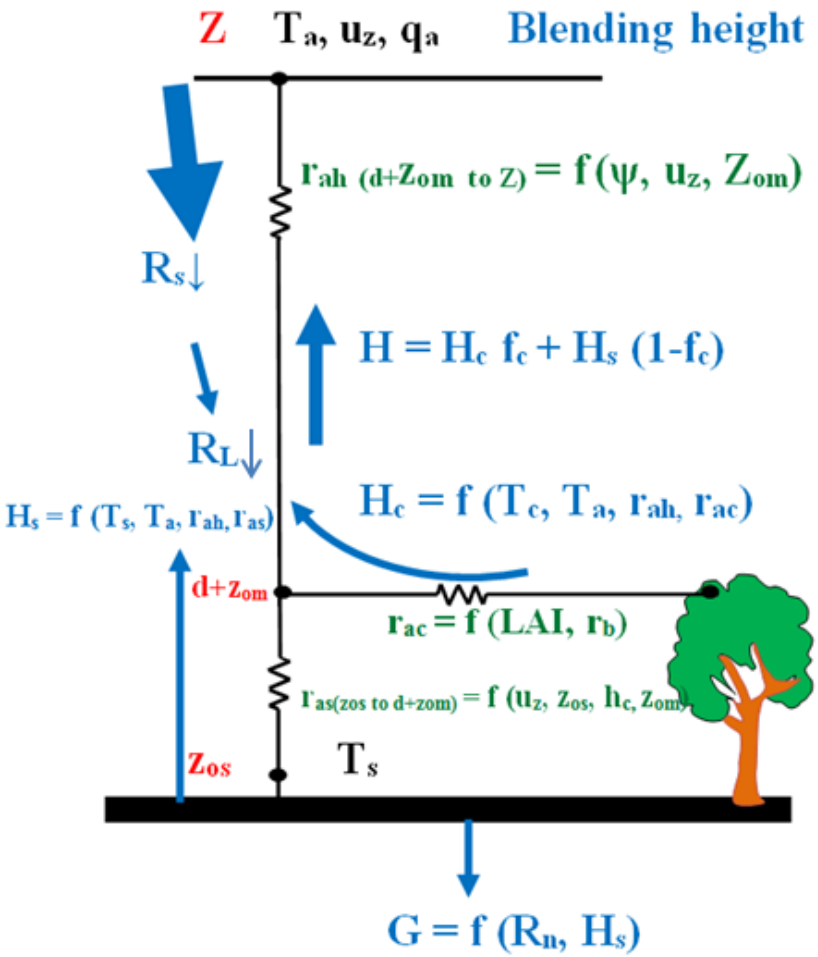

Fig. 1.1. Two source model for sensible heat flux (H) with major components of surface energy balance and resistances

Equations 1 and 2 show the aerodynamic equations for sensible heat flux of the soil (H_s) and canopy (H_c) portions, respectively.

$$H_s = \frac{\rho_a c_p (T_s - T_a)}{r_{ah} + r_{as}} \quad (1)$$

$$H_c = \frac{\rho_a c_p (T_c - T_a)}{r_{ah} + r_{ac}} \quad (2)$$

where T_a is the air temperature at blending height (K), ρ_a is the atmospheric density (kg/m^3), and c_p is the specific heat capacity of moist air (J/kg K). r_{as} is computed according to the Shuttleworth and Wallace, 1985 procedure shown in the appendix-A. The value of r_{ac} is small

compared to the other resistances, whose computation procedures are shown in the appendix-A. z_{om} is the roughness length of momentum (m) and z_{os} is the minimum roughness length above the surface which is assigned as 0.01 m for land surface. Figure 1.2 shows the two source model for latent heat flux (LE). Equations (3), (4), and (5) show the latent heat flux for soil (LE_s), canopy (LE_c), and water (LE_w) respectively.

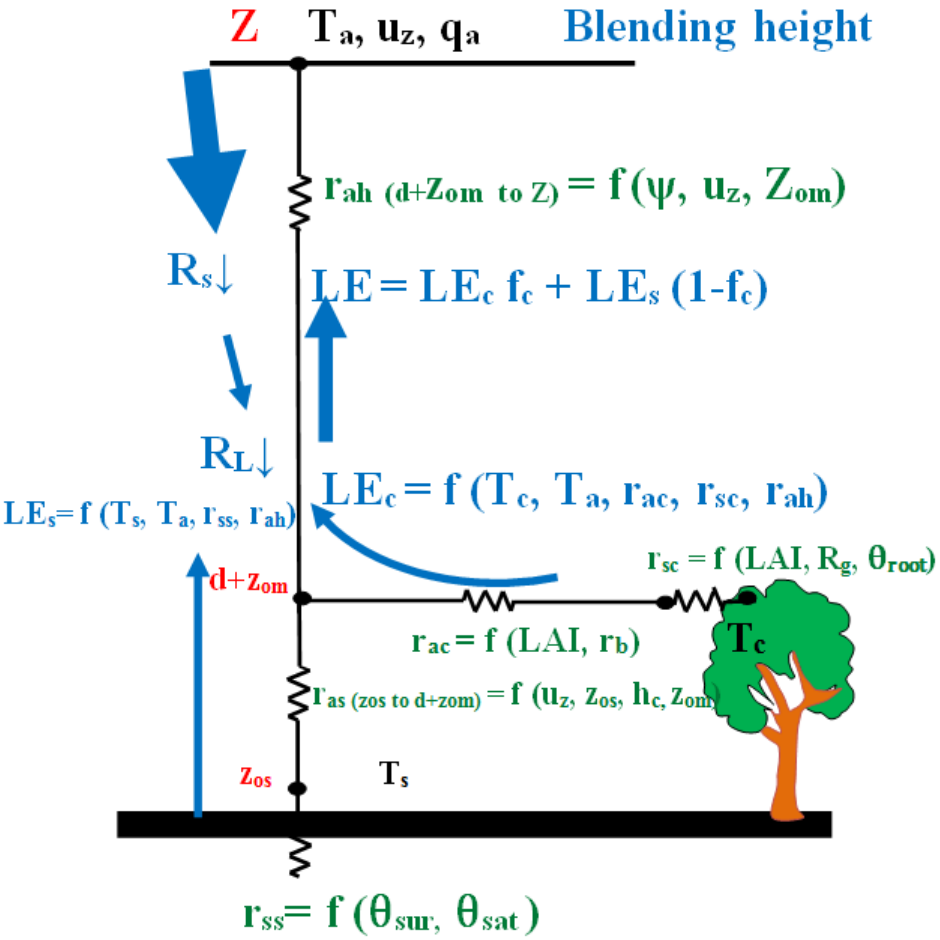

Fig. 1.2. Two source model for latent heat flux (LE) with major components of surface energy balance and resistances

$$LE_s = \frac{C_p \rho_a}{\gamma}\left(\frac{e^o{}_s - e_a}{r_{as} + r_{ah} + r_{rss}}\right) \quad (3)$$

$$LE_c = \frac{C_p \rho_a}{\gamma}\left(\frac{e^o{}_c - e_a}{r_{ac} + r_{ah} + r_{rsc}}\right) \quad (4)$$

$$LE_w = \lambda\, \rho_a \left(\frac{q^o{}_w - q_a}{r_{ah}}\right) \quad (5)$$

where $e^o{}_s$ is the saturation vapor pressure at the soil surface (kPa), $e^o{}_c$ is the saturation vapor pressure of the canopy (kPa), e_a is the actual vapor pressure of air (kPa), $q^o{}_w$ is the specific humidity of the air at saturation (kg/kg), q_a is the actual specific humidity (kg/kg), γ is the psychrometric constant (kPa/^{o}C), and λ is latent heat of vaporization (J/kg).

2.2 Convergence of Surface Energy Balance

The complexity of the solution and convergence of the surface energy balance increases as greater numbers of the parameters and fluxes are uncertain and need to be computed iteratively. Figure 1.3 shows backward averaged two source accelerated numerical solutions (BATANS) of the surface energy balance at satellite overpass time. Separate surface energy balance models, which differ in their method of separating E_{ss} and T from METRIC ET, are used for Step 1 and Step 2. Figure 1.3 is the representative surface energy balance for both steps. Section 2.3 discusses the procedure of partitioning E_{ss} and T in Step 1 and Step 2. Initial T_s and T_c are estimated by inverting equations (1) and (2), assuming neutral conditions. An initial value of H is taken from METRIC ET to start the surface energy balance. In the iterative process, friction velocity (u*), ground heat flux (G), LE, and H are backward averaged and updated during each iteration as a nested loop. Friction velocity (u*), G, LE, and H are assumed to be the most significant parameters for the purpose of convergence. These parameters are monitored during the convergence of surface energy balance and Monin-Obukhov similarity correction. Aerodynamic resistance (r_{ah}) is updated by with new values in each iteration. The convergence criterion for the entire grid is taken to be when 99% of the

total pixels r_{ah} are converged within $\pm$1 s/m.

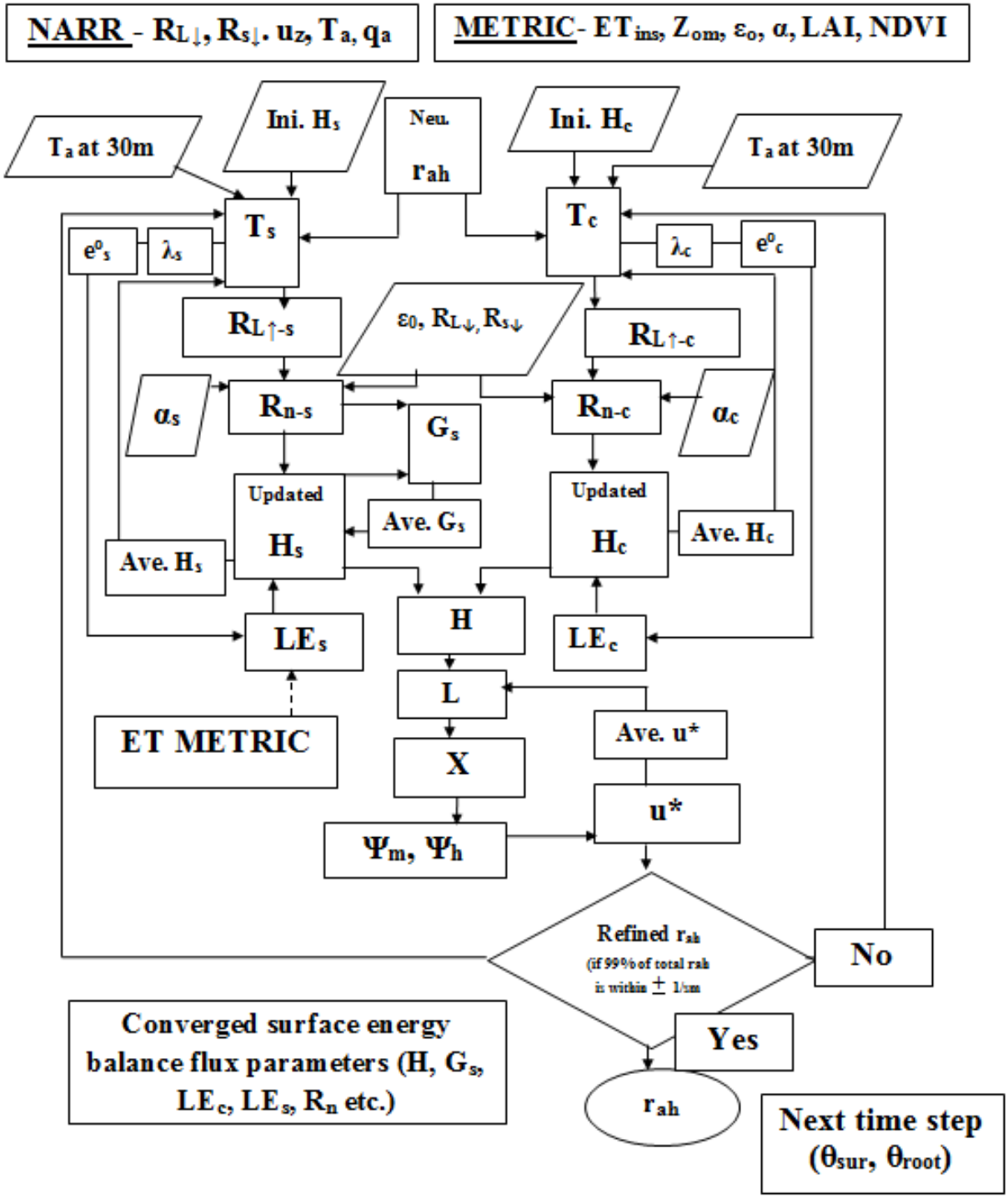

Fig. 1.3. Flowchart of BATANS convergence at satellite overpass time using NARR reanalysis weather data and satellite based METRIC data

After the convergence of the surface energy balance fluxes, θ_{root} is computed outside

the energy balance loop using a Jarvis-type equation (eqn. (12)). Soil moisture at root zone (θ_{root}) represents the soil moisture from the soil surface to the rooting zone which is 2 m for the big tree forest and sage brush desert, and 1 m for rest of the vegetation. Figure 1.4 shows the procedure of inverting a Jarvis-type model to compute θ_{root}. A detailed description of this process is described in Section 2.3.

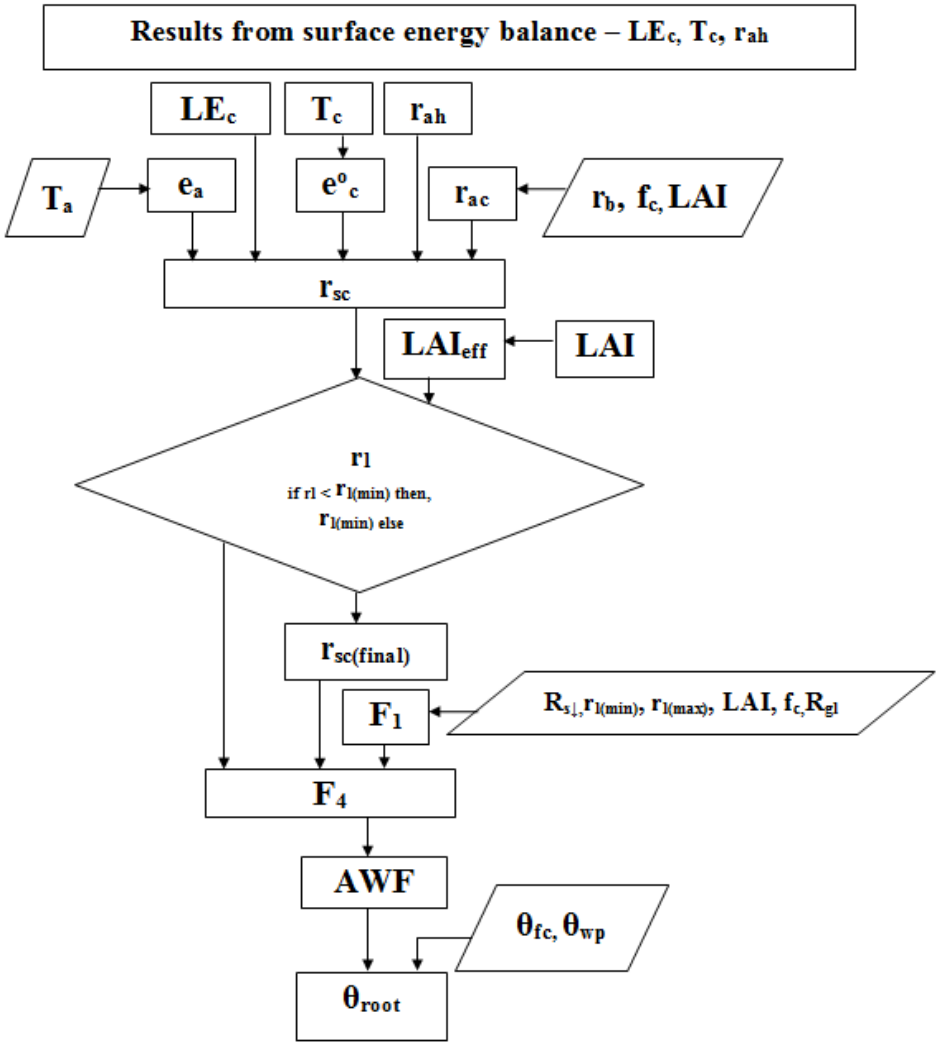

Fig. 1.4. Flowchart of computation soil moisture at root zone (θ_{root}) from Jarvis-type model

2.3 Model Implementation

Step 1: Estimation of T

Soil moisture prior to the satellite overpass date and at the satellite overpass time is not

always available in a large spatial and temporal resolution. In this study, soil surface evaporation (E_{ss}) at the satellite overpass date is computed using eqn. (3), assuming the soil is completely dry. With this assumption, the model can be applied in study areas where no information of the soil moisture is available. Soil surface resistance (r_{ss}) is set at 3000 s/m in Step 1 to make E_{ss} very small. Transpiration (T) is partitioned by subtracting E_{ss} from bulk METRIC ET (ET_{METRIC}) from weighting by f_c (eqn. 6). Transpiration (T) is updated as the fluxes of the surface energy balance are updated and solved iteratively. The initial estimate of T is computed from Equation 6.

$$T = \frac{ET_{METRIC} - (1 - f_c)E_{ss}}{f_c} \tag{6}$$

1. (a) Estimation of r_{sc}

Once r_{ah} is converged from BATANS (fig. 1.3), r_{sc} is computed by inverting aerodynamic equation of LE_c (eqn. 4).

$$r_{sc} = \frac{C_p \rho_a \, (e^o{}_c - e_a)}{\gamma \, LE_c} - r_{ah} \quad - r_{ac} \tag{7}$$

Saturation vapor pressure of the canopy ($e^o{}_c$) is computed during the iteration process using iteratively computed T_c (eqn. 8).

$$e^o{}_c = 0.611 \exp\left(\frac{17.27 \, T_c}{T_c + 237.3}\right) \tag{8}$$

Canopy resistance (r_{sc}) is converted to r_l to check if the minimum value of r_l is smaller than r_{lmin} i.e. 80 s/m. Effective Leaf area index (LAI_{eff}) is computed by using a modified version of Ben-Mehrez et al. (1992) equation of partial canopy. The Ben-Mehrez et al. (1992) is modified to concentrate LAI in a vegetation portion and to separate the soil portion from the vegetation portion (eqn. (9)). While partitioning ET into soil and canopy portion, LAI is weighted by f_c in all the equations that contain LAI.

$$LAI_{eff} = \frac{\frac{LAI}{f_c}}{0.3\frac{LAI}{f_c} + 1.2} \quad (9)$$

r_l is computed using LAI_{eff} as according to Allen et al., 1998 (eqn. (10)) which limits the maximum T in a pixel.

$$r_l = \begin{cases} r_{sc} LAI_{eff} & \text{if } r_{sc} LAI_{eff} \geq r_{l\_min} \\ r_{l\_min} & \text{otherwise} \end{cases} \quad (10)$$

Canopy resistance ($r_{sc)}$ is corrected with r_l if r_l is below r_{l_min} using eqn. (11).

$$r_{sc\_cor} = \frac{r_l}{[LAI_{eff}]} \quad (11)$$

1. (b) Estimation of θ_{root}

Once, r_{sc_cor} is estimated, θ_{root} is computed by inverting a Jarvis-type equation for canopy resistance (eqn. (12), fig. 1.4)). Impacts of different environmental factors (F_1, F_2, F_3, F_4) are considered while computing canopy resistance using a Jarvis-type function. In Equation 12, the impacts of environmental factors associated with solar radiation (F_1) and soil moisture at the root zone (F_4) are solely considered. The influence of other widely used environmental factors like temperature and humidity are not considered, as the temperature is computed iteratively and these two parameters are considered to be relatively consistent between two satellite overpass dates. The weighting coefficients of F_1 and F_4 are limited to 1.

$$r_{sc\_cor} = \frac{r_l}{\frac{LAI}{f_c} F_1 F_4} \quad (12)$$

Equation 13 shows the computation procedure for F_1.

$$F_1 = \frac{\frac{r_{l\,min}}{r_{l\,max}} + f}{1 + f} \quad (13)$$

r_{lmax} and r_{lmin} are maximum and minimum values for r_l respectively (s/m). r_{lmax} and r_{lmin} are taken as 5000 s/m (Kumar et al., 2010) and 80 s/m respectively (Allen et al., 1998). r_{lmin} is

assigned as 80 s/m for all land use classes except for the sagebrush desert and grassland, where a value of 300 s/m is used. This assumes that desert vegetation has higher resistance to transpiration. Parameter f in Jarvis-type model is computed using eqn. (14), where R_{gl} is minimum solar radiation necessary for photosynthesis (T) to occur, and R_g is incident solar radiation.

$$f = 0.55 \frac{R_g}{R_{gl}} \left(\frac{2}{\left(\frac{LAI}{f_c} \right)} \right) \tag{14}$$

The typical values of R_{gl} for irrigated cropland and barren/sparsely vegetated area are 100 and 999 W/m^2 respectively (Kumar et al., 2010). There is a larger uncertainty in the R_{gl} in sagebrush desert. The majority of r_{sc} values computed from the Jarvis-type equation are for the agricultural land and forest environment, and very little research had been done in the desert environment. For agricultural land, minimum solar radiation necessary for photosynthesis (R_{gl}) is assigned as 100 W/m^2 (Stewart, 1988; Alfieri, 2008). A sensitivity analysis is carried out with different set data of $rl_{min,}$ R_{gl}, f_c and LAI to produce a reasonable value of θ_{root} for May, 2008. Sensitivity analysis concluded that a R_{gl} of 100 W/m^2 can be used for all land use classes. Along with other parameters, there is also a greater uncertainty in LAI in sagebrush desert and grasslands. METRIC estimates very small values of LAI (0.05 to 0.11) in sagebrush desert and grassland, while a study conducted in Wyoming showed that LAI is about 0.7 for sagebrush desert (Miller, 1987). Clark and Seyfried, 2001 had also compiled LAI of sagebrush desert, which are from 0.13 to 1.1 at the Reynolds Creek Experimental Watershed in Idaho. After finding the values of R_{gl}, $f_{c,}$ and LAI, F_4 is computed with an inverted Jarvis-type model (eqn. (12)) using Equation 15.

$$F_4 = \frac{r_l}{\frac{LAI}{f_c} F_1 \, r_{sc\_cor}} \tag{15}$$

Available water fraction (AWF) is calculated from θ_{root}, soil moisture at field capacity (θ_{fc}), and soil moisture at wilting point (θ_{wp}) (eqn. 18). Soil moisture at field capacity (θ_{fc}) and θ_{wp} depend on the soil types. Their typical values are 0.36 m^3/m^3 and 0.12 m^3/m^3 (Kumar et al., 2010; Allen et al., 1998) respectively, for a silt loam soil. Studies frequently use the AWF function to represent the F_4 function, creating a very sharp decline of soil moisture (dashed line, fig. 1.5) when sufficient soil moisture is available for transpiration. The F_4 curve acquires a concave down shape to mimic soil moisture at the root zone, as well as the stress level of vegetation (fig. 1.5). The F_4 function decreases slowly within moisture ranges from θ_{fc} and certain threshold moisture content (θ_t) and decreases sharply from θ_t to θ_{wp}. Vegetation has very little to no stress in the soil moisture range from θ_{fc} to certain threshold moisture content (θ_t). The plant can transpire at a reference rate in these ranges of soil moisture if atmospheric conditions are favorable. When θ_{root} decreases to θ_t, vegetation is no longer able to transpire in a reference rate. A detailed discussion of the computational procedure of θ_t is carried out in next paper (paper 2).

To compute the F_4 function for a Jarvis-type equation, a logistic growth model is frequently used in agricultural modeling (France and Thornley, 1984; Anderson et al., 2007). This relationship preserves the characteristics of T with respect to θ_{root} (fig. 1.5), assuming it is independent of the soil types and textures. Using Equations 15 and 16, θ_{root} is computed by the following procedure:

$$F_4 = \left[\frac{1}{1 + 20 \, e^{(-8 \, AWF)}}\right] \tag{16}$$

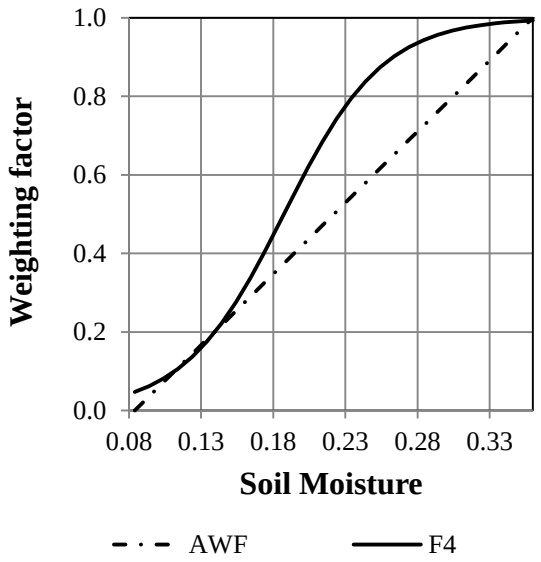

Fig. 1.5. F_4 function for Jarvis-type model developed from available water fraction (AWF) where θ_{wp} = 0.12 m^3/m^3 and θ_{fc} = 0.36 m^3/m^3

After computing F_4 (eqn. 15) from the Jarvis-type equation, AWF is computed by inverting the logistic growth model (eqn. 17).

$$\mathrm{AWF} = -0.125 \log\left[\frac{1-\mathrm{F_4}}{20\mathrm{F_4}}\right] \tag{17}$$

Finally, θ_{root} (eqn. 19) is computed by inverting the AWF equation (eqn. 18).

$$\mathrm{AWF} = \frac{\theta_{\mathrm{root}} - \theta_{\mathrm{wp}}}{\theta_{\mathrm{fc}} - \theta_{\mathrm{wp}}} \tag{18}$$

$$\theta_{\mathrm{root}} = \mathrm{AWF}\left(\theta_{\mathrm{fc}} - \theta_{\mathrm{wp}}\right) + \theta_{\mathrm{wp}} \tag{19}$$

Step 2: Estimation of E_{ss_cor}

In Step 2, an iterative process is carried out for the convergence of r_{ah} using different set of the surface energy balance model. In this step, transpiration (T_{cor}) is refined by r_{sc_cor} from Step 1 using the aerodynamic equation for vegetation (eqn. 4). With a better estimation of T_{cor}, soil surface evaporation is corrected (E_{ss_cor}) simultaneously in this step (eqn. 20).

$$E_{ss\_cor} = \frac{ET_{METRIC} - f_c T_{cor}}{1 - f_c} \quad (20)$$

2. (a) Estimation of r_{ss}

Once r_{ah} has converged from the surface energy balance in Step 2, r_{ss_cor} (eqn. 21) is estimated by inverting the aerodynamic equation for LE_s (eqn. 3).

$$r_{ss\_cor} = \frac{C_p \rho_a}{\gamma LE_s}(e^o{}_s - e_a) - (r_{ah} + r_{as}) \quad (21)$$

Saturation vapor pressure at the soil surface ($e^o{}_s$) is computed using T_s iteratively inside the surface energy balance (eqn. 22).

$$e^o{}_s = 0.611 \exp\left(\frac{17.27\, T_s}{T_s + 237.3}\right) \quad (22)$$

2. (b) Estimation of θ_{sur}

In this modeling approach, soil moisture at the surface (θ_{sur}) is estimated by inverting the r_{ss} equation as proposed by Sun, 1982 (eqn. 23). Soil moisture at surface (θ_{sur}) represents the evaporation layer of soil, from the surface to a depth of 10 cm. Equation 23 was developed for a loam soil, which has been extensively used (Mahfouf and Noilhan, 1991, Ács, F., 2003, Yang and Qin, 2009 etc.). Limited research has been done into developing a relationship between θ_{sur} and r_{ss} for all soil types and characteristics. Figure 1.6 shows some of the previously published relationships between θ_{sur} and r_{ss} for different soil types. Soil moisture at the surface (θ_{sur}) may be calculated by inverting Equation 23, but only if the value of r_{ss} is greater than 33.5 s/m. If not, θ_{sur} will become indefinite. Therefore, a minimum value of 35 s/m for r_{ss} is used in the model.

$$r_{ss\_cor} = 3.5\left(\frac{\theta_{sat}}{\theta_{sur}}\right)^{2.3} + 33.5 \quad (23)$$

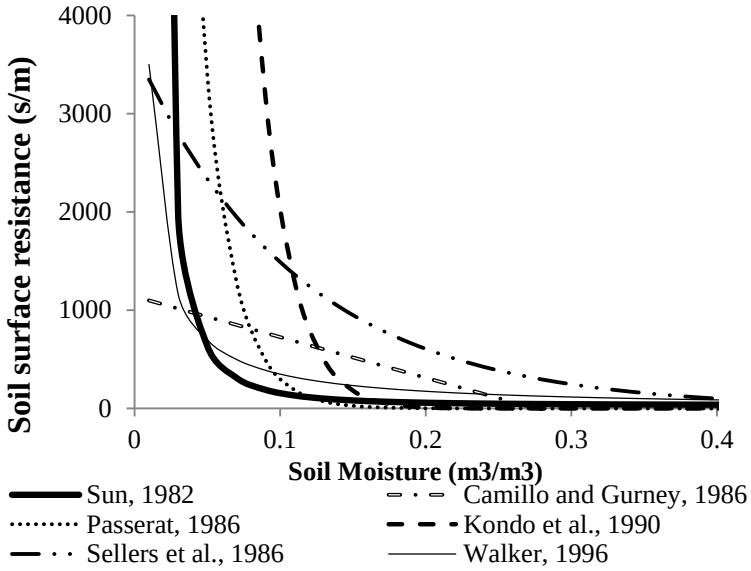

Fig. 1.6. Relationship between soil surface resistance (r_{ss}) and soil surface moisture (θ_{sur}) for different soil types

$$\theta_{sur} = \frac{\theta_{sat}}{\left(\frac{r_{ss\_cor} - 33.5}{3.5}\right)^{\frac{1}{2.3}}} \tag{24}$$

The estimated θ_{sur} in Step 2 and θ_{root} from Step 1 are used in soil water balance while extrapolating ET in Phase 2.

3.0 Application

3.1 Data Requirements

A Python based ArcGIS scripting code is used to develop BATANS. Meteorological data needed for BATANS are taken from NARR reanalysis. The NARR reanalysis is a valuable source of climatic gridded data with a high temporal resolution. Data are collected every 3 hours, but many data are not usable because of their coarse spatial resolution. The data acquired from NARR reanalysis are air temperature (T_a) at 30 m, wind speed (u_z) at 30 m, specific humidity (q_a) at 30 m, incoming shortwave ($Rs_{\downarrow}$), incoming long wave radiation ($R_{L\downarrow}$), surface runoff (S_{run}), and precipitation (P). Another set of vegetation indices and roughness data are taken from METRIC (Allen et al., 2007). The data from the METRIC

model are 30 m specific estimates for surface albedo (α), roughness length of momentum transfer (z_{om}), broadband emissivity (ε_o), leaf area index (LAI), and instantaneous hourly ET (ET_{ins}). Broadband emissivity (ε_o) is partitioned into soil and canopy portions. Surface albedo (α) is partitioned into soil and canopy portions based on θ_{sur}. The METRIC model is processed for Landsat image path 39 on May 18, 2000 and June 18, 2008 in southern Idaho. The National Land Cover Database (NLCD) is used to determine the land use classes. The NARR reanalysis data sets have a 32 km grid size, while a METRIC product has a 30 m grid size. The NARR reanalysis values in Table 1.2 correspond to the 32 km grid size that covers the entire study area used in the developed model. Table 1.2 shows data from both NARR reanalysis and METRIC.

Table 1.2. Data from NARR and METRIC at satellite overpass date 05/17/2008 and 06/18/2008

Parameters	**051/17/2008**	**06/18/2008**	**METRIC Data**
Wind speed at 30 m (u_z)	1.2 m/s	3.1 m/s	Surface albedo (α)
Air temperature at 30 m (T_a)	295.4 K	294.8 K	Roughness length of momentum transfer (z_{om})
Incoming shortwave radiation ($Rs_{\downarrow}$)	974 W/m^2	988 W/m^2	Broadband emissivity (ε_o)
Incoming longwave radiation ($R_{L\downarrow}$)	303 W/m^2	310 W/m^2	Leaf area index (LAI)
Precipitation (P)	0 mm/3 hr	0 mm/3 hr	Instantaneous hourly ET (ET_{ins})
Surface runoff (S_{run})	0 mm/3 hr	0 mm/3 hr	
Specific humidity at 30 m (q_a)	0.0041 kg/kg	0.0052 kg/kg	

Most of the soil in the area of interest consists of silt loam and loam soil (Westermann and Tindall, 1995; City of American Falls, 2009). The Soil Survey Geographic (SSURGO) database is used to acquire information about this soil.

3.2 Study Area

The test project area is in southern Idaho, near American Falls, and includes irrigated agriculture, desert, and water bodies. In this study, a small 500 km^2 AOI is chosen for

convergence and computational efficiency (fig. 1.7). The blue square box in fig. 1.7 is a NARR pixel which overlays the entire AOI. Landsat path 39 images from May, 17, 2008 overlay the NARR pixel. A single pixel of NARR has an area of 1024 km^2, which is an area equivalent to that of about 1 million Landsat image pixels.

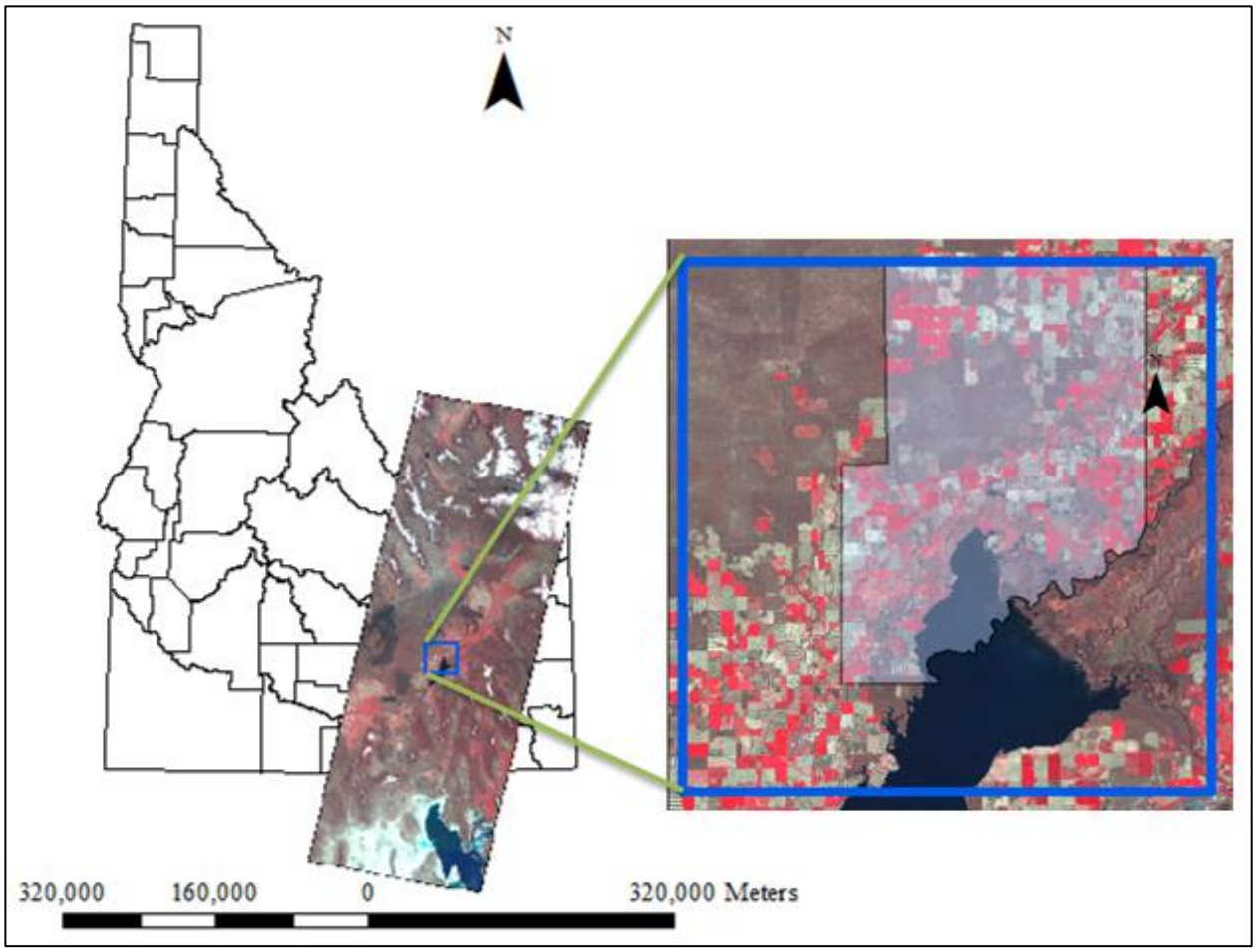

Fig. 1.7. Study area near American Falls, ID overlaying NARR pixel and a Landsat path 39 image for May 17, 2008

4.0 Results and Discussions

In this section, discussion is carried out for combined and partitioned surface energy fluxes separately. Surface energy fluxes computed from Step 2 are final flux values of the Phase 1 inversion process. Likewise, canopy resistance (r_{sc}) and θ_{root} from Step 1 are final values of the Phase 1 inversion process. Some of the statistical parameters suggested by

Legates and McCabe, 1999 are used to evaluate model performance. These statistical parameters are coefficients of determination (R^2), root mean square error (RMSE), mean absolute error (MAE), modified index of agreement (d_i), and coefficient of efficiency (E). These parameters are summarized in table 1.4.

Before analyzing θ_{sur} and θ_{root}, it is important to evaluate the surface energy balance fluxes and parameters. Simulated results from BATANS are compared to METRIC results after adjusting and combining f_c values. To evaluate model performance, three areas of interest (AOI) are chosen in different land use classes. They are the upper right agricultural land (URA AOI), bottom left agricultural land (BLA AOI) and middle sagebrush desert and grassland (MD AOI), as shown in Figure 1.8a. Figures 1.8a, 1.8b and 1.8c show ET, NDVI and f_c respectively at one satellite overpass date (05/17/2008). Dark blue colors (NDVI from 0.68 to 0.8) in fig. 1.8a indicate that the center pivots are transpiring nearly at reference rate, while sagebrush desert and grassland (NDVI from 0.19 to 0.27) have ET from about 0.1 to 0.25 mm/hr.

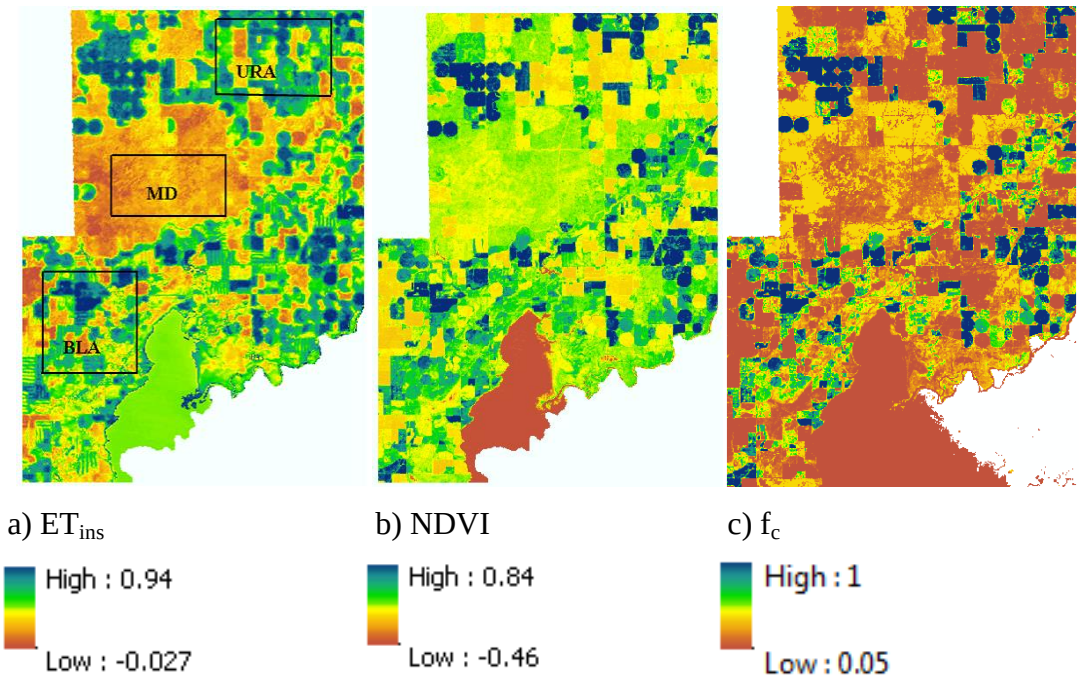

Fig. 1.8. METRIC generated instantaneous ET (mm/hr), NDVI, and f_c on 05/17/2008 in southern Idaho, near American Falls

4.1 Combined Result for 05/17/2008 satellite overpass

In this section, combined surface energy fluxes and results are discussed.

4.1.1 Sensible Heat Flux (H)

Figure 1.9 shows METRIC and simulated H at the satellite overpass time. Simulated H results match closely with METRIC H in visual inspection. The mean of H for the METRIC data is about 159 W/m^2 with a standard deviation of 43 W/m^2, while simulated H is about 183 W/m^2 with a standard deviation of 53.4 W/m^2 for URA AOI. The difference in the mean is about 25 W/m^2, which is less than 1 standard deviation from METRIC H. For BLA AOI, the mean is about 167 W/m^2 with a standard deviation of 49 W/m^2, while simulated H is 212 W/m^2 with a standard deviation of 62 W/m^2. In BLA AOI, the difference in mean increased compared to URA AOI, and is about 45 W/m^2. For MD AOI, which consists of sagebrush desert and grassland, the METRIC mean is about 269 W/m^2 with a standard

deviation of 15 W/m^2, while simulated H is 323 W/m^2 with a standard deviation of 20 W/m^2. Table 1.4 compiles the statistical parameters between simulated H and METRIC H values.

Simulated H is systemically greater than the METRIC results in all three AOIs. It is difficult to determine a consistent primary cause of these differences, as simulated H is from a combination of soil and canopy portions. One of the reasons of systemically greater H from BATANS is that G is consistently smaller. There are biases in the computation of fluxes in the surface energy balance approach, as LE is only as accurate as the combined estimates of R_n, G, and H (Allen et al., 2013). These flux biases are one possible reason for the differences between simulated and METRIC H. Use of the standard aerodynamic equation in the sparse canopy, where the surface-air temperature difference is made proportional to the sensible heat flux by means of an aerodynamic resistance, can produce a 50% error in surface energy balance (Choudhury et al., 1986, Stewart et al., 1989).

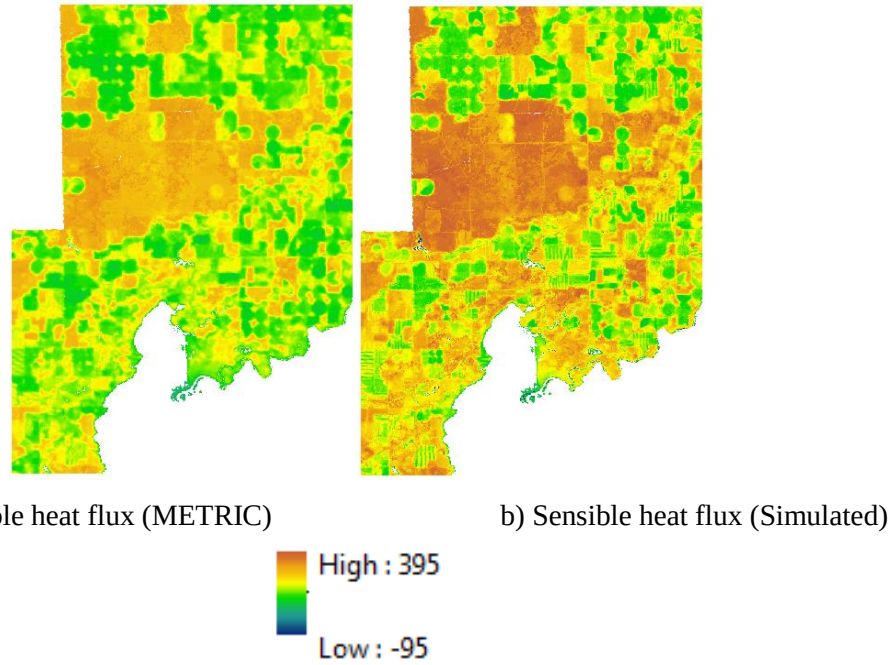

a) Sensible heat flux (METRIC) b) Sensible heat flux (Simulated)

Fig. 1.9. Comparison of METRIC to simulated bulk sensible heat flux (W/m^2) on 05/17/2008 in southern Idaho, near American Falls

Table 1.3 shows the results of the surface energy balance fluxes of a particular pixel

for different land use classes and conditions. The simulated H matches closely to METRIC H in all four agricultural pixels except for desert and grasslands, where simulated H is noticeably larger than METRIC H (table 1.3).

Table 1.3. Surface energy fluxes for different land use classes and conditions on 05/17/2008

Models	Coordinates (m)	NLCD Land use classes	fc	T_b (K)	H (W/m^2)	G (W/m^2)	Rn (W/m^2)	LE (W/m^2)
METRIC	2612097,	82	0.063	305	119	96	641	426
Simulated	1330202			305	92	84	603	427
METRIC	2606520,	52	0.28	321	278	111	519	130
Simulated	1327977			309	332	77	543	131
METRIC	2604335,	71	0.28	324	275	110	546	114
Simulated	1326667			312	331	76	526	115
METRIC	2600245,	82	0.85	301	98	43	600	459
Simulated	1328521			305	130	11	599	458
METRIC	2609171,	82	0.05	320	250	100	445	95
Simulated	1333273			314	284	105	485	95
METRIC	2612312,	82	0.24	309	155	90	603	358
Simulated	1329483			305	161	64	585	359

Figure 1.10 shows a scatter plot of about 30,000 METRIC H and simulated H pixels sampled on two different dates. The coefficients of determination (R^2) between the METRIC H and simulated H are about 0.79 and 0.77 for URA AOI and BLA AOI respectively (table 1.4) for 05/17/2008. Most of the points in both scatter plots are above the 1:1 line, indicating that simulated H is larger than METRIC H (fig. 1.10a and 1.10b). Root mean square errors (RMSEs) are about 34 W/m^2, 54 W/m^2 and 55 W/m^2 for URA, BLA, and MD AOIs, respectively, for 05/17/2008. On 06/18/2008, R^2 increased to 0.95 and 0.90 for URA and BLA AOIs respectively (fig. 1.10c and 1.10d). The increased R^2 on 06/18/2008 is probably because of increased convergence of surface energy fluxes with higher wind speed.

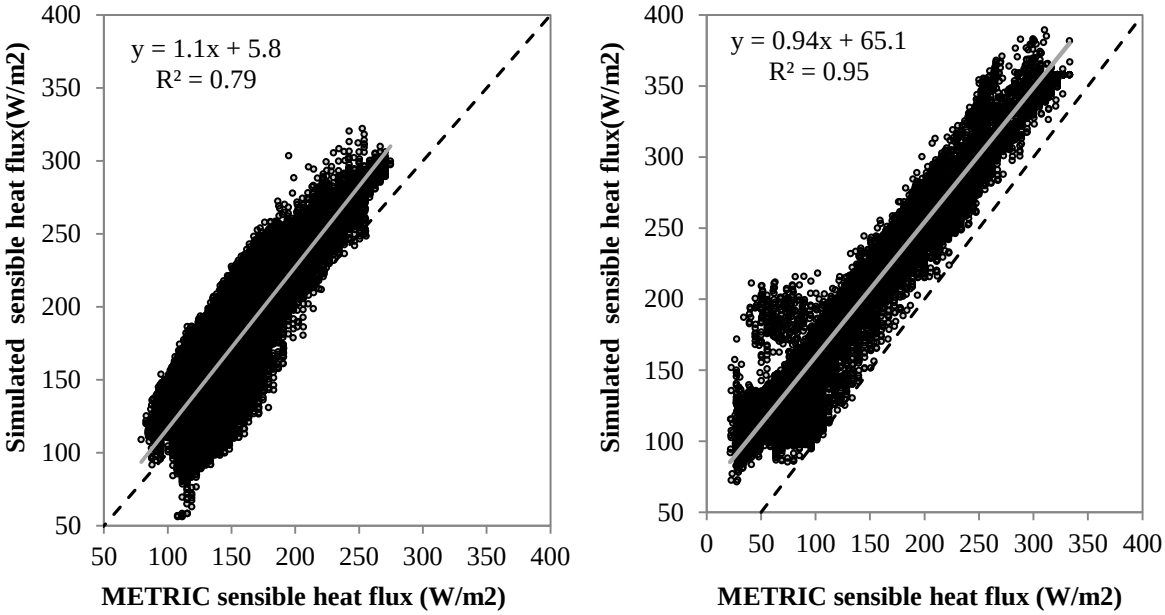

a) URA 05/17/2008 c) URA 06/18/2008

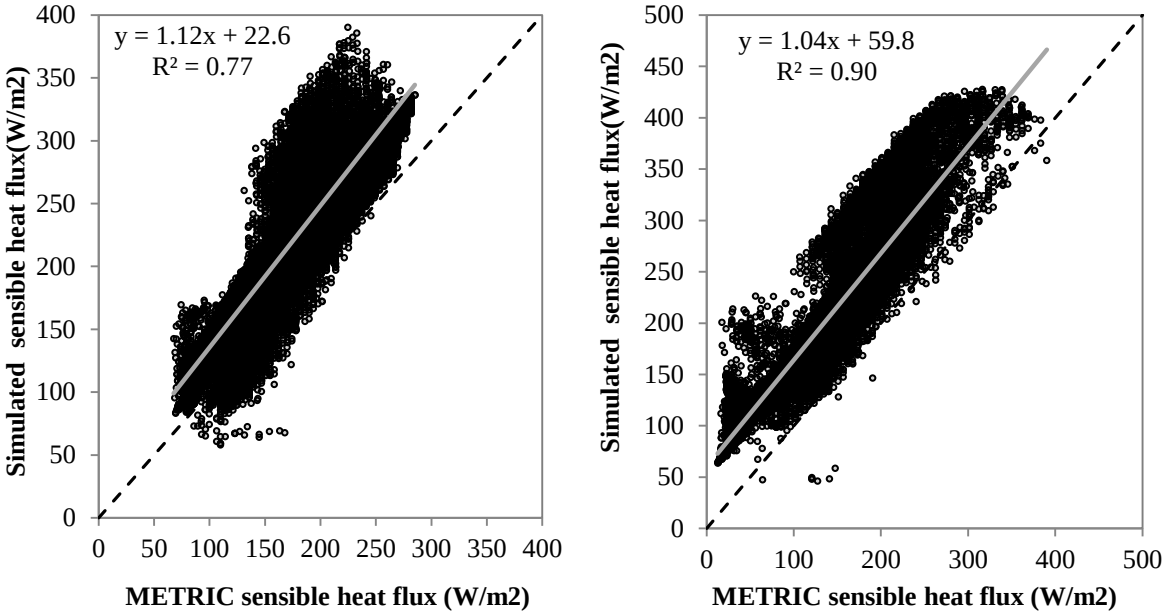

b) BLA 05/17/2008 d) BLA 06/18/2008

Fig. 1.10. Scatter plots of METRIC and simulated sensible heat flux (W/m^2) for URA and BLA AOIs on 05/17/2008 and 06/18/2008 in southern Idaho, near American Falls

4.1.2 Ground Heat Flux (G)

Figure 1.11 shows comparisons between METRIC and simulated G. BATANS

assumes that there is no G in the vegetated portion of the surface energy balance, making G close to zero as f_c approaches 1. The mean G of METRIC data is about 77 W/m^2 with a standard deviation of 17 W/m^2, while for simulated URA AOI data it is 67 W/m^2 with a standard deviation of 27.4 W/m^2 (Table 1.4). For BLA AOI, the mean is about 90 W/m^2 with a standard deviation of 42.3 W/m^2 for METRIC, while for simulated G data it is 60 W/m^2 with a standard deviation of 33.0 W/m^2. For MD AOI, which is comprised of sagebrush desert and grassland, the mean is about 108 W/m^2 with a standard deviation of 6.4 W/m^2 for METRIC data, and for simulated G data it is 77 W/m^2 with a standard deviation of 6.1 W/m^2. Results show that METRIC G and simulated G matched closely with a maximum difference of 30 W/m^2 in all AOIs. The RMSEs are 18 W/m^2, 46 W/m^2, and 30 W/m^2 for URA, BLA, and MD AOIs, respectively. METRIC has larger G (yellowish green) in woody lands (NLCD land class 90), compared to simulation results.

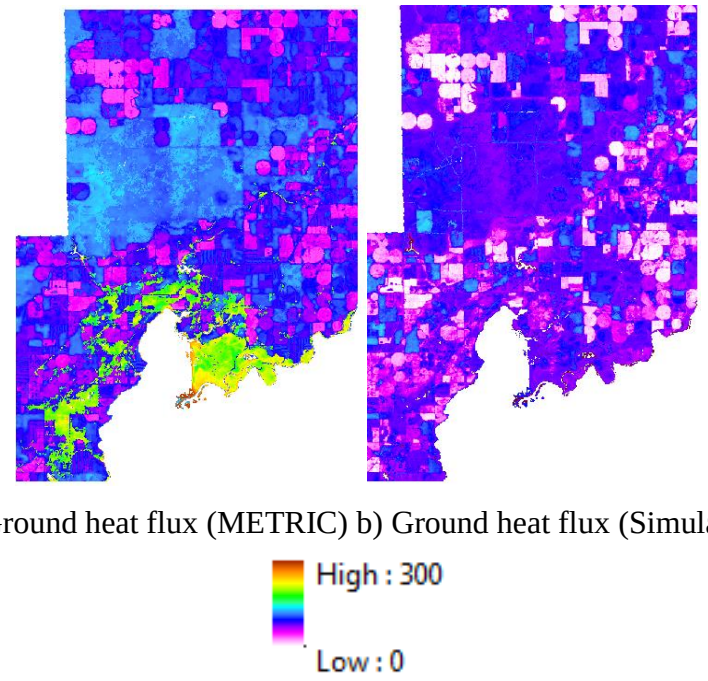

a) Ground heat flux (METRIC) b) Ground heat flux (Simulated)

Fig. 1.11. Comparison of METRIC to simulated ground heat flux (W/m^2) on 05/17/2008 in southern Idaho, near American Falls

4.1.3 Bulk Surface Temperature (T_b)

Figure 1.12 shows simulated bulk surface temperature (T_b) from the BATANS and METRIC models. METRIC temperature is a radiometric surface temperature computed from the thermal band of a Landsat, while simulated bulk surface temperature is the combination of T_c and T_s. For a URA AOI, the mean T_b of METRIC data is about 310 K with a standard deviation of 5.4 K, while the simulated mean is 307 K with a standard deviation of 3.2 K (table 1.4). For BLA AOI, the METRIC mean is 310 K with a standard deviation of 6.1 K, while the simulated mean is 307 K with a standard deviation of 3.1 K. BATANS is able to simulate surface temperature in a manner similar to METRIC in URA and BLA AOIs. For MD AOI, the mean of METRIC is about 322 K with a standard deviation of 1.1 K, while the simulated mean is 311 K with a standard deviation of 1.2 K. MD AOI has a larger difference in T_b compared to other two AOIs.

Table 1.3 showed the temperature comparison of individual pixels for different land use classes. BATANS is able to simulate surface temperatures close to those of METRIC when surface temperature is low, but when surface temperature is high, BATANS has difficulty simulating the resultant steep temperature profile. Numerous factors affect the simulation of surface temperature from the surface energy balance. As mentioned earlier, the surface temperature from METRIC is radiometric temperature, while the simulated temperature is an aerodynamic temperature. These temperatures can differ largely in sparse canopy and semi-arid areas without any bias (Stewart et al., 1993; Colaizzi, et al., 2004; Kustas, 2007). Stewart et al., 1993 discussed the large difference between the radiometric and aerodynamic temperatures in semi-arid areas.

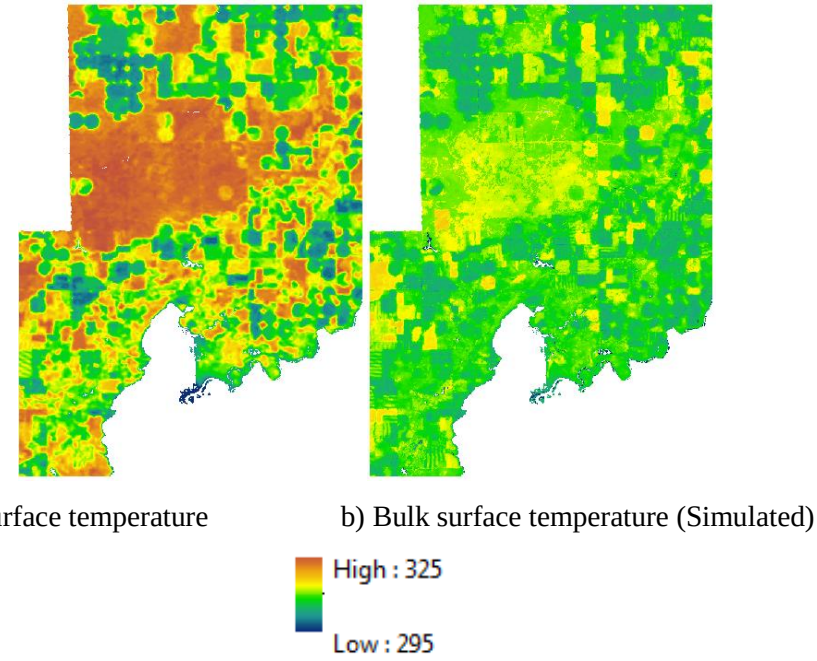

a) METRIC surface temperature b) Bulk surface temperature (Simulated)

Fig. 1.12. Comparison of METRIC to simulated bulk surface temperature (K) on 05/17/2008 in southern Idaho, near American Falls

The R^2 between METRIC and simulated T_b is about 0.74 for the URA AOI and 0.69 for BLA AOI (fig. 1.13) for 05/17/2008 data. The RMSE is about 3.8 K for URA AOI and 5.0 K for BLA AOI for 05/17/2008 data. The majority of points lie below the 1:1 line in both URA AOI and BLA AOI, showing that simulated T_b is smaller than METRIC T_b. For the date 06/18/2008, R^2 increased to 0.89 and 0.81 for URA and BLA AOIs respectively as of H (fig. 1.10, fig 1.13).

Results showed lower temperature in the sagebrush desert and grassland from BATANS, evidencing the difficulty involving in the simulation of temperature in the sparsely vegetated desert using the 32 km NARR reanalysis for 30 m data. Air temperature (T_a) at 30 m is assumed to be same for agricultural land and desert if both lie in same NARR pixel, but the desert environment has a larger temperature difference between surface and air than agricultural land. Thus, the desert has a steeper temperature profile than agricultural land at 30

m, which is the blending height. A number of efforts have been made to match simulated surface temperature to Landsat surface temperature. Sensitivity analysis is conducted by varying attenuation coefficient (n) (Appendix-A, eqn. 6) and exponent (m) on f_c (Appendix-A, eqn. 14b), but none of them are sufficient to increase surface temperature in desert and grasslands.

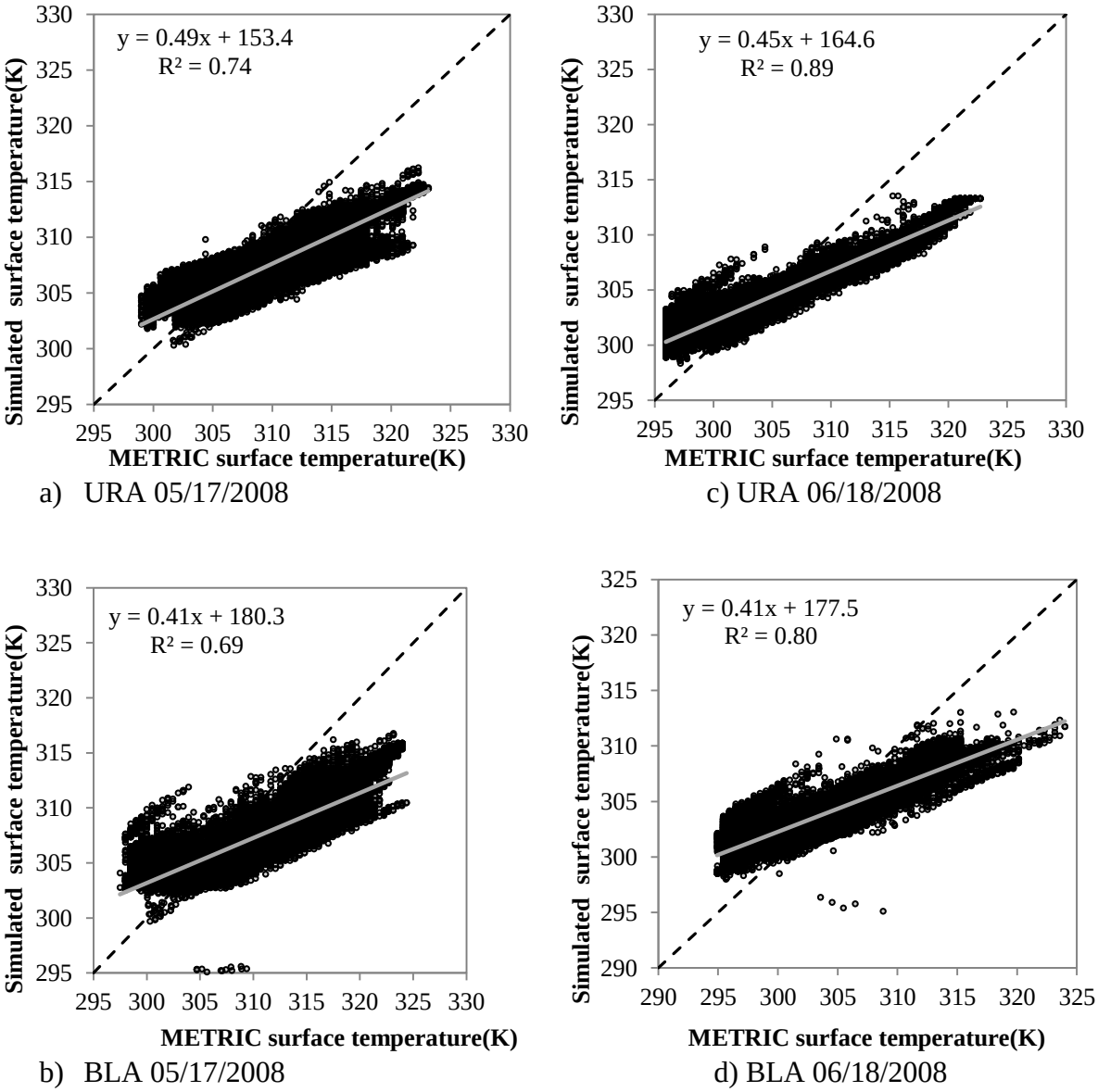

Fig. 1.13. Scatter plot of METRIC and simulated bulk surface temperature (T_b) for URA and BLA AOIs on 05/17/2008 and 06/18/2008 in southern Idaho, near American Falls

Table 1.4 shows the comparison between the METRIC and simulated results for different statistical measures for 05/17/2008. The means of the METRIC and simulation results are similar in most cases, except for some differences in H and T_b in sagebrush desert and grassland. The R^2 is about 0.78 for G in URA AOI and 0.32 for BLA AOI. The R^2 for T_b for MD AOI is 0.23, showing a weak coefficient of determination. The R^2 values for R_n are 0.88, 0.75 and 0.61 for URA, BLA, and MD AOIs respectively. The RMSEs of R_n are 30 W/m^2, 34 W/m^2, and 17 W/m^2 for URA, BLA, and MD AOIs respectively. The coefficient of efficiency (E) has a negative sign in H for BLA and MD AOI; in G for URA AOI, BLA AOI, and MD AOI; in T_b for MD AOI; and in R_n for MD AOI, indicating that the observed mean is a better predictor than the model (Wilcox et al., 1990). Modified index of agreement (d_i) is also very weak in T_b for MAD AOI.

Table 1.4. Statistics of combined surface energy balance fluxes on 05/17/2008

Fluxes	**METRIC**		**Simulated**		R^2	Slope	Intercept	MAE	RMSE (W/m^2)	E	d_i
Combined H	Mean (W/m^2)	Standard deviation (W/m^2)	Mean (W/m^2)	Standard deviation (W/m^2)							
URA AOI	159	43.2	183	53.4	0.78	1.1	5.8	30.2	33.8	0.38	0.64
BLA AOI	167	48.8	212	62	0.76	1.12	22.63	46.4	53.6	-0.20	0.55
MD AOI	269	15.1	323	20.0	0.72	1.06	35.8	54.3	55.4	-11.1	0.19
Combined G	Mean (W/m^2)	Standard deviation (W/m^2)	Mean (W/m^2)	Standard deviation (W/m^2)	R^2	Slope	Intercept	MAE	RMSE (W/m^2)	E	di
URA AOI	77	16.9	67	27.43	0.78	1.4	-44.4	14.2	18.2	-0.16	0.55
BLA AOI	90	42.3	60	33.0	0.32	0.44	20.3	32.0	46.5	-0.2	0.49
MD AOI	108	6.4	77	6.1	0.45	0.61	13.05	29.5	29.9	-21.1	0.15
Combined Temp. (T_b)	Mean (K)	Standard deviation (K)	Mean (K)	Standard deviation (K)	R^2	Slope	Intercept	MAE	RMSE (K)	E	di
URA AOI	310	5.4	307	3.2	0.74	0.49	154.9	3.1	3.8	0.49	0.60
BLA AOI	310	6.1	307	3.1	0.69	0.41	180.4	4.2	5.05	0.32	0.52
MD AOI	322	1.1	311	1.2	0.23	0.49	150	11.3	11.42	-112.2	0.07
Combined R_n	Mean (W/m^2)	Standard deviation (W/m^2)	Mean (W/m^2)	Standard deviation (W/m^2)	R^2	Slope	Intercept	MAE	RMSE (W/m^2)	E	di
URA AOI	544	62.6	558	44.0	0.88	0.62	215.5	25.4	30.4	0.76	0.72
BLA AOI	549	58.2	566	43.2	0.75	0.62	222.8	27.4	33.9	0.66	0.67
MD AOI	502	16.3	531	9.0	0.61	1.5	-282.6	13.2	17.2	-3.15	0.41

A - Upper right agricultural, BLA-Bottom left agricultural land, MD- Middle Desert

4.2 Partitioned Surface Energy Balance Fluxes for 05/17/2008

In the following section, results of the partitioned soil and canopy surface energy balance fluxes and parameters are discussed. Surface energy balance is carried out separately for both soil and canopy portions when computing fluxes and parameters. These partitioned fluxes are later converted to bulk equivalents adjusting the f_c derived from NDVI (Section

4.1).

4.2.1 Soil Surface Evaporation (E_{ss}) and Canopy Transpiration (T)

Figure 1.14 shows the actual contribution of LE_s and LE_c to total LE in terms of mm/hr, after adjusting f_c. Soil surface evaporation (E_{ss}) is low for the agricultural land, where f_c is very high, as its contribution to total ET is negligible. Soil surface evaporation (E_{ss}) is significant where f_c is small and the soil is wet because of recent irrigation or precipitation events. Canopy transpiration (T) is very high where f_c and METRIC ET are high, showing that the crop is fully transpiring. Results confirmed that BATANS is able to partition and simulate reasonable value of E_{ss} and T at satellite overpass.

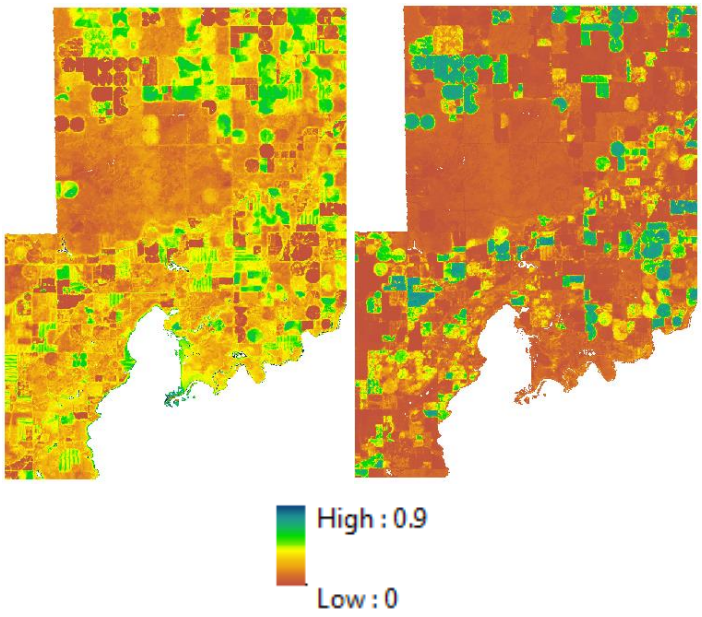

a) Soil evaporation (E_{ss}) b) Canopy transpiration (T)

Fig. 1.14. Estimated soil evaporation (mm/hr) and canopy transpiration (mm/hr) after adjusting for f_c on 05/17/2008 in southern Idaho, near American Falls

4.2.2 Soil Surface Resistance and Canopy Resistance (r_{ss} and r_{sc})

As mentioned in earlier sections, soil surface resistance (r_{ss}) and r_{sc} are computed by inverting the aerodynamic equations of LE_s and LE_c, respectively. Canopy resistance (r_{sc}) has low values in fully covered agricultural lands and higher values where f_c is small, in

sagebrush desert and grassland. Canopy resistance (r_{sc}) in land use classes 81 and 82, which are irrigated agricultural lands, is about 55-120 s/m. The model is able to reproduce a realistic value of r_{sc} in irrigated agricultural land because r_{sc} should be low in irrigated agricultural areas. Likewise, r_{sc} in sagebrush desert and grassland is about 150 to 5000 s/m (fig. 1.15). As discussed earlier, it is assumed that the desert vegetation faces more resistance while transpiring than agricultural land vegetation. Soil surface resistance (r_{ss}) in agricultural land is about 60-5000 s/m, while r_{ss} for sagebrush desert and grasslands is about 500-1000 s/m. When f_c is near 1, r_{ss} is elevated very highly in agricultural land, and E_{ss} makes a very small contribution to total ET.

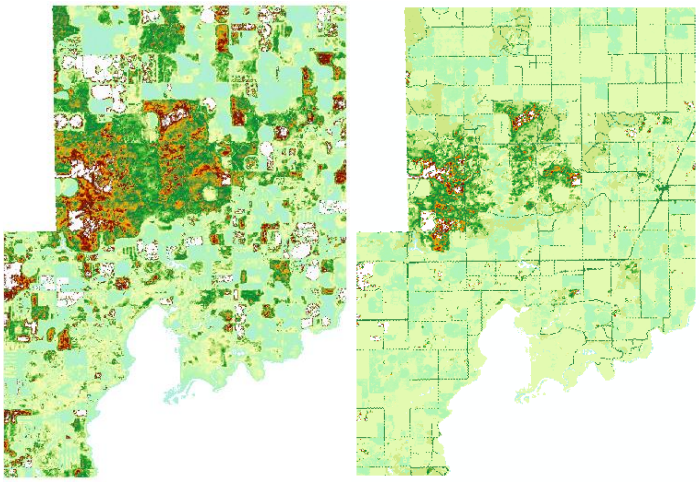

a) Soil surface resistance (r_{ss}) b) Canopy resistance (r_{sc})

Fig. 1.15. Estimated soil surface resistance (s/m) from Step 2 and canopy resistance (s/m) from Step 1 on 05/17/2008 in southern Idaho, near American Falls

4.2.3 Soil Surface and Root Zone Soil Moisture (θ_{sur} and θ_{root})

The complexity of using the Jarvis-type equation in desert increases as R_{gl}, f_c, r_{sc}, rl_{min}, LAI, and physiological characteristics of the plants are more difficult to quantify precisely

than in agricultural land. The developed model estimated θ_{sur} from 0.02 to 0.3 m^3/m^3 in an agricultural land (fig. 1.16). Soil moisture at the surface (θ_{sur}) is high in some areas where f_c is low, indicating recent irrigation or precipitation events. For instance, the developed model is able to capture the recent irrigation or precipitation event with θ_{sur} as 0.23 m^3/m^3 for an agricultural pixel (coordinate of 2602197, 1332720 m, fc ~ 0.3) with an ET of about 0.65 mm/hr. Soil surface moisture (θ_{sur}) is low in the agricultural land where r_{ss} is high. Inverted θ_{sur} for sagebrush desert is small, i.e. 0.01-0.05 m^3/m^3 (fig. 1.16).

The θ_{root} of agricultural land is slightly greater than that of sage brush desert and grassland. The θ_{root} of sagebrush desert is about 0.18-0.20 m^3/m^3, while in agricultural land it is about 0.18-0.22 m^3/m^3. This indicates that soil moisture from the winter snow is still present in the desert. It is important to establish reasonable initial moisture content at the root zone in the desert to preserve the accurate stress level of the desert vegetation, even though desert environments have lower ET than agricultural areas.

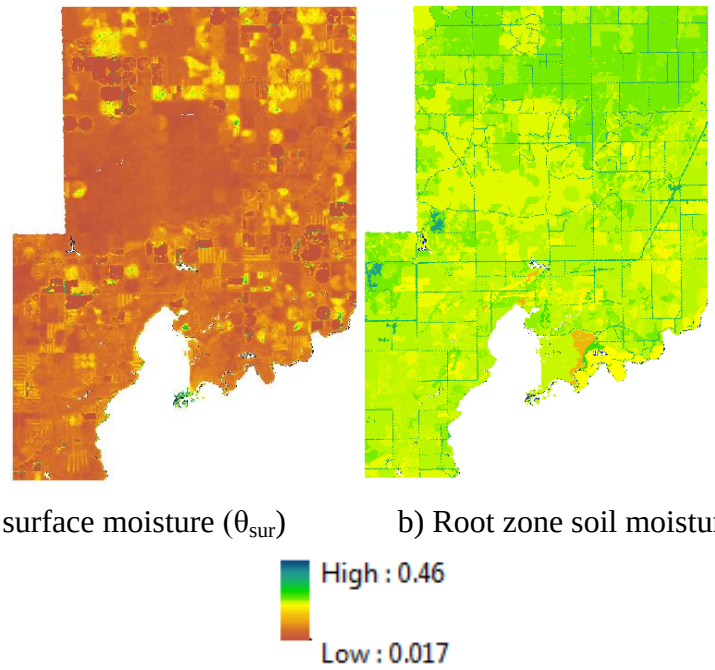

a) Soil surface moisture (θ_{sur}) b) Root zone soil moisture (θ_{root})

Fig. 1.16. Estimated soil moisture at root zone (m^3/m^3) from Step 1 and soil surface moisture (m^3/m^3) from Step 2 on 05/17/2008 in southern Idaho, near American Falls

5.0 Conclusions

BATANS has been developed and applied in southern Idaho to estimate soil moisture of the soil surface layer (θ_{sur}) and root zone (θ_{root}). BATANS was able to simulate the surface temperature and soil moisture at satellite overpass time for two different dates. These data are needed to initialize the soil water balance and plant parameters while extrapolating ET between the two satellite overpass dates. Within the various uncertainties, the simulated and METRIC H, G, and T_b matched closely for agricultural fields but less closely for sagebrush desert and grassland. The coefficient of determination (R^2) between the simulated and METRIC was about 0.51-0.95 for sensible heat flux for different sampled AOI's in the agricultural areas. Root mean square error (RMSE) of sensible heat flux was about 34-71 W/m^2. The error could have been due to a bias in METRIC H, differences in spatial resolution between METRIC and NARR reanalysis data, assumptions in the calculation of G, the computation procedure for $f_{c,}$ and the use of a standard aerodynamic equation for computing

the aerodynamic temperature. The simulated G was systemically smaller than METRIC G, which could be due to the assumption that no G occurred under vegetation. The R^2 between the simulated and METRIC T_b was about 0.69-0.89 for agricultural land, and the maximum RMSE was about 4 K. There was less variation in data when temperature was low. As H, G, and T_b are simultaneously calculated iteratively, any error within the surface energy parameters was, in essence, distributed among all fluxes. At dry areas and desert, the standard aerodynamic equation with an aerodynamic resistance was not able to explain the high radiometric temperature from Landsat, where the simulated surface temperatures were about 10 K lower than those from METRIC. Total surface energy fluxes replicated partitioned surface energy fluxes weighted by f_c. Partitioning of ET not only helped to explicate the surface energy balance fluxes for soil and canopy, but also facilitated the computation of θ_{sur} and θ_{root}. The model was able to simulate high r_{ss} (up to 5000 s/m) in dry areas and low r_{ss} (~ 35 s/m) in wet areas. Canopy resistance (r_{sc}) in well watered transpiring agricultural land was about 40-120 s/m, and it increased up to 5000 s/m in dry areas. The simulated θ_{sur} and θ_{root} had reasonable values for the month of May, 2008, though these values need to be calibrated and validated independently in the field. Both agricultural land and desert had θ_{root} values of about 018 - 0.22 m^3/m^3, showing that some moisture remained in the desert in May. Soil moisture at the surface (θ_{sur}) varied according to soil surface resistance (r_{ss}) at the surface. As this model had been tested within a specific area of interest, future work could be done to expand the concept and apply it to more areas.

References

Ács, F., 2003. A comparative analysis of transpiration and bare soil evaporation. Boundary-Layer Meteorology 109: 139–162.

Albergel, C., Rudiger, C., Pellarin, T., Calvet, J.C., Fritz, N., Froissard, F, Suquia, D., Petitpa, A., Piguet, B. and Martin, E., 2008. From near-surface to root-zone soil moisture using an exponential filter: an assessment of the method based on in-situ observations and model simulations.

Alfieri, J. G., Niyogi, D., Blanken, P.D., Chen, F., LeMone, M. A., Mitchell, K.E, Ek, M.B. and Kumar A., 2008. Estimation of the Minimum Canopy Resistance for Croplands and Grasslands Using Data from the 2002 International H2O Project. 2008 American Meteorological Society.

Allen, R.G., Pereira, L.S., Raes, D., and Smith, M., 1998. Crop Evapotranspiration: Guidelines for Computing Crop Water Requirements. United Nations FAO, Irrig. and Drain. Paper 56. Rome, Italy .300 p.

Allen, R.G., Tasumi, M. and Trezza, R., 2007. Satellite-based energy balance for mapping evapotranspiration with internalized calibration (METRIC) – Model. *ASCE J. Irrigation and Drainage Engineering* 133(4):380-394.

Allen, R.G., Trezza, R., Kilic, A., Tasumi, M. and Li, H., 2013. Sensitivity of Landsat-scale energy balance to aerodynamic variability in mountains and complex terrain. Journal of the American Water Resources Association (Under review). JAWRA-12-0113-P. R1.

Anderson, M.C., Norman, J.M., Mecikalski, J.R., Otkin, J.A. and Kustas, W. P., 2007. A climatological study of evapotranspiration and moisture stress across the continental United States based on thermal remote sensing: 1. Model formulation. Journal of geophysical research, vol. 112, d10117, doi:10.1029/2006jd007506, 2007.

Bastiaanssen, W. G. M., Menentia, M., Feddesb, R.A. and Holtslagc, A. A. M., 1998. A remote sensing surface energy balance algorithm for land (SEBAL). 1. Formulation. Journal of Hydrology 212–213 (1998) 198–212.

Ben Mehrez, M., Taconet, O., Vidal-Madjar, D. and Valencogne, C., 1992. Estimation of stomatal resistance and canopy evaporation during the HAPEX-MOBILHY experiment.Agric For Meteorol, 58, 285-313.

Camillo, P. J. and Gurney, R.J., 1986. A resistance parameter for bare soil evaporation models. Soil Sci. 141, 95–105.

Choudhury, B. J., Reginato, R. J. and Idso, S. B., 1986. An Analysis of Infrared Temperature observations over Wheat and Calculation of Latent Heat Flux', Agric. arid Foresf Mereorol. 37, 75-88.

Choudhury, B. J. and Monteith, J. L., 1988. A four layer model for the heat budget of homogenous land sufaces.Q.J.R. Meteorological Soc.

City of American Falls Comprehensive Plan Planning For Today & Tomorrow 2007-2027 <Accessed 05/10/2013>.

Clark, P.E. and Seyfried, M.S., 2001. Point sampling for leaf area index in sagebrush steppe communities. Journal of Range Management 54(5), September 2001.

Colaizzi, P. D., Kustas, W. P., Anderson, M. C., Agam, N., Tolk, J. A., Evett, S. R., Howell, T. A., Gowda, P. H. and O'Shaughnessy, S. A., 2012. Two-source energy balance

model estimates of evapotranspiration using component and composite surface temperatures. Adv. Water Res.

Colaizzi, P. D., Evett, S. R., Howell, T. A. and Tolk, J. A., 2004. Comparison of aerodynamic and radiometric surface temperature using precision weighing lysimeters. Remote Sensing and Modeling of Ecosystems for Sustainability. Doi: 10.1117/12.559503, pp 215-229.

Dhungel, R. and Allen, R.G., 2014b. Time Integration of Evapotranspiration Using a Two Source Surface Energy Balance Model Using NARR Reanalysis Weather Data and Satellite Based Metric Data. Ph.D. Dissertation, University of Idaho.

Essery, R. L. H., Best, M. J. and Cox, P. M., 2003. Explicit Representation of Subgrid Heterogeneity in a GCM Land Surface Scheme. J. Hydrol., Vol4, No.3, p530-543.

France, J., and Thornley, J. H. M., 1984. Mathematical Models in Agriculture, 335 pp., Butterworths and Co., London.

http://landcover.usgs.gov/classes.php <accessed oct., 2013>.

http://nomads.ncdc.noaa.gov/ <accessed oct., 2011>.

Jarvis, P. G., 1976. The interpretation of the variation in leaf water potential and stomatal conductance found in canopies in the field. Philos Trans R Soc Lond B 273: 593–610.

Kondo, J., Saigusa, N. and Sato, T., 1990. A parameterization of evaporation from bare soil surfaces. J. Appl. Meteor., 29, 385-389.

Kumar, A., Chen, F., Niyogi, D., Alieri, J. G., Ek, M., and Mitchell, K., 2010. Evaluation of a Photosynthesis-Based Canopy Resistance Formulation in the Noah Land-Surface Model. Boundary-Layer Meteorol, DOI 10.1007/s10546-010-9559-z.

Kustas. W. P., Anderson, M. C., Norman, J. M. and Li, F., 2007. Utility of Radiometric–aerodynamic Temperature Relations for Heat Flux Estimation. Boundary-Layer Meteorology 122:1, 167.

Legates, D. R. and McCabe Jr, G. J., 1999. Evaluating the Use of "Goodness-of-Fit" Measures in Hydrologic and Hydroclimatic Model Validation, Water Resour. Res., 35(1), 233–241

Li, F., Kustas, W. P., Prueger, J. H., Neale, C. M. U. and Jackson, T. J., 2005. Utility of remote sensing based two-source energy balance model under low and high vegetation cover conditions. J. Hydrometeorol. 6, 878–891.

Mahfouf, J. F. and Noilhan, J., 1991. Comparative Study of Various Formulations of Evaporation from Bare Soil Using in-situ Data. J. Appl. Meteorol. 30,1354-1365.

Mason, P. J., 1988. The formation of areally-averaged roughness lengths. Quart. J. Roy. Meteor. Soc., 114,399–420.

McNaughton, K. G., and van den Hurk, B. J. J. M., 1995. A ‘Lagrangian’ revision of the resistors in the two-layer model for calculating the energy budget of a plant canopy. Boundary-layer Meteorol. 74:261–288.

Mesinger, F., and Coauthors, 2006. North American Regional Reanalysis. Bull. Amer. Meteor. Soc., 87, 343-360.

Miller, R. F., 1987. Comparison of water use by Artemisia tridentata spp. wyomingensis and Chrysothamnus viscidiflorus spp. Viscidiflorus. TechnicalP aperN o. 8211, Oregon Agricultural Experiment Station National de Polytechnique de Grenoble, France. 205p.

Norman, J. M., Anderson, M. C., Kustas, W. P., French, A. N., Mecikalski, J., Torn, R., Diak, G. R., Schmugge, T. J., and Tanner, B. C. W., 2003. Remote-sensing of surface energy fluxes at 10V-m pixel resolutions. Water Resources Research (submitted for publication).

Norman, J. M., Kustas, W. P. and Humes, K. S., 1995. A two-source approach for estimating soil and vegetation energy fluxes in observations of directional radiometric surface temperature. Agric. For. Meteor.77, 263-293 (1995).

Passerat de Silans, A., 1986. Transferts de masse et de chaleur dans un sol stratifié soumis à une exitation atmosphérique naturelle. Comparaison modèle expérience.Thèse de l'institut.

Repack, M. R., 1989. A practical Lagrangian method for relating concentrations to source distributions in vegetation canopies. Quart. J. R. Meteorol. Soc. 115:609–632.

Raupach, R. R. and Finnigan, J. J., 1995. Scale Issues in Boundary-Layer Meteorology: Surface Energy Balances in Heterogeneous Terrain. Hydro. Proc. 9, 589–612.

Scott, C., Bastiaanssen., W. G. M. and Ahmad., M.D., 2003. Mapping Root Zone Soil Moisture Using Remotely Sensed Optical Imagery. Journal of irrigation and drainage engineering © ASCE.

Sellers, P. J, Mintz, Y., Sud, Y. C. and Dalcher, A., 1986. A Simple Biosphere model (SiB) for use within general circulation models. Journal of the Atmospheric Sciences 43: 505–531.

Shuttleworth, W. J. and Wallace, J. S., 1985. Evaporation from sparse crops-an energy combination theory. Quart. J. R. Met. Soc.

Soil Survey Staff, Natural Resources Conservation Service, United States Department of Agriculture. Soil Survey Geographic (SSURGO) Database for [Power County, ID]. Available online athttp://soildatamart.nrcs.usda.gov. Accessed [10/15/2012].

Stewart, J. B., Shuttleworth, W. J., Blyth, K., and Lloyd, C. D., 1989. FIFE: a comparison between aerodynamic surface temperature and radiometric surface temperature over sparse prairie grass, in 19th Conf. Agric. For. Meteorol., Charleston, SC, March 1989, pp. 144-146.

Stewart, J. B., Kustas, W. P., Humes, K. S., Nichols, W. D., Moran, M. S., and de Bruin, H. A. R., 1994. Sensible heat flux-radiometric surface temperature relationship for eight semiarid areas, J. Appl. Meteorol., 33, 1110-1117.

Stewart, J.B., 1988. Modelling surface conductance of pine forest. Agric For Meteorol 43:19–35

Su, Z., 2002. The Surface Energy Balance System (SEBS) for estimation of turbulent heat fluxes. Hydrol Earth Syst Sci 6(1):85–99 (HESS).

Sun, S.F., 1982. Moisture and heat transport in a soil layer forced by atmospheric conditions, M.S. thesis, Dept. of Civil Engineering, University of Connecticut, 72 pp.

Suñén, M. A., Nordbo, A., Balsamo, G., Beljaars, A. and Mammarella, I., 2013. Representing Land Surface Heterogeneity: Offline Analysis of the Tiling Method. J. Hydrol. 14, 859-867, doi: 10.1175/JHM-D-12-0108.1.

Walker, B. H., and Langridge, J. L., 1996. Modelling plant and soil water dynamics in semi-arid ecosystems with limited site data. Ecol. Model. 87: 153-167.

Westermann, D. T. and Tindall, T. A., 1997. Potassium considerations for southern Idaho soils. In T. A. Tindall and D.T. Westermann (eds.). Proceedings of the Western

Nutrient Management Conference, Vol. 2:172-181. Salt Lake City, UT, March 6-7. Potash and Phosphate Institute, Manhattan, KS.

Wieringa, J., 1986. Roughness-dependent geographical interpolation of surface wind speed averages. Quart. J. Roy. Meteor. Soc., 112, 867–889.

Wilcox, B. P., Rawls, W. J., Brakensiek, D. L., and Wight, J. R., 1990. Predicting runoff from rangeland catchments: A comparison of two models, Water Resour. Res., 26, 2401-2410, 1990.

Yang, K., Chen, Y. Y., and Qin, J., 2009. Some practical notes on the land surface modeling in the Tibetan Plateau, Hydrol. Earth Syst. Sci., 13, 687-701, doi:10.5194/hess-13-687-2009, 2009.

Chapter 2: Time Integration of Evapotranspiration Using a Two Source Surface Energy Balance Model Using NARR Reanalysis Weather Data and Satellite Based Metric Data

By

Ramesh Dhungel and Richard G. Allen

Abstract

A backward averaged two source accelerated numerical solution of the surface energy balance model (BATANS) was developed to extrapolate evapotranspiration (ET) between Landsat satellite overpass dates that were used for the time-integration of METRIC model derived ET images estimations. BATANS was demonstrated with data from southern Idaho over the one month period from 05/17/2008 to 06/18/2008. NARR reanalysis meteorological data were used to calculate surface energy balance fluxes for 3-hour time steps, and the METRIC data set was used to define initial surface characteristics and soil water conditions. Fraction of vegetation cover (f_c) was used to partition surface energy balance fluxes into soil and canopy components, as defined by the normalized difference vegetation index (NDVI). BATANS was able to estimate the surface energy balance fluxes for the 3 hour period between satellite overpasses. This was accomplished by using surface temperature approximated from the energy balance, which utilized NARR weather data. Surface temperature was iteratively computed within the surface energy balance using air temperature at 30 m and an aerodynamic equation for sensible heat flux. Soil surface resistance (r_{ss}) and Jarvis-model-based canopy resistance (r_{sc}) were used to calculate latent heat flux (LE) using an aerodynamic expression. METRIC generated ET was used to initialize the soil water content for the surface and root zone layers at the start of the simulation period, validate the

simulated results from the model at the next satellite overpass date, and make adjustments. The soil moisture sub-model was used to track soil moisture at the surface and root zone, which defined the evaporation and transpiration portions respectively. An irrigation sub-model was developed to factor in irrigation for known irrigated agricultural fields, which is critical when computing ET for heavily irrigated areas. Any mismatch between the simulated and METRIC ET at the following Landsat image date was adjusted over the simulation period with a time-based linear correction to increase the accuracy and reduce computation time. The developed extrapolation model was able to reasonably predict ET from irrigated agricultural lands and desert at the end of the simulation period. Due to the possible mismatch in timing of irrigation events between simulated and actual conditions, BATANS produced lower ET than METRIC in some cases when the NDVI was low. In these cases, potential for evaporation effects following irrigation was high when compared to METRIC estimations at the end of the simulation period. The average simulated and METRIC ET matched closely in all sampled areas of interest (AOI). The R^2 for ET for about 30,000 pixels was about 057 to 0.68 for various AOIs and the RMSE was about 0.03 to 0.17 mm/hour.

1.0 Overview

The motivation for this study was the need for ET maps having high temporal and spatial resolution and availability of weather based gridded data to calculate surface energy fluxes. A two source surface energy balance model has been developed to partition ET which is needed to accurately estimate ET. This allows one to understand the behavior of the land surface processes and the various resistances associated with them. The main objective of the study is to extrapolate ET between the satellite overpass dates using the two source surface energy balance model based on NARR reanalysis weather data and METRIC estimations. The

result of this study can be used to analyze hourly, monthly and seasonal trends in ET, recharge patterns, and other hydrological and crop production aspects. This allows users, ranging from farmers to state agencies, to help manage water rights and drought conditions. The first part of this study (Dhungel and Allen, 2014a) estimated soil moisture and resistances at the satellite overpass time to parameterize the model and to set initial boundary conditions for the second part. In this section (second part), ET is extrapolated between the satellite overpass dates using the soil moisture at the previous satellite overpass date as an initial starting point of the soil water balance. This procedure estimates soil and canopy temperature iteratively, as no gridded thermal sensor based temperature data or satellite images were available.

Past research has explored methods for partitioning ET into soil and canopy portions using a variety of approaches which are generally based on the surface energy balance. In general, these researchers have been limited to point based ET (weather station based meteorological data) or single event based ET (satellite overpass date) because the partitioning of ET requires large quantities of data. Surface energy balance models like traditional SEBAL (Bastiaanssen et al., 1998) and METRIC (Allen et al., 2007) are single source and single event (satellite overpass date) based models which calculate relatively accurate ET at satellite overpass dates. METRIC interpolates daily ET between the satellite overpass dates using a mathematical spline of the fraction of reference evapotranspiration (ET_rF).

Some of the earlier studies are based on two source surface energy balance by Raupach, 1989, McNaughton and Van den Hurk, 1995, Shuttleworth and Wallace, 1985, Choudhury and Monteith, 1988, Norman et al., 1995, Li et al., 2005, and Colaizzi, 2012.

Application of a two source model to partition ET to a larger area such as going from regional to global scales or larger to smaller time steps is more challenging. Methods used to partition ET for gridded data generally include two source surface energy balance models with aerodynamic equations (eqn. 2, 3, 4 and 5) or separate Penman-Monteith type equations for the canopy and soil. Soil and canopy temperature and various resistances from sources and sinks are needed while partitioning ET with these models. Shuttleworth and Wallace, 1985, proposed a two source surface energy balance model, in which Penman Monteith based ET equation, were written separately for soil and vegetation portions with detailed resistances. This method was a cornerstone for two source ET models. Later, Norman et al., 1995 proposed a two source model using the radiometric temperature and the Priestly Taylor equation of ET to partition soil and vegetation. These approaches have been widely used in the remote sensing community. The problem with the Shuttleworth and Wallace procedure for estimating ET is that large quantities of data need to be measured and parameters need to be fitted, which might not be possible in larger spatial applications. The Norman et al., 1995 method has been widely accepted by the remote sensing community, although it also faces many challenges because of its use of the relatively less accurate Priestley Taylor equation. The need for thermal based radiometric surface temperature also creates more requirements that may not always be available.

2.0 Methodology

2.1 Surface Energy Balance Model

A detailed discussion about the two source model implemented in this study has been presented in the first paper (Dhungel and Allen, 2014a). This paper elaborates on the procedure to apply the model to extrapolate ET between the satellite image dates and is good

background for this publication. Table 2.1 shows the fluxes, parameters and boundary conditions of BATANS.

Table 2.1. Fluxes, parameters, variables, and boundary condition used in BATANS

Parameters	**Symbol**	**Min**	**Max**	**Units**
Incoming solar radiation	$R_{S\downarrow}$	-	-	W/m^2
Incoming longwave radiation	$R_{L\downarrow}$	-	-	W/m^2
Net Radiation	R_n	-	-	W/m^2
Measurement height (Blending height)	Z	-	-	m
Stability correction parameter	ψ	-	-	-
Soil surface temperature	T_s	265	350	K
Canopy temperature	T_c	265	350	K
Combined temperature	T_b	265	350	K
Air Temperature at blending height	T_a	-	-	K
Wind speed at blending height	u_z	-	-	m/s
Specific humidity at blending height	q_a	-	-	kg/kg
Soil surface evaporation	E_{ss}	0.0001	1.4 Ref_ET	mm/hr
Canopy transpiration	T	0.0001	1.4 Ref_ET	mm/hr
Combined (bulk) Sensible heat flux	H	-200	500	W/m^2
Sensible heat flux for soil portion	H_s	-200	500	W/m^2
Sensible heat flux for canopy portion	H_c	-200	500	W/m^2
Ground heat flux	G	-200	700	W/m^2
Latent heat flux for soil	(LE_s)	-	-	W/m^2
Latent heat flux for canopy	(LE_c)	-	-	W/m^2
Friction velocity	u*	0.01	500	m/s
Aerodynamic resistance from canopy height to blending height	r_{ah}	1	500	s/m
Normalized difference vegetation Index (NDVI) for fraction of cover	NDVI	0.15	0.8	-
Albedo soil	α_s	0.15	0.28	-
Albedo canopy	α_c	0.15	0.24	-
Leaf area index	LAI	f_c	LAI_{METRIC}	-
Single area leaf equivalent bulk stomatal resistance	r_l	80	5000	s/m
Fraction of vegetation cover	f_c	0.05	1	-
Mean boundary layer resistance per unit area of vegetation	r_b	0	-	s/m
Roughness length of momentum	z_{om}	0.01	-	m
Roughness length of heat	z_{oh}	-	-	m
Minimum roughness length	z_{os}	0.01	-	m
Bulk boundary layer resistance of the vegetative elements in the canopy	r_{ac}	0	5000	s/m
Canopy resistance	r_{sc}	0	5000	s/m
Soil surface resistance	r_{ss}	35	5000	s/m
Aerodynamic resistance between the substrate and canopy height ($d + z_{om}$)	r_{as}	-	-	s/m
Height of canopy	h_c	-	-	m
Manageable allowable depletion	MAD	0	0.95	-
Relative Evaporative fraction (ET_rF)	Rel_ETrF	0.55	1	-
Soil moisture at surface	θ_{sur}	-	-	m^3/m^3
Soil moisture at root zone	θ_{root}	-	-	m^3/m^3
Available water fraction	AWF	0	1	-
Soil moisture at wilting point	θ_{wilt}	-	-	m^3/m^3
Soil moisture at field capacity	θ_{fc}	-	-	m^3/m^3

The sensible heat flux (H) is estimated separately for the soil and canopy portions and then blended together at canopy height as shown in eqn. (1).

$$H = H_c\, f_c + H_s\ (1 - f_c) \tag{1}$$

where f_c is the fraction of vegetation cover, H_c and H_s are sensible heat from vegetation and soil portions (W/m^2) respectively. Equations of sensible heat flux for the soil and canopy are shown in eqn. (2) and eqn. (3) respectively. Soil surface temperature (T_s) and canopy temperature (T_c) are computed by inverting eqn. (2) and (3) respectively.

$$H_s = \frac{\rho_a\, c_p (T_s - T_a)}{r_{ah} + r_{as}} \tag{2}$$

$$H_c = \frac{\rho_a\, c_p (T_c - T_a)}{r_{ah} + r_{ac}} \tag{3}$$

where ρ_a is the atmospheric density (kg/m^3), c_p is the specific heat capacity of moist air (J/kg K), T_a is the air temperature at 30 m taken from NARR reanalysis (K), r_{as} is the aerodynamic resistance between the substrate and canopy height ($d + z_{om}$) (s/m), d is zero plane displacement (m), z_{om} is the roughness length of momentum (m), r_{ah} is the aerodynamic resistance between $d + z_{om}$ and the 30 m blending height for both soil and canopy (s/m), and r_{ac} (s/m) is the bulk boundary layer resistance of the vegetative elements in the canopy (s/m). r_{as} is computed in accord with the Shuttleworth and Wallace, 1985 procedure (Appendix-A), and is assumed to be zero for fully covered agricultural land (f_c =1). Equations (4) and (5) show the latent heat flux equations for the soil and canopy portions respectively.

$$LE_s = \frac{C_p\, \rho_a}{\gamma}\left(\frac{e^o{}_s - e_a}{r_{as} + r_{ah} + r_{ss}}\right) \tag{4}$$

$$LE_c = \frac{C_p\, \rho_a}{\gamma}\left(\frac{e^o{}_c - e_a}{r_{ac} + r_{ah} + r_{sc}}\right) \tag{5}$$

where LE_s and LE_c are sensible heat flux for the soil and canopy portions respectively

(W/m^2), e^o_s is the saturation vapor pressure at the soil surface (kPa), e^o_c is the saturation vapor of the canopy (kPa), e_a is the actual vapor pressure of the air (kPa), r_{ss} is soil surface resistance (s/m), and r_{sc} is canopy resistance (s/m). Equation (6) is total latent heat flux (LE) after adjusting f_c for soil and canopy portions.

$$LE = LE_c\, f_c + LE_s\ (1 - f_c) \tag{6}$$

Figure 2.1 shows the model for H, including the surface energy balance fluxes and parameters to calculate these fluxes. The parameters and fluxes of fig. 2.1 are described in Table 2.1.

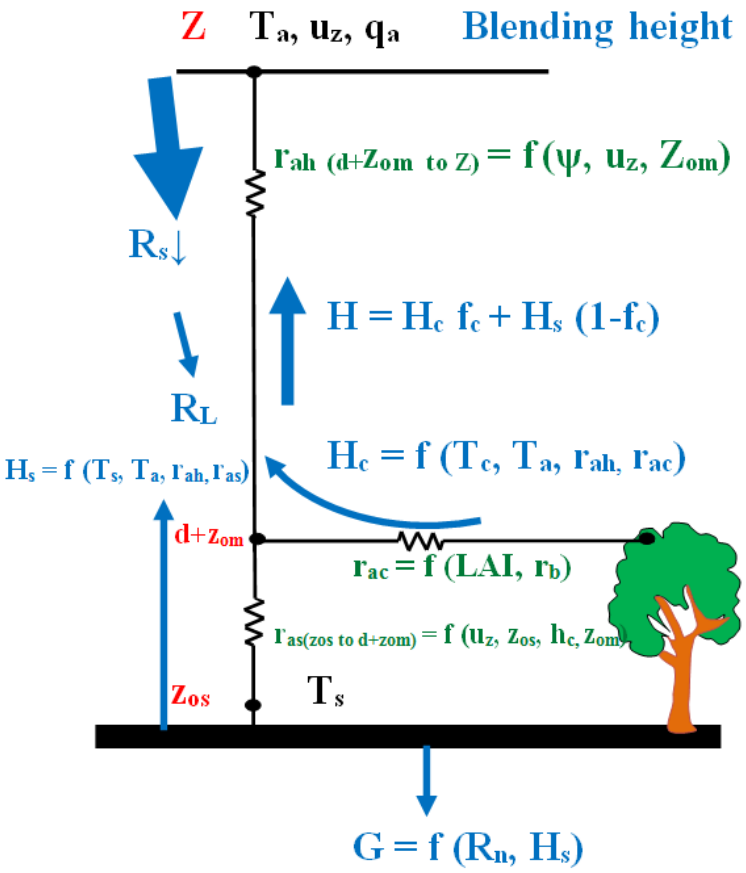

Fig. 2.1. Two source model for sensible heat flux (H) with major components of surface energy balance and resistances

Figure 2.2 is a flowchart of the complete surface energy balance model (BATANS) and a solution technique adopted for the Monin-Obukhov stability correction. The Monin-

Obukhov stability correction is applied to the combined sensible heat flux (H) from canopy height ($d + z_{om}$) to the blending height (z). It is assumed that the combined stability correction maintains the characteristics of the soil and canopy fluxes. A detailed formulation of stability correction is shown in the appendix-A. A blending height of 30 m is used in this study because of the availability of NARR reanalysis weather data at this height. To start the surface energy balance, initial estimates of T_s and T_c are calculated from H_s and H_c from the earlier time steps. Aerodynamic resistance (r_{ah}) is initially computed as neutral atmospheric conditions, and updated during the iteration process. For each time step, a new set of NARR reanalysis weather data and METRIC interpolated data are used to conduct the surface energy balance (fig. 2.2). Soil moisture at the surface (θ_{sur}) and root zone (θ_{root}) are tracked using the soil water balance at each time step. Initial estimates of the surface energy fluxes are updated with new values in each iteration until convergence is reached. A backward averaging of H, G, LE and u* is done to expedite the convergence of the surface energy balance variables. Once r_{ah} is converged within $\pm$ 1 s/m for each pixel and 99% of the total pixels are converged, the model advances to the new time step.

Without incoming shortwave radiation at night, the surface energy balance fluxes, i.e. net radiation (R_n), ground heat flux (G) and H, become negative and stable near the surface boundary layer. This stability causes difficulty in iteratively determining surface temperature due to numerical instability. Therefore, no iteration for convergence is done during night, where a neutral condition is utilized. Situations in which the model converges with negative sensible heat flux during daytime are indicative of advection of energy.

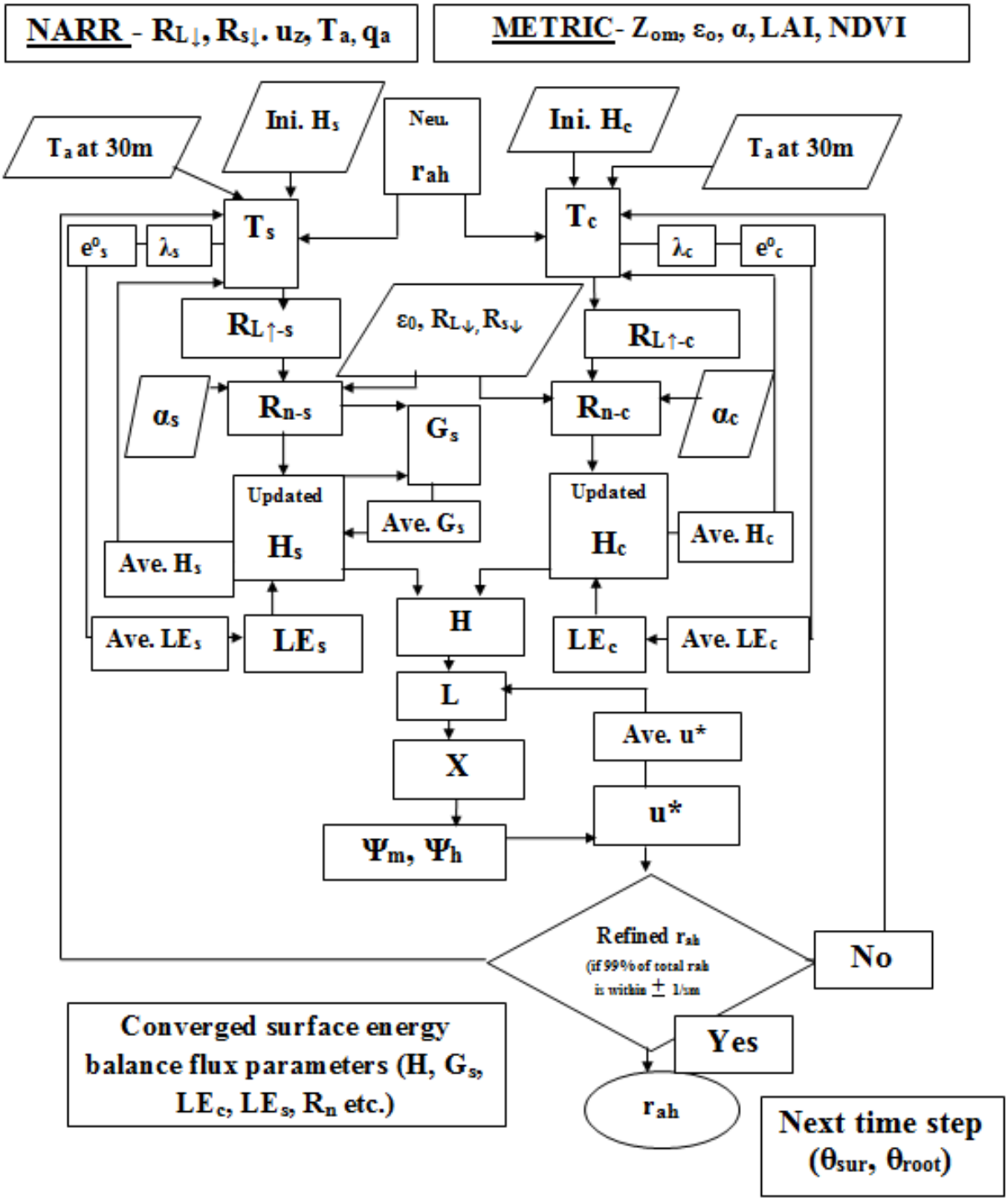

Fig. 2.2. Flowchart of BATANS convergence using NARR reanalysis weather data and satellite based METRIC data

Figure 2.3 shows the process of extrapolation of ET between the satellite overpass dates. ET METRIC at the start of the satellite overpass is used to initialize the soil moisture

estimations at the surface and root zone. ET METRIC at the next satellite overpass date is used to calibrate and validate the model. The ET energy balance is simulated every 3 hours using BATANS.

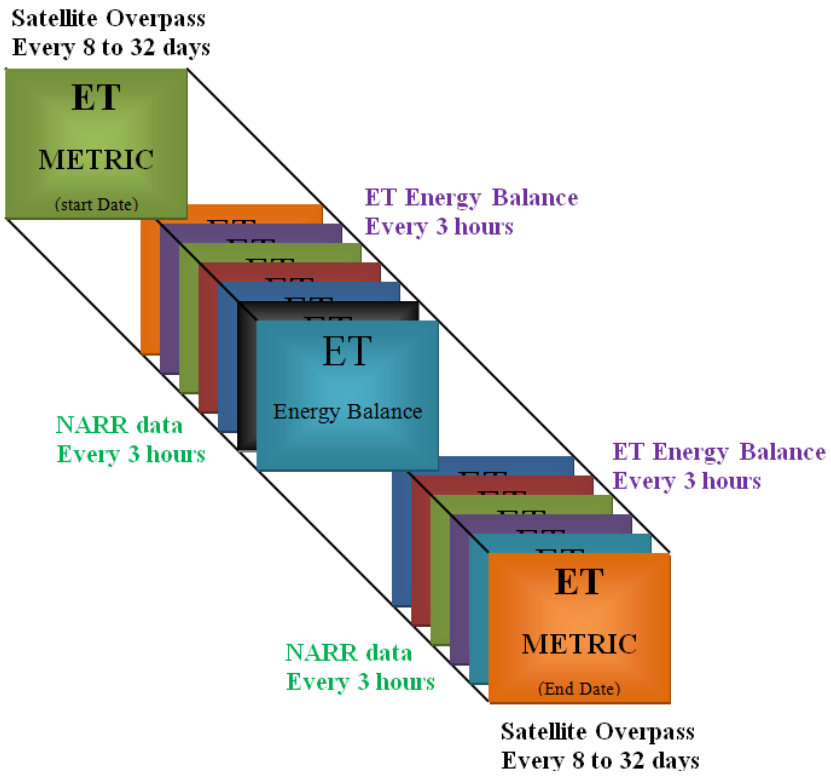

Fig. 2.3. An illustration of the partitioning of ET at satellite overpass dates and extrapolation of ET between satellite overpass dates

In this section, a detailed discussion is carried out on the soil water balance model adopted in this study. Soil water balance is a key element of the land surface model as it helps to track soil moisture at surface and root zone, which is necessary to estimate resistances to energy. These resistances are measure of ET in aerodynamic equations.

2.2 Soil Water Balance Sub-model

In general, three kinds of soil water balance methods are widely used in land surface, irrigation and hydrological modeling. The first method involves the physical mass balance of soil water content (Budyko, 1956 and Manabe, 1969), and it has been extensively used in

different forms for different numbers of soil layers (Milly, 1992, Schaake et al., 1996 and Allen et al., 1998). Depending on the complexity of the modeling approach, some important soil water movement processes, such as capillary rise, gravitational processes, and root uptake water, may be ignored. Another widely used soil water balance model is the two layer force restore model (Deardorff, 1977, Deardorff, 1978, Sellers, 1986, Noilhan and Mahfouf, 1996 and WEB-SVAT modeling). The diffusive flux of water between the surface and bulk root layer may be estimated by the function of soil moisture at the root zone (θ_{root}) and force restore coefficients. Finally, a multi-layered soil water balance method with a one dimensional Richards' equation may be used for the prediction of soil moisture (Lee and Abriola, 1999 and Irannejad and Shao, 1998). These water balance approaches to land surface modeling have been discussed in detail by Shao, 1998, Peng et al., 2002 and Barrgaoui, 2012.

This study implements is a simple physical water mass balance type soil water balance model. This is an advancement of the first modeling approach described in the previous section, in which soil evaporation (E_{ss}) and canopy transpiration (T) are computed separately, in contrast to a conventional single source model. This method incorporates soil moisture content through soil surface resistance in the soil surface layer and canopy resistances at the rooting depth layer. In this implemented soil water sub-model, the soil profile is divided into three layers (fig. 2.4). The 1^{st} (top) layer is the soil surface layer, where evaporation takes place, and it is 100 mm in depth from the surface. The 2^{nd} layer represents the rooting depth (d_{root}) where transpiration takes place and includes the 1^{st} (evaporation) layer as a subset. The 2^{nd} layer is extended from the surface to 1-2 m depth depending on the type of the vegetation. The rooting depth is set at 1 m for all vegetated areas, except for forest and sagebrush desert, for which it is set at 2 m. This is because the root zones of mature forests and certain other

kinds of vegetation like sage brush desert can go up to 2 m depth (Richards and Caldwell, 1987 and Robson and Kingery, 2006). The rooting depth of the cultivated agricultural vegetation is generally around 0.2 – 2.0 m (NRCS handbook). These d_{root} values can be refined according to the land use type and crop type to match observed soil moisture in the root zone. The 3rd layer is the deep percolation layer that is used to keep track of fluxes outside of the root zone. The implemented soil water balance focuses on the first two layers. The 1st layer is a subset of the 2nd layer. This allows for estimation of the evaporation from exposed soil and quantification of the impact of this evaporation on depletion of water available for transpiration in the root zone. Similar method are implemented by Schaake et al., 1996, FAO 56 (Allen et al., 1998), Hunsaker et al., 2003, and Er-Raki, 2008.

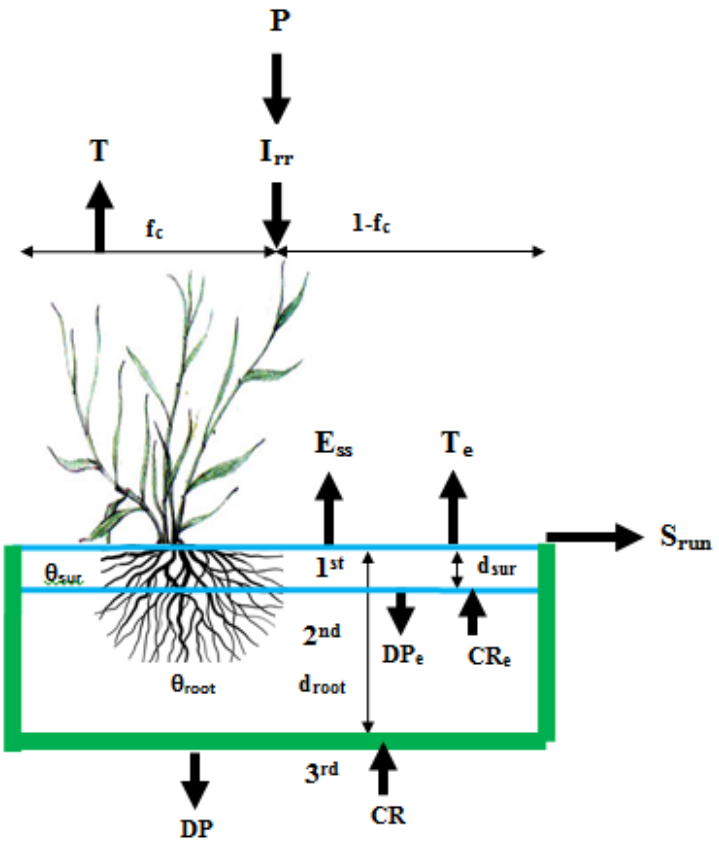

Fig. 2.4. A representative sketch of soil surface and root zone control volume for soil water balance

The blue block in fig. 2.4 shows the control volume of the soil surface layer, and the green block shows the control volume of the bulk root zone layer. In this model, no particular information regarding the soil moisture is measured by any other means. The actual distribution of water in the vertical profile with respect to time is not known. A soil water balance of the surface layer was conducted first to determine E_{ss}. Soil surface evaporation (E_{ss}) is subtracted from a soil water balance of root zone in later calculations to calculate final soil moisture at root zone. The soil water balance is updated every three hours to compute a new set of θ_{sur} and θ_{root}.

In the following section, the detailed description of soil water balance of the soil surface layer and root zone layer is carried out.

2.2.1 Soil Water Balance of Soil Surface Layer: Surface to d_{sur} (100 mm) layer

Soil moisture of the upper d_{sur} at the current time step is computed by using soil moisture from the previous time step ($\theta_{sur\ (i-1)}$) and balancing the soil water fluxes of the current time step takes into account precipitation ($P_{(i)}$), soil surface evaporation ($E_{ss(i)}$), surface runoff ($S_{run(i)}$), irrigation ($I_{rr(i)}$) and deep percolation ($DP_{e(i)}$). The depth involving E_{ss}, i.e. d_{sur}, is generally taken as 100 mm (Dickinson, 1984). Soil moisture at the satellite overpass time is taken as the starting point, and it is estimated by an inversion model (Dhungel and Allen, 2014a). The soil water balance of the upper soil portion is shown eqn. (7).

$$\theta_{sur(i)} = \theta_{sur(i-1)} + \frac{\left(P_{(i)} + I_{rr(i)} - S_{run(i)}\right) - E_{ss(i)} - T_{e(i)}}{d_{sur}} - DP_{e(i)} + CR_{e(i)} \quad (7)$$

where i is current time step, $\theta_{sur(i)}$ is volumetric water content (VWC) for the current time step (m^3/m^3), $\theta_{sur(i-1)}$ is the VWC of the surface layer for the previous time steps (m^3/m^3), $E_{ss(i)}$ is soil surface evaporation (mm), $P_{(i)}$ is precipitation (mm), $S_{run(i)}$ is surface runoff (mm), $I_{rr(i)}$ is irrigated water (mm), d_{sur} is soil surface depth (mm), $DP_{e(i)}$ is deep percolated water from the

upper soil layer to the root zone (m^3/m^3), $CR_{e(i)}$ is the capillary rise from the root zone into the 1st soil surface (m^3/m^3), and $T_{e(i)}$ is transpiration from the soil surface layer (mm). $CR_{e(i)}$ and $T_{e(i)}$ are neglected to simplify the soil water balance in this sub-model. The $\theta_{sur(i)}$ is in units of m^3/m^3 while the parameters $P_{(i)}$, $I_{rr(i)}$, $I_{rr(i)}$, $S_{run(i)}$, $E_{ss(i)}$ and $T_{e(i)}$ are in units of mm of water per unit area.

In soil water balance, the unit millimeters of water is initially converted to m^3 of water distributed over the depth (d_{sur} or d_{root}), and later converted to a m^3/m^3 equivalent by dividing the depth (eqn. 8 – 10). $E_{ss(i)}$ is computed iteratively in this process and is updated according to $\theta_{sur(i)}$ with each iteration. In the implemented soil moisture sub-model, the soil water balance of the surface layer at the current time step is written as the following conditional equation, assuming $CR_{e(i)}$ and $T_{e(i)}$ as zero (eqn. (8)).

$$\theta_{sur(i)} = \begin{cases} \theta_{sur(i-1)} + \dfrac{\left(P_{(i)} + I_{rr(i)} - S_{run(i)}\right) - E_{ss(i)}}{d_{sur}} & \text{if } \theta sur_i \le \theta_{fc} \\ \theta_{fc} & \text{if } \theta sur_i > \theta_{fc} \end{cases} \quad (8)$$

When $\theta_{sur(i)}$ is greater than field capacity (θ_{fc}), soil water from the surface layer is deep percolated to the 2nd root zone layer (d_{root}); therefore VWC of the upper surface layer is limited to θ_{fc}.

2.2.2 Soil Water Balance of Root Zone: Surface to d_{root} (1-2 m) layer

The soil water balance of the rooting depth (d_{root}) is computed from eqn. (9).

$$\theta_{root(i)} = \theta_{root(i-1)} + \frac{\left(P_{(i)} + I_{rr(i)} - S_{run(i)}\right) - T_{(i)} - E_{ss(i)}}{d_{root}} - DP_{(i)} + CR_{(i)} \quad (9)$$

where $\theta_{root(i)}$ is the VWC at the root zone for the current time step (m^3/m^3), $\theta_{root(i-1)}$ is the VWC of the root zone from the previous time steps (m^3/m^3), $T_{(i)}$ is transpiration from the root zone (mm), $DP_{(i)}$ is deep percolation below the root zone (m^3/m^3), and $CR_{(i)}$ is the capillary rise

from 3rd layer to the root zone (m^3/m^3). In this sub-model, the soil water balance of the root zone layer for the current time step is written using the following conditional equation, which assumes $CR_{(i)}$ and $DP_{(i)}$ to be zero.

$$\theta_{root(i)} = \begin{cases} \theta_{root(i-1)} + \dfrac{(P_{(i)} + I_{rr(i)} - S_{run(i)}) - T_{(i)} - E_{ss(i)}}{d_{root}} & \text{if } \theta_{root(i)} \leq \theta_{fc} \\ \theta_{fc} & \text{if } \theta_{root(i)} > \theta_{fc} \end{cases} \quad (10)$$

When the soil water content at root zone (θ_{root}) is greater than the field capacity (θ_{fc}), it will be deep percolated ($DP_{(i)}$) below to the bulk layer. T_i is computed iteratively and any change in $\theta_{root\ (i)}$ will update T_i with each iteration. Capillary rise ($CR_{(i)}$) from the 3rd layer into the bulk layer (2nd) is neglected.

So as to accurately estimate ET in irrigated agricultural land, it is important to account irrigation events between the satellite overpass dates. BATANS incorporates an irrigation sub-model to account irrigation events. The following section discusses the developed irrigation sub-model.

2.3 Irrigation Sub-model and Components

Irrigation (I_{rr}) is assumed to be applied to irrigated agricultural lands in a semiarid climate when soil moisture in the root zone is below the threshold moisture content (θ_t). The amount of depleted soil moisture at d_{root} is added as irrigation to recharge the soil moisture to the field capacity (θ_{fc}). Threshold moisture content (θ_t) is defined as the moisture content at which plants start getting stressed and no longer transpire at reference rates. At the time of irrigation, both surface and root zone moisture content is within the field capacity (θ_{fc}) using irrigation sub-model. As mentioned earlier, when the moisture content is greater than field capacity (θ_{fc}), water is released from the root zone as a deep percolation (DP). Equation (11) shows the conditional equation for an irrigation sub-model used in the developed model. The

total amount of the applied irrigation water depends on soil moisture below the θ_t and root depth (d_{root}).

$$I_{rr(i)} = \begin{cases} (\theta_{fc} - \theta_{root(i)}) \, d_{root} & \text{if } \theta_{root(i)} < \theta_t \\ 0 & \text{if } \theta_{root(i)} \geq \theta_t \end{cases} \quad (11)$$

Figure 2.5 shows a representative sketch of different soil moisture contents and available water for vegetation in the irrigation sub-model.

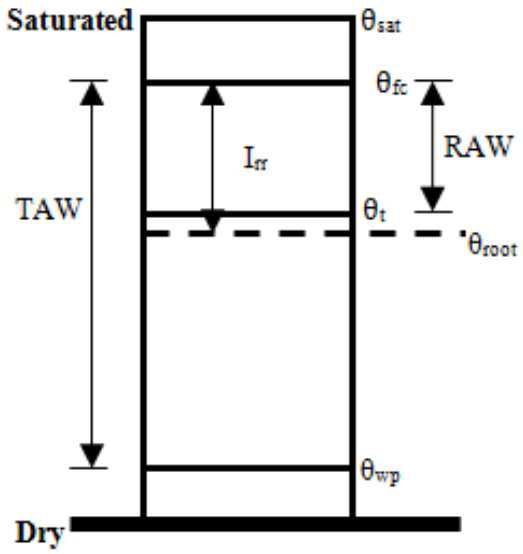

Fig. 2.5. A representative sketch of different soil moistures and parameters used in irrigation sub-model

Total available water (TAW) in fig. 2.5 is water available from soil moisture at field capacity (θ_{fc}) to wilting point (θ_{wp}). The threshold moisture content (θ_t) is computed using readily available water (RAW) and θ_{fc} (eqn. (12)).

$$\theta_t = \theta_{fc} - RAW \quad (12)$$

Readily available water (RAW) is computed from the manageable allowable depletion (MAD) and total available water (TAW) as according to eqn. (13).

$$RAW = MAD(\theta_{fc} - \theta_{wp}) \quad (13)$$

Manageable allowable depletion (MAD) is determined according to the derived relative ET_rF (Ref_ET_rF) at the time of irrigation. Ref_ET_rF is used to distribute the plant stress by MAD in between the satellite overpass dates. A regression equation (eqn. (14)) has been developed for MAD to account for different levels of plant stress for different kinds of vegetation and conditions (Allen, 2013). MAD is limited to a maximum value of 0.95.

$$\mathrm{MAD} = -2.914 - 6.608\,\mathrm{Rel\_ETrF} + 9.632\sqrt{\mathrm{Rel\_ET_rF}} + 0.858\,\mathrm{p} \tag{14}$$

where p is the fraction of depletion of available water before stress, which is generally taken as 0.5. Ref_ET_rF was computed from eqn. (15), and it is limited to a range from 0.55 to 1. MAD and Rel_ET_rF are used for irrigated agricultural lands, where actual irrigation is applied, and it is not used for other land use classes.

$$\mathrm{Rel\_ET_rF} = \frac{\mathrm{ETrF_{act(ave)}}}{\mathrm{ETrF_{pot(ave)}}} \tag{15}$$

where $ET_rF_{pot(ave)}$ is the average potential ET_rF for two satellite overpass dates, and $ET_rF_{pot(act)}$ is the actual ET_rF for two satellite overpass dates. $ET_rF_{pot(ave)}$ and $ET_rF_{act(ave)}$ are calculated from eqn. (16a) and (16b) respectively.

$$\mathrm{ETrF_{pot(ave)}} = 1.25\left(\frac{\mathrm{NDVI_{(S)}} + \mathrm{NDVI_{(E)}}}{2}\right) \tag{16a}$$

$$\mathrm{ETrF_{act(ave)}} = \frac{\mathrm{ETrF_{act_{(S)}}} + \mathrm{ETrF_{act_{(E)}}}}{2} \tag{16b}$$

where $ET_rF_{act(S)}$ is actual ET_rF of the current satellite overpass date, $ET_rF_{act(E)}$ is actual ET_rF of the next satellite overpass date, $NDVI_{(S)}$ is NDVI of the current overpass date, and $NDVI_{(E)}$ is the NDVI of the next satellite overpass date, from the METRIC model.

As mentioned earlier, resistances to energy fluxes are measure of ET estimations. In this section, a brief description of the formulation and computational procedure of soil surface

resistance (r_{ss}) and canopy resistance (r_{sc}) is discussed. A detailed discussion of these resistances is carried out in Dhungel and Allen, 2014a.

2.4 Soil Surface Resistance (r_{ss}) and Canopy Resistance (r_{sc}) Computation Procedure

To compute E_{ss} and T from the aerodynamic equation for the latent heat flux of the soil and canopy, r_{ss} and r_{sc} is needed. After calculating θ_{sur} from the soil water balance (eqn. (8)), r_{ss} is computed using an equation proposed by Sun (1982) (eqn. (17)). r_{ss} depends on the amount of soil moisture on the soil surface i.e. top layer.

$$r_{ss(i)} = 3.5\left(\frac{\theta_{sat}}{\theta_{sur(i)}}\right)^{2.3} + 33.5 \quad (17)$$

where θ_{sat} is soil moisture at saturation (m^3/m^3).

While computing r_{sc} using a Jarvis-type equation (eqn. (20)), different environmental weighting functions (F_1, F_2, F_3, F_4) were used to because the effect of plant stresses is needed. Some of the commonly used weighing functions for plant stress are soil moisture, solar radiation, temperature and humidity. In this study, weighting functions representing the environmental effects of plant stress due to photosynthetically active radiation (F_1) and soil moisture (F_4) are solely considered. As discussed in Dhungel and Allen, 2014a, environmental factors like temperature and humidity are not considered in this study, because temperature and humidity are considered to be relatively consistent between two satellite image dates. The formulation of F_1 is discussed in Dhungel and Allen, 2014a. While computing F_4 (eqn. (19)), logistic growth curve of available water fraction (AWF) developed in Dhungel and Allen, 2014a is used to compute F_4 (eqn. (18)). Soil moisture at field capacity (θ_{fc}) and soil moisture at wilting point (θ_{wp}) depend on the soil types. The typical values of θ_{fc} and θ_{wp} for silt loam soil are 0.36 m^3/m^3 and 0.12 m^3/m^3 (Kumar et al., 2010, Allen, 1998) respectively, and they are used in the development of this model. This is due to match the study area's soil type (silt

loam).

$$AWF_{(i)} = \frac{\theta_{root(i)} - \theta_{wp}}{\theta_{fc} - \theta_{wp}} \tag{18}$$

$$F_{4(i)} = \left[\frac{1}{1 + 20\, e^{(-8\, AWF_{(i)})}}\right] \tag{19}$$

The weighting coefficients F_1 and F_4 are limited to 1. Weighting coefficients near or equal to 1 show that there is no stress in vegetation associated with the environmental factor. When these weighing coefficients are small, r_{sc} becomes large, evidencing a very high stress level in the vegetation.

$$r_{sc(i)} = \frac{r_l}{\frac{LAI_{(i)}}{f_{c(i)}} F_{1(i)}\, F_{4(i)}} \tag{20}$$

where r_l is single area leaf equivalent bulk stomatal resistance (s/m).

3.0 Application

3.1 Data Requirements and Study Area

The model was coded in a Python scripting with ArcGIS modules and functions. The model runs every three hours for an entire month with a full surface energy balance (fig. 2.2). So, it is important to have an efficient platform to run the model since it is computing resource intensive. Python and GIS handle time series calculations efficiently compared to other image processing software like ERDAS Imagine. When the model is implemented for larger areas, the model should run faster with the use of servers or computing clouds.

Data acquired from the METRIC model has a 30 m resolution while NARR reanalysis weather data has 32 km resolution. Even though weather data acquired from the NARR reanalysis has coarser resolution (32 km), it is assumed that these weather data have a low variability within each 32 km pixel size. NARR reanalysis is a valuable source of climate data

with high temporal resolution; data is collected every 3 hours. Data acquired from the NARR reanalysis are air temperature (T_a) at 30 m, wind speed at 30 m (u_z), specific humidity (q_a) at 30 m, surface runoff (S_{run}), precipitation (P), incoming shortwave at surface ($R_{s\downarrow}$), and incoming long wave radiation at the surface ($R_{L\downarrow}$). Since 30 m is assumed to be the blending height over all half million 30 m pixels contained in the 32 km cell, $T_{a,}$ u_z and q_a taken at 30 m. Data acquired from the METRIC model were surface albedo (α), roughness length of momentum transfer (z_{om}), broadband emissivity (ε_o), leaf area index (LAI), and reference ET fraction (ET_rF) for two satellite overpass dates. Albedo (α), z_{om}, ε_o and LAI were linearly interpolated between the satellite overpass dates. It is because these parameters vary little between the satellite overpass, and it's difficult to acquire higher temporal and spatial resolution.

The extrapolation model was run from 05/17/2008 to 06/18/2008 for the test case. The model was ran for all of the 3 hours' time steps between the satellite overpass dates with a simulation period of about a month for an area near American Falls in southern Idaho. Figure 2.6 shows the P, S_{run}, $R_{s\downarrow}$, $R_{L\downarrow}$, $u_{z,}$ and T_a from NARR reanalysis for every three hours for the entire month. The maximum precipitation (P) is about 2.5 mm/3 hr. Air temperature (T_a) is below 300 K for the entire simulation period. The maximum wind speed is about 14 m/s and the average is 5.2 m/s.

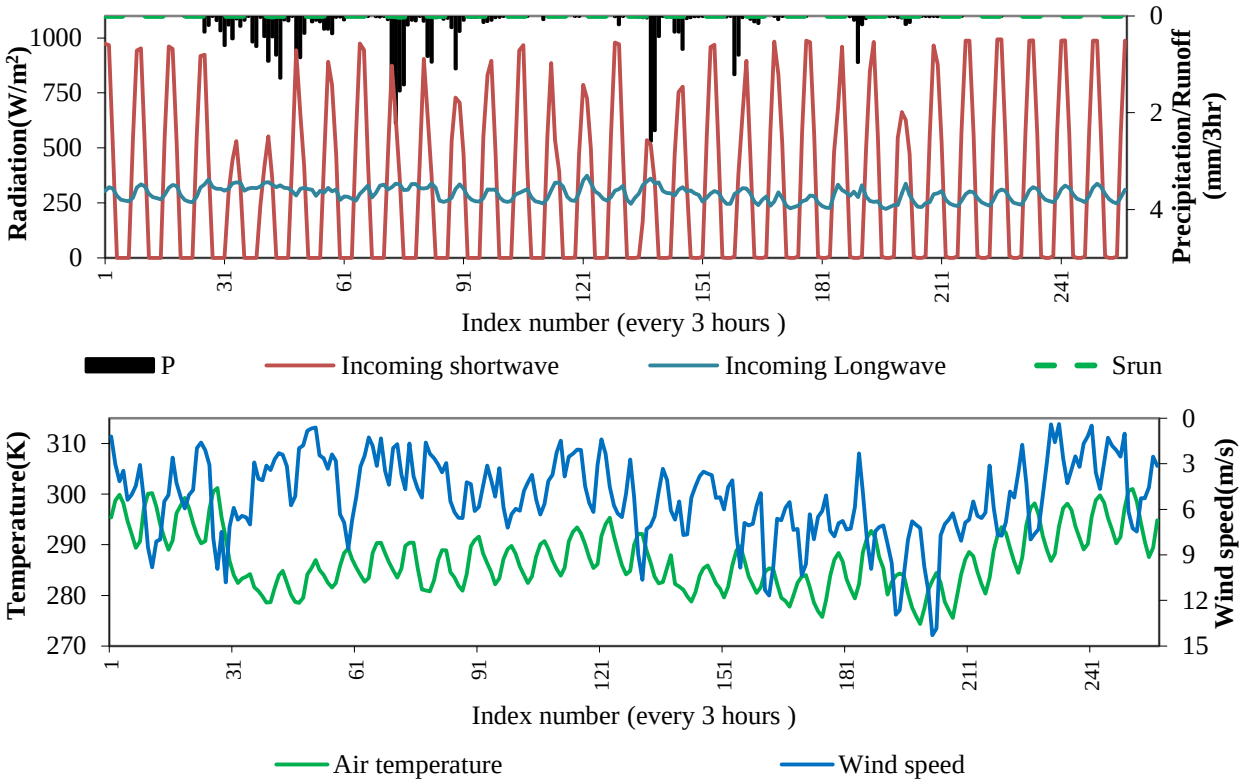

Fig. 2.6. NARR reanalysis data in three hour time intervals during the simulation period from 05/17/2008 to 06/18/2008

Figure 2.7 shows the study area location as a 500 km^2 area of interest that is contained within one NARR reanalysis pixel (blue box). It also shows the Landsat path 39 image for May 17, 2008. The smaller area of interest with different land use classes is chosen for computational efficiency and convergence purposes. Use of a single pixel of NARR reanalysis data can create biases in calculation, but the data has been carefully scrutinized and compared with ground data. No bias has been found between the ground meteorological data and the NARR reanalysis. NARR reanalysis data was compared to the Aberdeen AgriMet weather station (lat. =42.95 N, long. =112.83 W and elevation = 1341.46 m) data, and the two sets are correlated well.

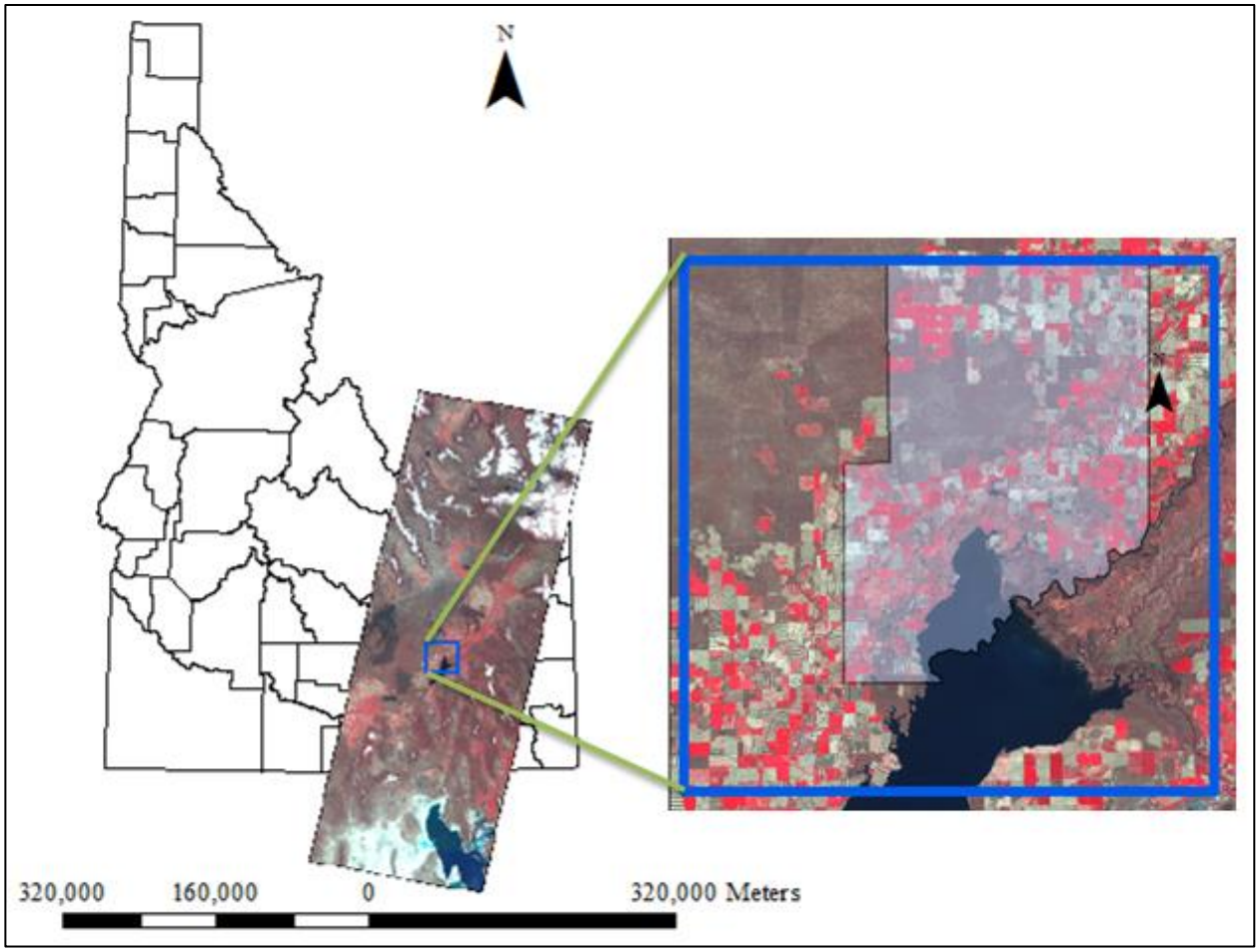

Fig. 2.7. Study area near American Falls, ID overlaying NARR reanalysis pixel and a Landsat path 39 image for May, 17, 2008

The soil in the study area is comprised of silt loam and loam. The Soil Survey Geographic (SSURGO) database has been used to acquire soil moisture data, including soil moisture at wilting point (θ_{wp}), field capacity (θ_{fc}) and saturation (θ_{sat}) for different types of soil. To identify land use classes, National Land Cover Database *(*NLCD, 2006) land use classes are used. Not much land use expansion and agricultural development happened in this region from 2006 to 2008 so it was still a valid land use classification to use for that time period on such a small region. Parameters like rooting depth (d_{root}), minimum solar radiation necessary for photosynthesis to occur (R_{gl}), roughness length of momentum (z_{om}), height of vegetation (h_c), irrigation, and minimum value single area leaf equivalent bulk stomatal

resistance (r_{lmin}) differ by land use class. Table 2.2 shows values of data acquired from NARR reanalysis on 05/17/2008 at 11 am (start of simulation), on 05/17/2008 at 2 pm (three hours after the first satellite overpass) and on 06/18/2008 at 11 am (end of the simulation).

Table 2.2. Data from NARR reanalysis for the study area

Variables	**05/17/2008 11 am**	**05/17/2008 2 pm**	**06/18/2008 11 am**
Wind speed at 30 m (u_z)	1.2 m/s	3 m/s	3.1 m/s
Air Temperature at 30 m (T_a)	295.4 K	299 K	294.8 K
Specific humidity at 30 m (q_a)	0.0041 kg/kg	0.004 kg/kg	0.0052 kg/kg
Incoming shortwave radiation ($R_{s\downarrow}$)	974 W/m^2	967 W/m^2	988 W/m^2
Incoming longwave radiation ($R_{L\downarrow}$)	303 W/m^2	320 W/m^2	310 W/m^2
Surface runoff (S_{run})	0 mm/3hr	0 mm/3hr	0 mm/3hr
Precipitation (P)	0 mm/3hr	0 mm/3hr	0 mm/3hr

4.0 Results and Discussions

Three different sub-areas of interest (sub-AOIs) are chosen inside the main AOI to evaluate model performance using different statistical measurements at the end of a satellite overpass date. They are upper right agricultural land (URA AOI), middle desert (MD AOI) and bottom left agricultural land (BLA AOI) (fig. 2.8a).

4.1 Satellite Overpass Time

Figure 2.8 shows the METRIC ET and NDVI at the satellite overpass date on 05/17/2008 approximately at 11 am and simulated ET for the next three hours (05/17/2008 at 2 pm). The maximum ET from METRIC at the satellite overpass on 05/17/2008 is about 0.94 mm/hr. It is intended to examine how well the model is able to simulate ET after three hours with similar meteorological conditions. This analysis is important for the validation of the extrapolation and inversion models. Partitioning of the surface energy balance fluxes on the satellite overpass date is done by the inversion model (Dhungel and Allen, 2014a), while extrapolation of ET for every three hours is done by the extrapolation model as discussed in

this paper. Three hours after the satellite overpass time, T_a is increased by 4 K and the rest of the parameters are similar to the satellite overpass time (Table 2.2). Visually, the simulation results of ET from the extrapolation model show a very similar trend three hours after the satellite overpass time when compared to the inversion model.

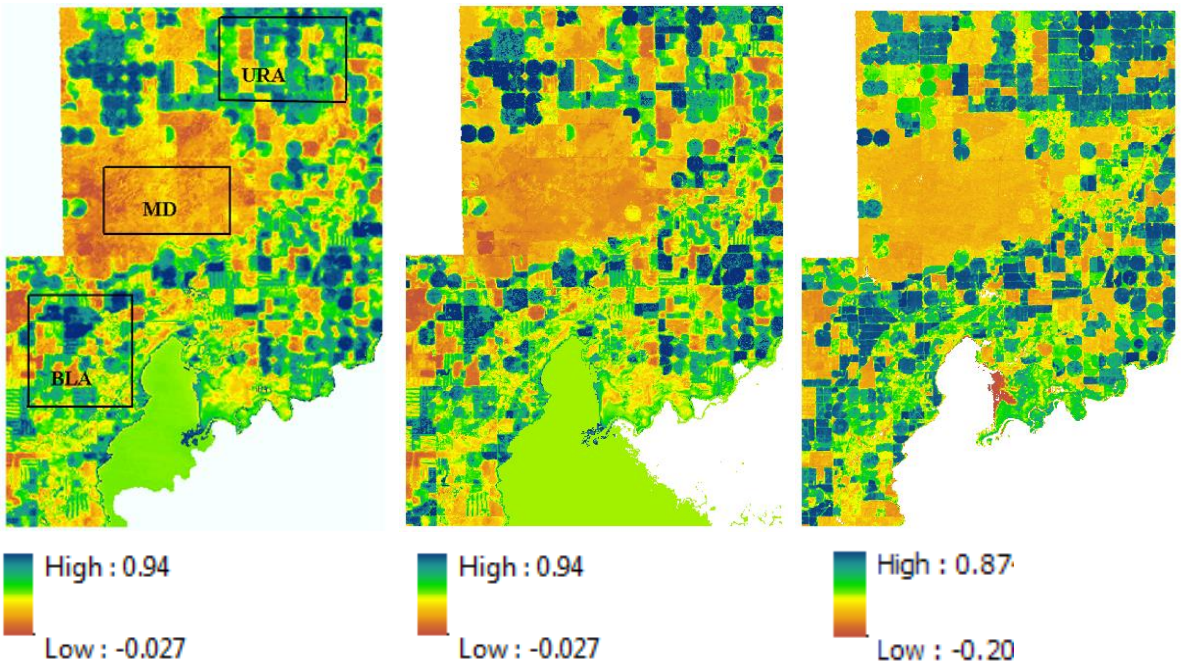

a) METRIC ET (mm/hr) (05/17/2008, 11 am) **b) Simulated ET (mm/hr) (05/17/2008, 2 pm)** **c) NDVI (05/17/2008, 11 am)**

Fig. 2.8. Visual comparison of METRIC ET at satellite overpass time to simulated ET three hours after satellite overpass and NDVI at satellite overpass on 05/17/2008 in southern Idaho, near American Falls

Figure 2.9 shows the simulated ET, METRIC ET and the NDVI at the end of the simulation period i.e. 06/18/2008, which was 32 days after the starting date. From a visual inspection, it can be ascertained that the model was able to simulate a pattern of ET similar to METRIC ET. Statistics confirmed that the simulated ET mimicked METRIC results in irrigated agricultural lands having high NDVI. Desert and grassland regions also showed similar results between the developed model and METRIC outputs. Most of the larger

discrepancies occurred in the irrigated agricultural pixels where NDVI is low. In agricultural lands where NDVI is low, ET is generally dominated by E_{ss}. Soil surface evaporation (E_{ss}) increases when irrigation or precipitation occurs and decreases rapidly when the soil drying. To have high ET in irrigated agricultural lands where NDVI is low, there must be a recent precipitation or irrigation event. There was no precipitation during the week prior to the satellite overpass date, so the higher values of ET in low NDVI areas probably resulted from an actual irrigation event in the field. In this case, the irrigation sub-model is not able to capture this actual event in the field probably because θ_{root} is still above threshold moisture content (θ_t). This process can easily create a mismatch between METRIC and simulated ET at the next satellite overpasses date. Even though the difference in ET at satellite overpass can be large due to this mismatch, the actual discrepancy may be smaller if the model just missed the irrigation time before satellite overpass date. Further discussion related to irrigation assumptions is presented in Section 4.2.

In addition to the irrigation scheduling time, numerous other factors may create mismatches between the simulated ET and METRIC ET. These include incorrect initial moisture content and inaccurate parameters such as d_{root}, r_{ss}, and $r_{sc,}$ etc. Some of the aspects of these variables and conditions are discussed in the later sections. While calculating H and LE, different sets of resistances are acting in combination within the aerodynamic equation. Formulations of these resistances directly affect the final value of simulated ET, and resistances may need to be adjusted so that the simulated ET matches METRIC ET at next satellite overpass date. This is because resistances and related fluxes are highly interdependent.

For the land use classes 52 and 72 (sagebrush desert and grassland), BATANS is able

to simulate ET similar to METRIC (fig. 2.9). Even if there is no precipitation in the week prior to the second satellite overpass date, both models are able to capture ET for the second overpass date, residual ET is possibly due to transpiration supplied by the stored soil moisture in the root zone. The simulation was conducted for the period from May to June, 2008; the root zone soil layer was still wet because of winter snow in this period. ET simulated from the extrapolation model and METRIC is fairly constant in desert and grassland for these satellite overpass dates (Fig 2.9).

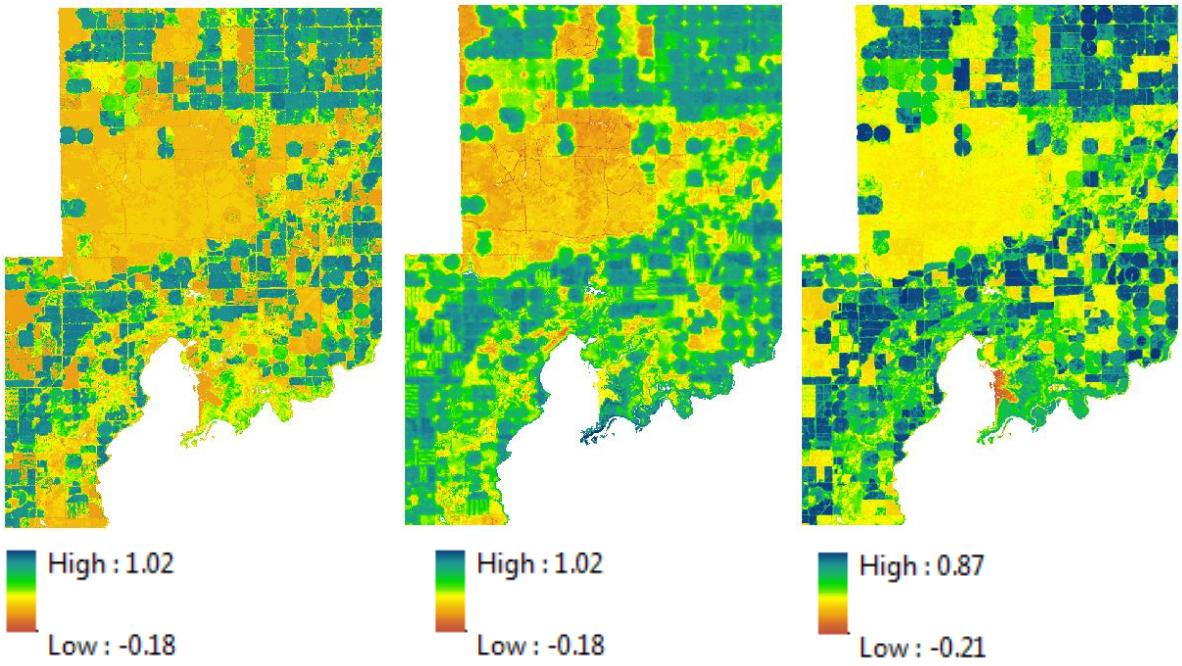

Fig. 2.9. Comparison of simulated ET to METRIC ET and NDVI at following satellite overpass date i.e. 06/18/2008 in southern Idaho, near American Falls

Figure 2.10 shows a comparison between the simulated ET, METRIC ET and NDVI for a small area inside the URA AOI. The suspected mismatch in irrigation time between the simulated and actual events, METRIC produced high ET in a right portion of central pivot C-1 area, where the simulation model was not able to capture the effects of that wetting event. As NDVI is low in C-1 area (0.10 - 0.31), soil water evaporated relatively quickly after

irrigation. For instance, in one of the irrigated agricultural pixel A2 (defined later) that lies in C-1 area where METRIC estimated high ET, irrigation sub-model applied irrigation once at 05/19/2008 for the entire simulation period. This observation clearly shows that one of the primary reasons for the mismatch in ET in low NDVI areas may be due to a discrepancy in irrigation timing.

Since the rooting depth is considered a constant 1 m for the irrigated agricultural land, the model may have over-predicted soil moisture in the root zone within low NDVI areas, which reduced the frequency of irrigation. But in reality, rooting depths may vary with the stage of plant growth and types of the vegetation. Frequent irrigation is required at the initial stage of vegetation growth, compared to the fully grown vegetation, because d_{root} is smaller compared to mature vegetation. So to increase accuracy of the simulated ET, where the NDVI is low, it is important to have an appropriate rooting depth according to the vegetation type and growth stage. Table 2.3 shows the statistical values of the fluxes from both the METRIC and the extrapolation model at the next satellite overpass date, which is 32 days after the start of the first satellite overpass date. Table 2.3 incorporates both the extrapolation model (column 1-12) and inversion model (13-14) results.

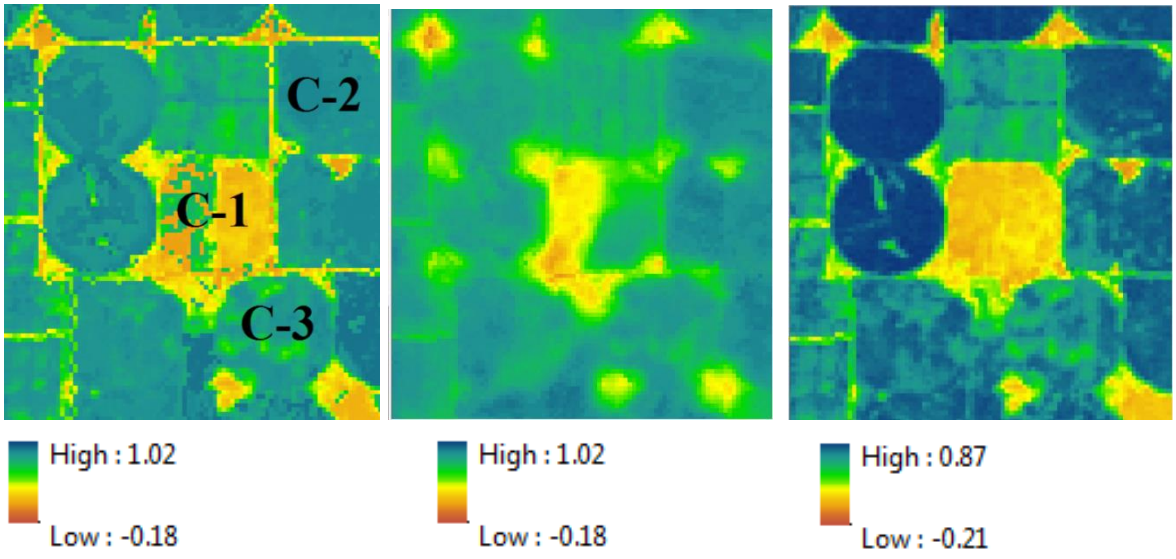

Simulated ET (mm/hr) **METRIC ET (mm/hr)** **NDVI**

Fig. 2.10. Comparisons between simulated ET to METRIC ET and NDVI inside upper right agricultural (URA) AOI at next satellite overpass date i.e. 06/18/2008 in southern Idaho, near American Falls

The following section discusses the results of BATANS in between the satellite overpass every three hours.

4.1.1 Extrapolation Model

The simulated mean ET from the extrapolation model and METRIC model matches very closely with a maximum difference of 0.1 mm/hr in all AOIs with an R^2 of about 057 - 0.68 (Table 2.3). It shows that the model is able to predict a similar mean ET after a month of simulation with a reasonable accuracy. Even though the simulated mean ET was consistent to METRIC estimations, individual variations were seen due to parameter uncertainty and irrigation mismatch. Simulated bulk surface temperature (T_b) in URA and BLA AOIs matches closely to the METRIC model, with a difference of 1 K. Mid desert (MD) AOI has a lower T_b than METRIC, which may be because of the steep temperature profile in the desert compared to irrigated agricultural areas. As discussed in Dhungel and Allen, 2014a, BATANS has difficulty simulating the higher temperature in the desert using aerodynamic type equation in

surface energy balance. Simulated mean G is slightly lower than METRIC G which is possibly because of the assumption that there is no G in the vegetation portion. The maximum difference between the mean G values is about 27 W/m^2, which occurred in URA AOI. The largest difference occurs in mean H occurred in BLA AOI, and it was about 80 W/m^2. The maximum difference in mean R_n was about 44 W/m^2, and it occurred in MD AOI.

Some other statistical parameters that were used to evaluate the degree of agreement between the simulated and METRIC models includes the mean absolute error (MAE), root mean square error (RMSE), coefficient of efficiency (E), and the index of agreement (d_i). The coefficient of determination (R^2) of the fluxes varied over a wide range for different fluxes and parameters (Table 2.3). The index of agreement (d_i) varies from 0 to 1, like R^2, and higher values show better agreement between the simulated and METRIC data. In most cases, R^2 and index of agreement (d_i) have similar values, which verify the statistical accuracy of these parameters. Coefficient of efficiency (E) has a negative sign in some surface energy balance flux parameters, showing that the observed mean is a better predictor than the simulated model (Wilcox et al., 1990). Higher values of E between the simulated and METRIC results indicate better agreement, and E can vary from minus infinity to 1. MAE and RMSE are larger in H, with a maximum value of 108 W/m^2, showing greater variance in the individual errors in the simulated H. Even if some of the simulated surface energy fluxes vary from the METRIC estimations, final ET values have less variation, as the bias of the surface energy fluxes are possibly neutralized. Thermal based surface temperature is one of the dominating factors when computing ET from surface energy balance models. Simulated surface energy fluxes from BATANS are based on the iteratively computed surface temperature, a method

that has more uncertainty when calculating fluxes than the METRIC model. So, some variations between the simulated and METRIC estimations are anticipated.

Figure 2.11a shows a hourly scatter plot of simulated ET and METRIC ET of about 30,000 sample pixels at the end of the simulation period (at 06/18/2008) for BLA AOI. The coefficient of determination (R^2) is about 0.67 and the RMSE is about 0.17 mm/hr (fig. 2.11a). The hourly scatter plot can have more variability than daily ET, so it is equally important to compare the daily scatter plot of ET. The daily ET scatter plot is also computed by letting the extrapolation model run beyond the satellite overpass time for a full day, without interruption at the satellite overpass time. The scatter plot shows that daily ET and hourly ET have similar trends (fig. 2.11a and 2.11b). The R^2 of the daily ET is about 0.65 (fig. 2.11b).

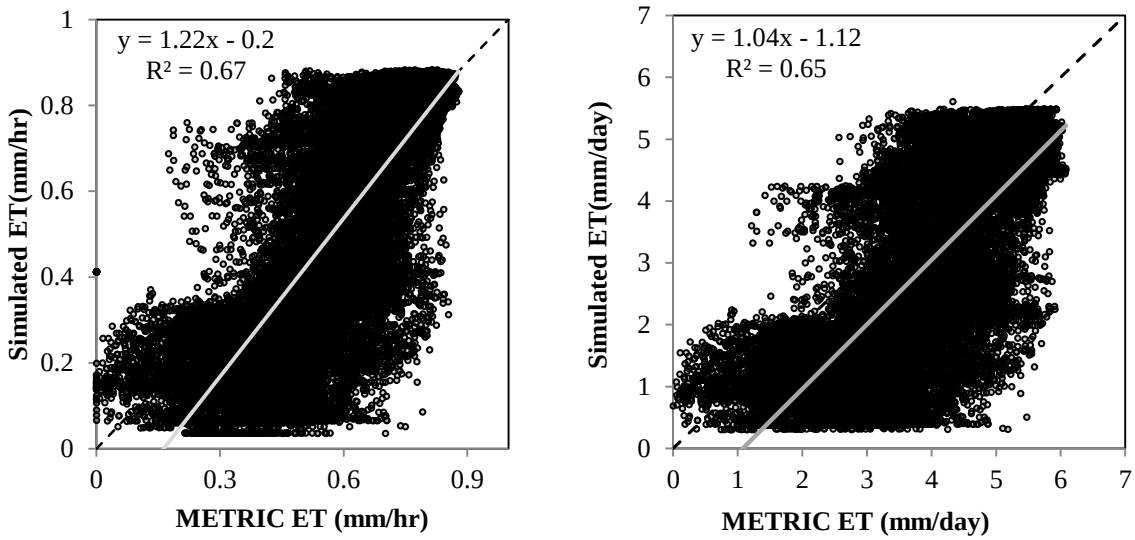

a) Hourly ET (mm/hr) **b) Daily ET (mm/day)**

Fig. 2.11. Scatter plot between simulated and METRIC ET at next satellite overpass date for bottom left agricultural (BLA) AOI on 06/18/2008 in southern Idaho, near American Falls

Figure 2.12 shows the hourly scatter plots between METRIC ET vs. NDVI and simulated ET vs. NDVI for BLA AOI. In the simulated ET vs. NDVI plot, the data tends to approach the 1:1 line because of a possible mismatch in irrigation events, and some influence of NDVI on the simulated ET, since ET is weighted based on NDVI.

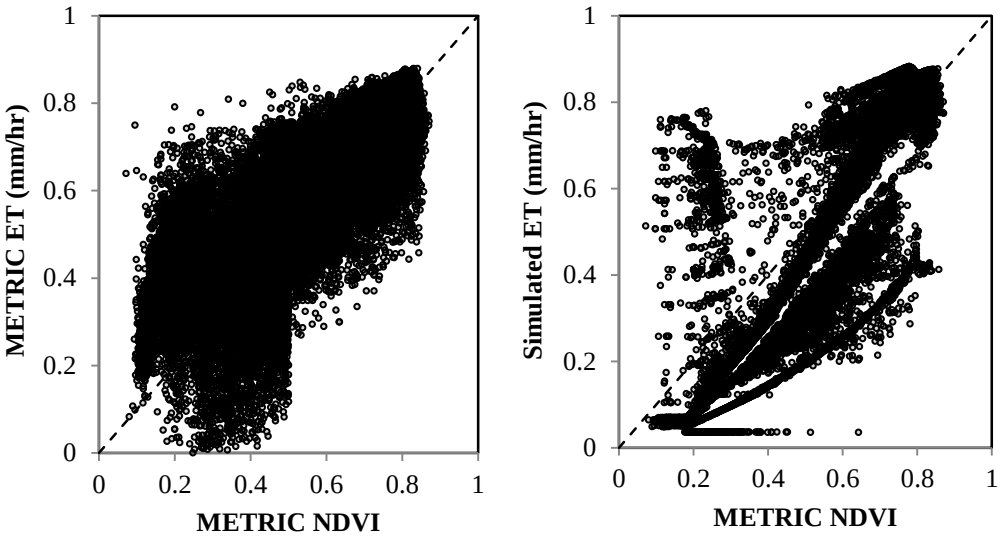

a) METRIC ET vs. NDVI (mm/hr) **b) Simulated ET vs. NDVI (mm/day)**

Fig. 2.12. Scatter plot of METRIC ET vs. METRIC NDVI and simulated ET vs. METRIC NDVI for bottom left agricultural (BLA) AOI on 06/18/2008 in southern Idaho, near American Falls

Figure 2.13 shows the comparison between the daily ET from BATANS and reference ET (ET_r) from the Aberdeen weather station for different selected pixels during the simulation period. Pixel A1 is an agricultural pixel with high NDVI (0.71 to 0.83), A2 is agricultural pixel with low NDVI (0.12 to 0.32), and D1 is a desert pixel with an NDVI of about 0.2. Pixel A1 closely followed ET_r, as it is near fully covered with vegetation. Pixels A2 and D1 have lower daily ET compared to A1, because f_c is small in these pixels and precipitation was low in this period. These results confirmed that BATANS is able to simulate a realistic trend of ET throughout a simulation period between two images. A detailed discussion of these

individual pixels is carried out in the section 4.2. The average daily ET are about 4.6 mm/day, 2.2 mm/day and 1.47 mm/day for A1, A2 and D1 pixels respectively.

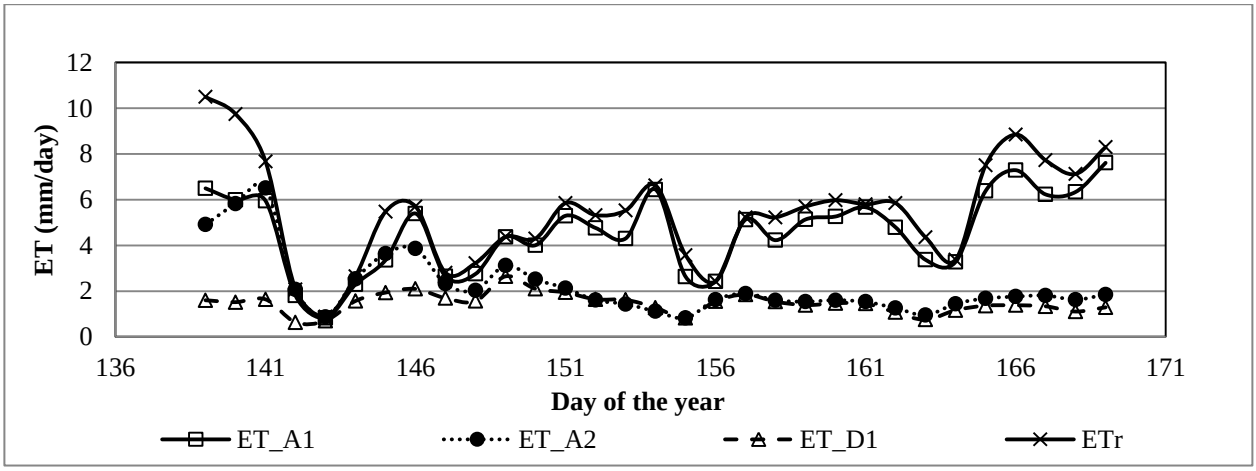

Fig. 2.13. Simulation results of daily ET for agricultural pixels A1 (ET_A1), A2 (ET_A2) and desert pixel D1 (ET_D1) compared to reference ET (ET_r) from Aberdeen AgriMet station between satellite overpass dates

4.1.2 Inversion Model

While inverting METRIC ET using the inversion model, the simulated model cannot replicate H, G, T_s and R_n exactly like the METRIC results. So, the surface energy balance fluxes can have different results, depending upon the degree of error when calculating surface temperature and other fluxes. It is important to understand that the METRIC and developed inversion model use different methods to calculate final ET, though both use surface energy balance approaches. So, the results of these two models are expected to vary to some extent because of different approaches. As mentioned earlier, the inversion model only uses METRIC ET and surface roughness parameters, and the rest of the surface energy fluxes are computed iteratively using NARR reanalysis data. Another interesting observation is the inversion model at 06/18/2008 (col. 13-14) has results similar to the interpolation model results (col. 2-3) at the end of the simulation period. The mean G from the inversion model is less than 10 W/m^2 different from the interpolation model. Mean H from the inversion model

matches very closely to interpolated H; it is within a 20 W/m^2 difference. Difference in R_n is also within 20 W/m^2. The results indicate that both simulated and inversion model fluxes match very well with all parameters. The major objective of this study is to extrapolate ET between the satellite overpass, the major focus is to simulate realistic ET using BATANS which was ultimately obtained. This allows for the consideration of using BATANS to extrapolate ET every 3 hours in between satellite images with the utilization of NARR data. However, other surface energy fluxes can have biases and can vary according to the iteratively calculated surface temperature. It is highly beneficial to simulate relatively accurate ET every three hours based on weather data from NARR reanalysis to estimate ET between images, even though surface energy fluxes can have some variation.

Table 2.3. Statistics of combined surface energy balance fluxes from extrapolation and inversion model compared with METRIC estimations

Fluxes	METRIC Results (06/18/2008 11am.)		Simulated Results (Extrapolation model) (06/18/2008 11am.)									Simulated Results (Inversion model) (06/18/2008 11 am.)	
1	2	3	4	5	6	7	8	9	10	11	12	13	14
Statistical measures	Mean	Standard deviation	Mean	Standard Deviation	R^2	Slope	Intercept	MAE	RMSE	E	d_i	Mean	Standard Deviation
ET	(mm/hr)	mm/hr)	(mm/hr)	(mm/hr)	%		(mm/hr)	(mm/hr)	(mm/hr)		(mm/hr)	(mm/hr)	(mm/hr)
URA AOI	0.62	0.20	0.60	0.27	0.64	1.09	-0.08	0.11	0.17	0.29	0.71	0.62	0.2
BLA AOI	0.59	0.19	0.52	0.28	0.68	1.2	-0.18	0.13	0.17	0.17	0.68	0.58	0.19
MD AOI	0.16	0.04	0.18	0.04	0.57	0.56	0.08	0.02	0.03	0.49	0.64	0.16	0.05
Temperature (T_b)	K	K	K	K	%		K	K	K		K	K	K
URA AOI	303.1	6.5	304.2	4.1	0.55	0.46	163.18	3.8	4.5	0.51	0.67	303.5	3.2
BLA AOI	304.0	5.8	304.9	3.9	0.51	0.48	157.5	3.4	4.19	0.48	0.60	304	2.6
MD AOI	322.1	0.87	309.1	0.47	0.0	-0.03	319.6	12.9	12.9	-217.1	0.05	309.1	0.73
Ground heat flux (G)	W/m^2	W/m^2	W/m^2	W/m^2	%		W/m^2	W/m^2	W/m^2		W/m^2	W/m^2	W/m^2
URA AOI	57.3	24.51	40.0	45.6	0.86	1.73	-59.2	27.3	30.2	-0.52	0.58	31.0	36.05
BLA AOI	70.4	44.0	50.0	48.4	0.38	0.68	1.9	34.07	45.3	-0.06	0.54	36.1	35.2
MD AOI	115.2	11.2	99.4	4.7	0.31	0.23	72.3	15.8	18.4	-1.6	0.37	88.2	8.3
Sensible heat flux (H)	W/m^2	W/m^2	W/m^2	W/m^2	%		W/m^2	W/m^2	W/m^2		W/m^2	W/m^2	W/m^2
URA AOI	109.4	73.9	172.0	96.93	0.50	0.93	69.7	70.1	92.5	-0.56	0.49	168.7	71.5
BLA AOI	125.6	71.3	205.1	106.6	0.54	0.4	36.3	90.2	108.7	-1.3	0.49	191.1	78.1
MD AOI	288.0	28.1	333.5	20.5	0.56	0.54	175.1	48.2	49.0	-2.0	0.28	355.9	13.6
Net radiation (R_n)	W/m^2	W/m^2	W/m^2	W/m^2	%		W/m^2	W/m^2	W/m^2		W/m^2	W/m^2	W/m^2
URA AOI	590.51	49.7	613.7	50.7	0.54	0.75	168.79	34.64	43.07	0.25	0.61	624.1	40.6
BLA AOI	592.0	45.6	608.14	50.6	0.49	0.78	144.6	32.03	40.5	0.21	0.61	622.8	63.17
MD AOI	508.7	13.6	552.38	7.75	0.0	0.03	534.9	43.8	46.2	-10.55	0.19	562.3	9.6

URA-Upper right agricultural, BLA-Bottom left agricultural land, MD- Middle Desert

4.2 Three Hourly Results (Extrapolation Model)

4.2.1 Irrigated Agricultural Pixel A1 (Coordinate: 2600407, 1328596)

In this section, the behavior of individual pixels is discussed for the entire simulation period. Figure 2.14 shows the comparison between the simulated ET, soil surface evaporation (E_{ss}), and transpiration (T) for an irrigated agricultural pixel A1 that is inside one of the central pivots. In this pixel, NDVI varies from 0.71 to 0.83 at the start and end of the simulation period respectively. ET from the METRIC model, at the start and end of the satellite overpass, are 0.67 mm/hr and 0.7 mm/hr respectively. ET from the simulated model is about 0.79 mm/hr at the end of the simulation period. Reference ET (ET_r) from the Aberdeen AgriMet weather station is used as an upper boundary condition to limit E_{ss} and T, which is about 0.9 mm/hr at 06/18/2008. There is very low precipitation during this simulation period, less than 3 mm. Figure 2.14 shows that the simulated E_{ss} is very small compared to T as the pixel is near fully covered with vegetation. Therefore, a majority of ET is the contribution of T, and small precipitation events are not able to elevate E_{ss} when f_c is near to 1. ET varied according to the weather conditions and the influence of NDVI is not dominant because NDVI is relatively high throughout the simulation period. Figure 2.14 also includes the linearly interpolated NDVI. The results confirmed that the BATANS model was able to simulate realistic ET every three hours and at the end of the simulation period.

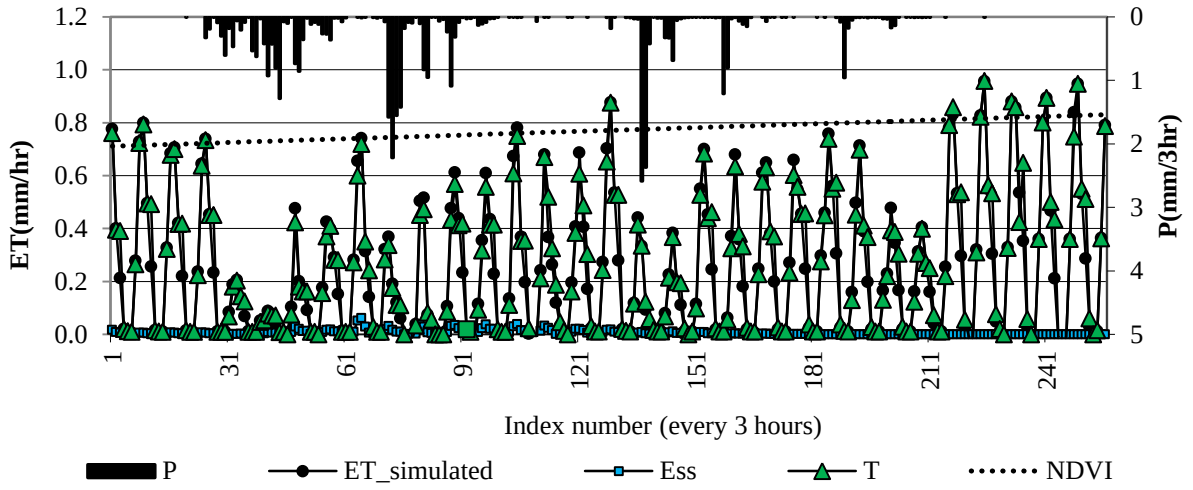

Fig. 2.14. Simulation results of combined ET (ET_simulated), soil evaporation (E_{ss}) , canopy transpiration (T), and precipitation (P) for an irrigated agricultural pixel A1 (Land use 82, NDVI: 0.71 to 0.83 and f_c: 0.86 to 1) from 05/17/2008 to 06/18/2008

Figure 2.15 shows the comparison between simulated bulk surface temperature (T_b) and air temperature (T_s) at 30 m. The differences between T_b and T_s are small in most of the time steps because the pixel is fully vegetated irrigated agricultural land, creating nearly neutral conditions. The discussion above also confirmed that the simulated surface temperature and thermal temperature are statistically consistent. The maximum simulated surface temperature is about 305 K. This analysis confirmed that BATANS is able to simulate realistic surface temperature at fully vegetated agricultural pixel.

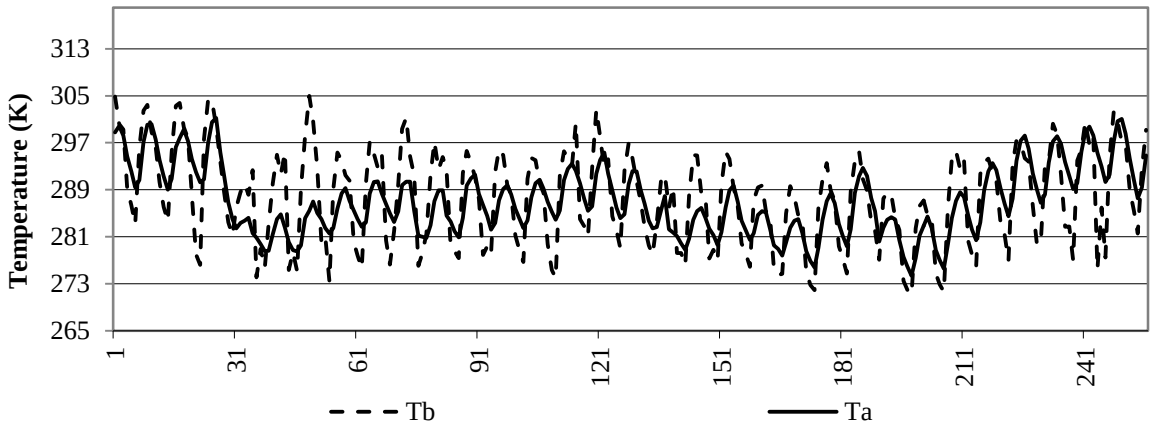

Fig. 2.15. Simulation results of bulk surface temperature (T_b) and air temperature (T_a) from NARR reanalysis for an irrigated agricultural pixel A1 (Land use 82, NDVI: 0.71 to 0.83 and $f_{c:}$ 0.86 to 1) from 05/17/2008 to 06/18/2008

Figure 2.16 shows the cumulative values of ET_r, simulated ET, precipitation and irrigation. Cumulative ET_r is about 35 mm higher than cumulative ET. The total ET for the simulation period was about 185 mm. A total applied irrigation and precipitation match closely to the cumulative ET, which is about 204 mm. Irrigation was applied once at 05/25/2008 within the simulation period. Cumulative P is about 35 mm.

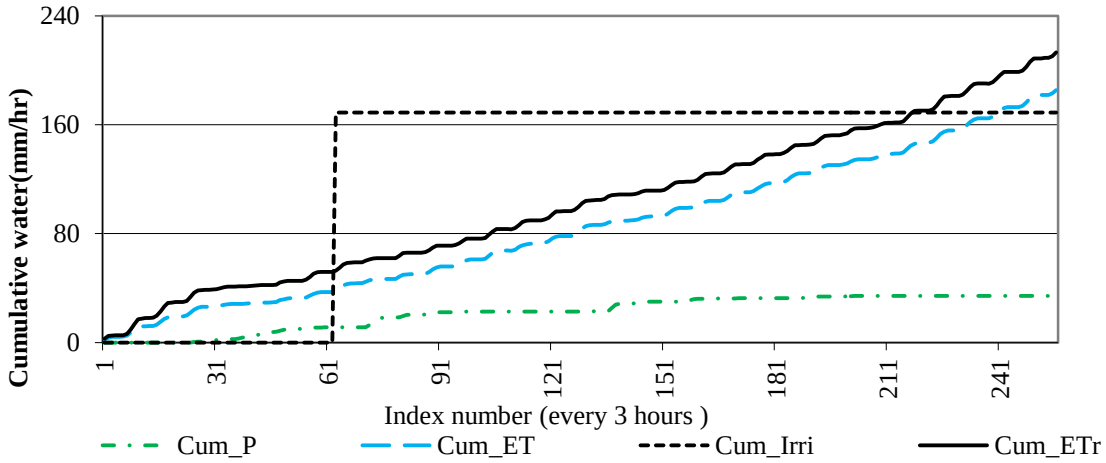

Fig. 2.16. Cumulative results of precipitation (Cum_P), ET (Cum_ET), irrigation (Cum_Irri), and reference ET (Cum_ET_r) for an irrigated agricultural pixel A1 (Land use: 82, NDVI: 0.71 to 0.83 and $f_{c:}$ 0.86 to 1) from 05/17/2008 to 06/18/2008

Figure 2.17 shows θ_{sur} and θ_{root} with the precipitation events. θ_{root} decreased gradually

after the irrigation event, and was about 0.2 m^3/m^3 at the end of the simulation period. Soil moisture at root (θ_{root}) responded gently to the low precipitation because the addition of water to θ_{root} was small compared to total water available at root zone. Soil moisture at surface (θ_{sur}) decreased rapidly after the irrigation event and dried out at the end of the simulation period, as there was no precipitation prior to the satellite overpass. Soil moisture at surface (θ_{sur}) responded quickly in the precipitation and irrigation events.

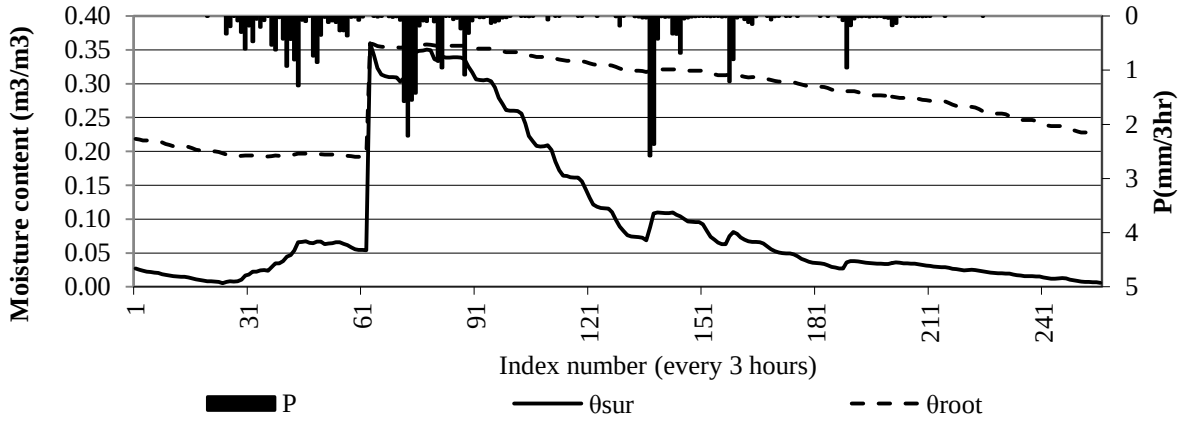

Fig. 2.17. Simulation results of soil moisture (θ_{sur}) at surface and root zone (θ_{root}) for an agricultural pixel A1 (Land use 82, NDVI: 0.71 to 0.83 and $f_{c:}$ 0.86 to 1) from 05/17/2008 to 06/18/2008

Figure 2.18 shows the simulation results of r_{ss} and r_{sc}. Soil surface resistance (r_{ss}) decreased rapidly at the time of precipitation and irrigation. The soil surface resistance reached a maximum value of 5000 s/m at the start of the simulated period (05/17/2008) and stayed low during the precipitation events. At the end of the simulation period, r_{ss} again elevated to the maximum allowed value of 5000 s/m, as there was no precipitation and irrigation. Canopy resistance (r_{sc}) has small values (~35 s/m) in the day time that increase at night because the F_1 function in the Jarvis-type equation becomes very small without solar radiation input. This creates a very large r_{sc} at night time. The maximum value of r_{sc} at night time gradually decreases and becomes fairly constant with an increase in LAI within the

pixel.

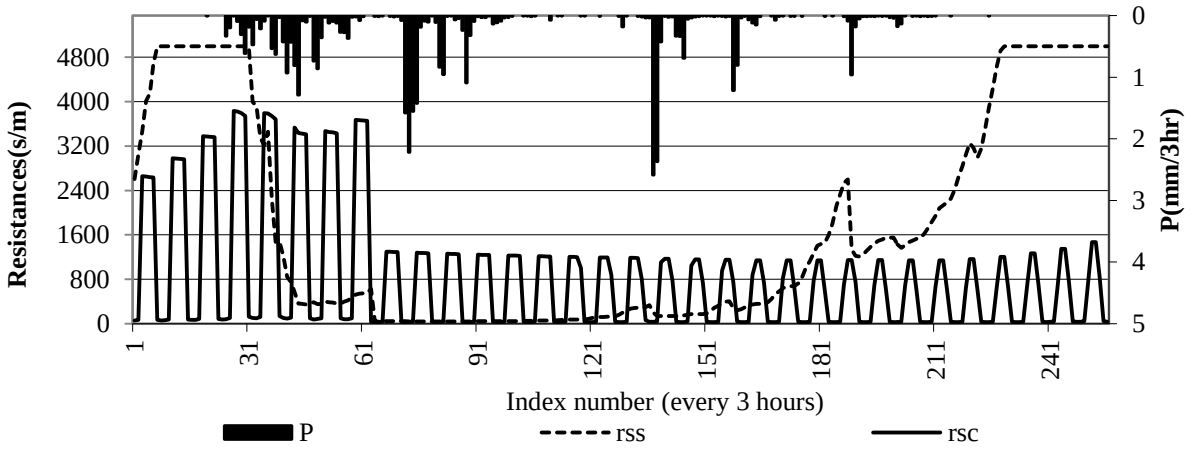

Fig. 2.18. Simulation results of soil surface resistance (r_{ss}) and canopy resistance (r_{sc}) for an irrigated agricultural pixel A1 (Land use 82, NDVI: 0.71 to 0.83 and f_c: 0.86 to 1) from 05/17/2008 to 06/18/2008

4.2.2 Desert Pixel D1 (Coordinates: 2601776, 1325307)

Figure 2.19 shows a comparison between simulated ET, E_{ss} and T for a desert pixel with NDVI of about 0.2. The simulated ET in the desert is low, naturally, (less than 0.3 mm/day) throughout the simulation period, as desert ET is more limited by precipitation than agricultural lands. Soil surface evaporation (E_{ss}) is high after light precipitation events in comparison to T, because of the low f_c in the desert. The contribution of T in the desert is fairly consistent within the simulation period; water that is transpiring comes from the d_{root}. After the precipitation events, ET rises about 0.3 mm/hr, becoming the maximum value for this simulation period. Simulated ET closely matches METRIC ET at the end of the simulation period.

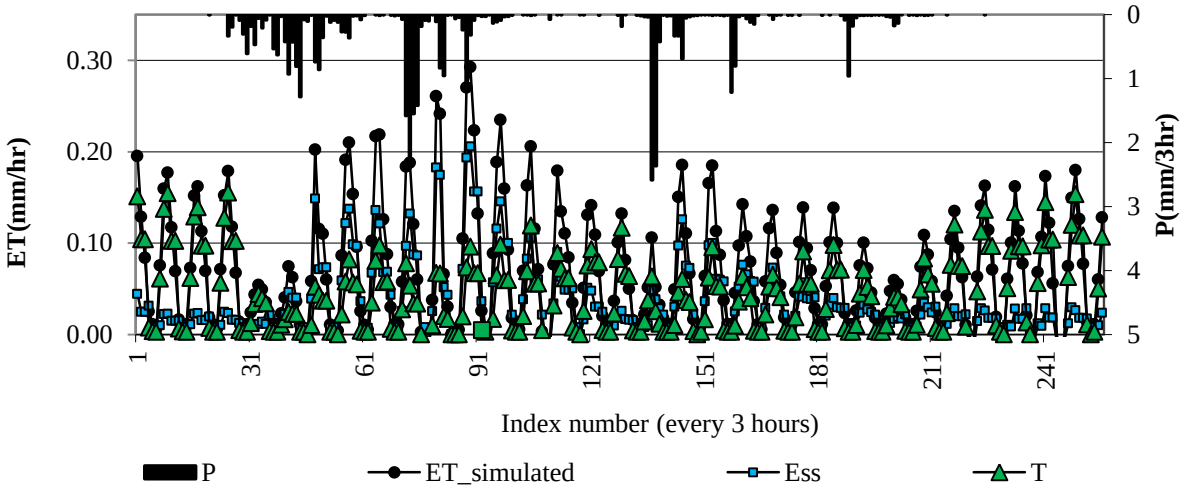

Fig. 2.19. Simulation results of combined ET (ET_simulated), soil evaporation (E_{ss}) and canopy transpiration (T) for a desert pixel D1 (Land use 52, NDVI = 0.2 to 0.17) from 05/17/2008 to 06/18/2008

Figure 2.20 shows the comparison between the simulated bulk surface temperature (T_b) and T_a, where T_b is larger than T_a during the day-time and smaller at night. Table 2.3 shows that the mean of T_b that is systematically smaller than METRIC thermal based surface temperature at the satellite overpass time. The maximum value of T_b is about 314 K in the simulation period, which is about 8 K less than thermal based radiometric temperature. T_b averaged about 309 K, which is smaller than the thermal based surface temperature at desert. This analysis also confirmed that BATANS is able to produce higher surface temperature in desert compared to air temperature and surface temperature of fully vegetated agricultural pixel in daytime.

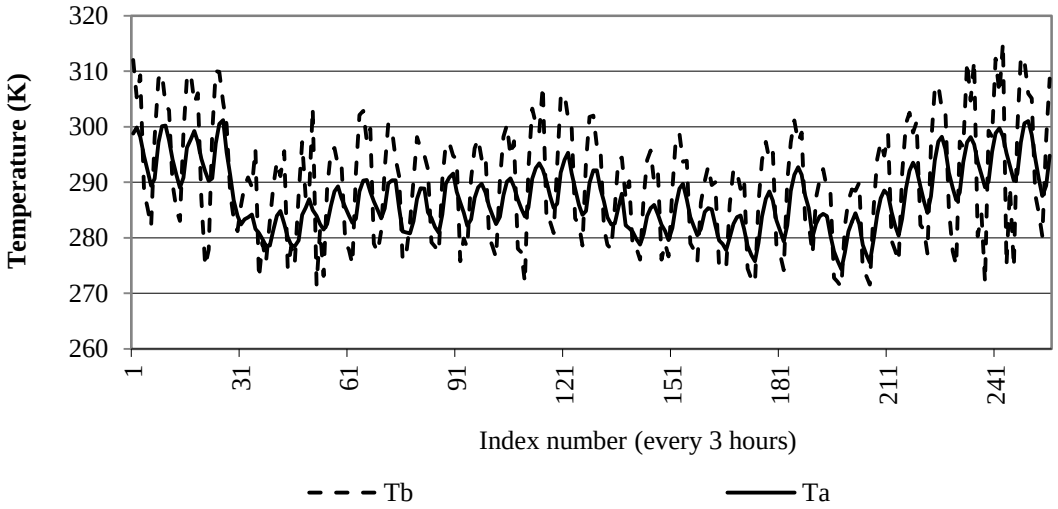

Fig. 2.20. Simulation results of bulk surface temperature (T_b) and air temperature from NARR reanalysis (T_a) for desert pixel D1 (Land use 52, NDVI: 0.2 to 0.17) from 05/17/2008 to 06/18/2008

Figure 2.21 shows the cumulative precipitation, ET and $ET_{r,}$ for desert pixel D1. Cumulative ET was about 19 mm higher than cumulative precipitation in this simulation period, probably because T is supplied by θ_{root} in the root zone.

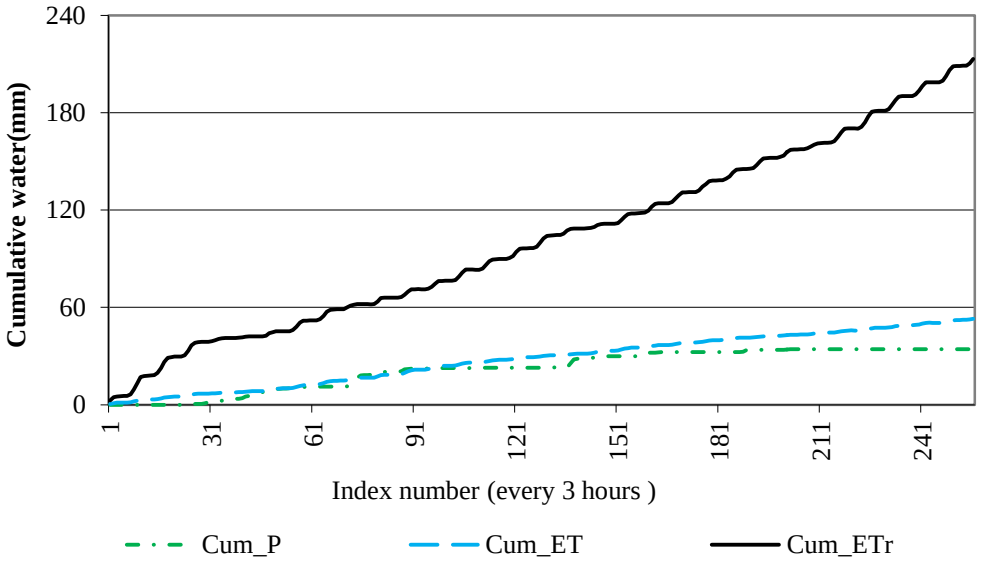

Fig. 2.21. Cumulative results of precipitation (Cum_P), ET (Cum_ET) and reference ET (Cum_ET_r) for a desert pixel D1 (Land use 52, NDVI: 0.2 to 0.17) from 05/17/2008 to 06/18/2008

Figure 2.22 shows θ_{sur} and θ_{root} for the desert pixel D1 during the entire simulation period. Soil moisture at the surface (θ_{sur}) abruptly rose and fell in response to precipitation events. Soil moisture at the root (θ_{root}) responded to precipitation much less quickly as the addition when the soil moisture at 2 m rooting depth was small. Soil moisture at the 2 m rooting depth steadily decreased from 0.204 m^3/m^3 to 0.19 m^3/m^3.

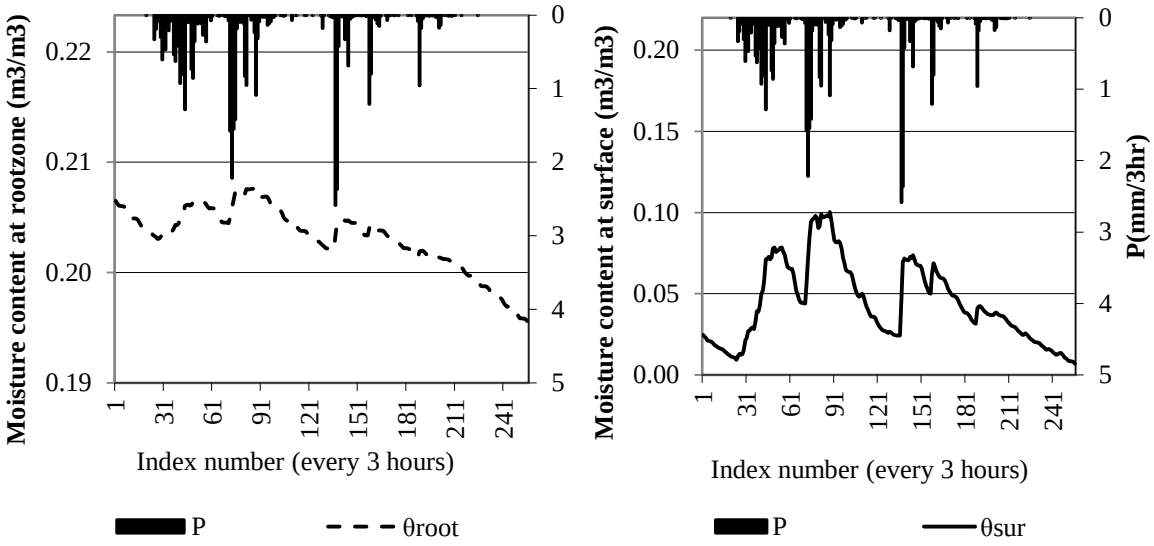

Fig. 2.22. Simulation results for soil moisture at the surface (θ_{sur}) and root zone (θ_{root}) for a desert pixel D1 (Land use 52, NDVI: 0.2 to 0.17) from 05/17/2008 to 06/18/2008

Figure 2.23 shows the comparison between r_{ss} and r_{sc} for pixel D1. Soil surface resistance (r_{ss}) decreased rapidly at the time of precipitation and irrigation and it reached a minimum value of 35 s/m. At the start and end of the simulation period, when there was no precipitation, r_{ss} reached a maximum allowed value of about 5000 s/m. Canopy resistance (r_{sc}) had very small values during the day time, but it increased at night because of the F_1 function at the Jarvis-type equation. The canopy resistance (r_{sc}) of pixel D1 during the day was found to be greater than that of pixel A1 because of the formulation of the Jarvis function. The desert vegetation may face greater transpiration resistance than cultivated, irrigated vegetation.

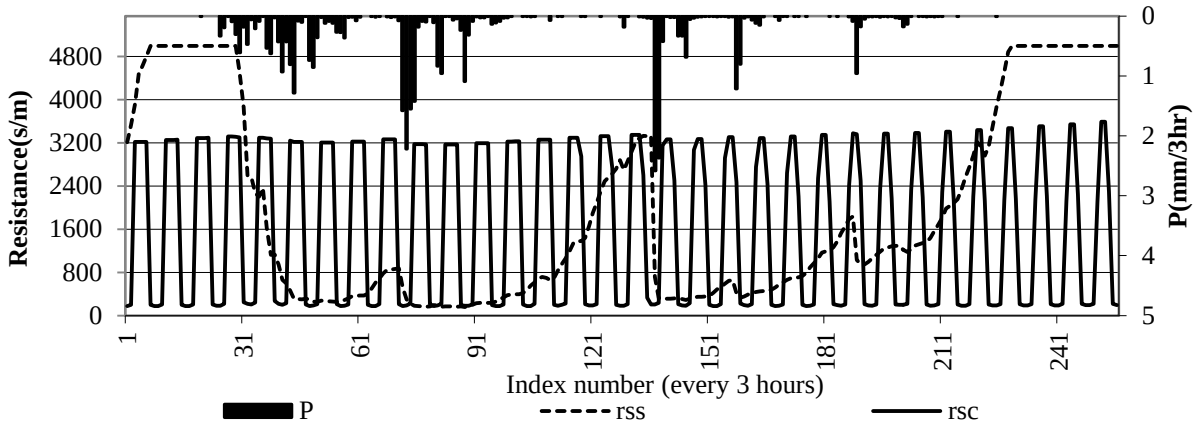

Fig. 2.23. Simulation results of soil surface resistance (r_{ss}) and canopy resistance (r_{sc}) for a desert pixel D1 (Land use 52, NDVI: 0.2 to 0.17) from 05/17/2008 to 06/18/2008

4.2.3 Irrigated Agricultural Pixel A2 (Coordinate: 2612319, 1332522)

Another simulation was carried out for different agricultural pixel, A2, which had lower NDVI than pixel A1. Figure 2.24 shows a comparison between the simulated ET, E_{ss}, and T with NDVI from 0.12 to 0.32 in the area where simulated ET is significantly lower than METRIC ET. The simulated ET of this pixel is smaller than that of pixel A1 because f_c is significantly smaller in A2. Soil surface evaporation (E_{ss}) was higher than T at the start of the simulation period because the irrigation was applied at 05/19/2008. When the soil became dry at the end of the simulation period, E_{ss} became very small and T gradually increased with an increase of f_c. The increase in T was not able to match METRIC ET because f_c was still very low and there were no irrigation or precipitation events at the end of the simulation period. METRIC ET at the end of the simulation period was about 0.72 mm/hr, while simulated ET was 0.21 mm/hr.

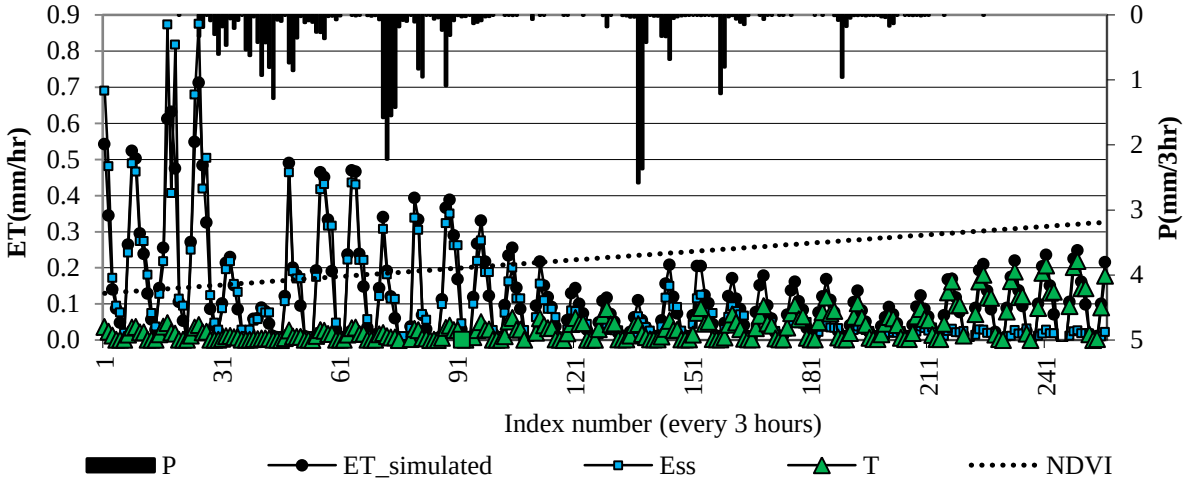

Fig. 2.24. Simulation results of combined ET (ET_simulated), soil evaporation (E_{ss}) and canopy transpiration (T) for an irrigated agricultural pixel A2 (Land use 82, NDVI : 0.12 to 0.32 and f_c : 0.05 to 0.27) from 05/17/2008 to 06/18/2008

Bulk surface temperature (T_b) was higher during the day and lower at night than T_a (fig. 2.25) because the soil surface of pixel A2 is largely exposed; T_b rose up to 315 K in the dry environment during the day time. The trend of the T_b in pixel A2 is similar to that of pixel D1, as both pixels have very small f_c.

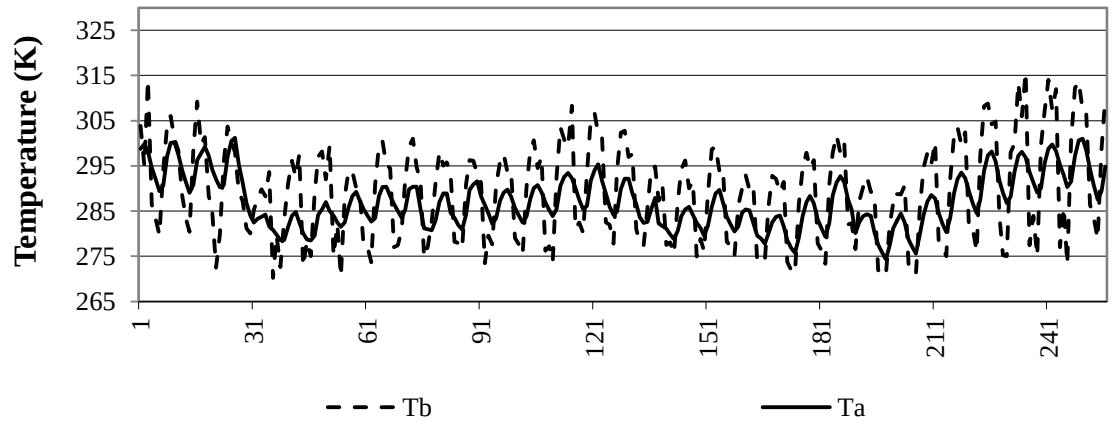

Fig. 2.25. Simulation results of bulk surface temperature (T_b) and air temperature (T_a) from NARR reanalysis for an irrigated agricultural pixel A2 (Land use 82, NDVI: 0.12 to 0.32 and f_c: 0.05 to 0.27) from 05/17/2008 to 06/18/2008

In pixel A2, cumulative ET_r has a greater difference than the cumulative ET in pixel A1 because ET is low throughout the simulation period (fig. 2.26). In pixel A2, irrigation was applied once at 05/19/2008, three days after the first satellite overpass. The total ET of the simulation period was about 88 mm.

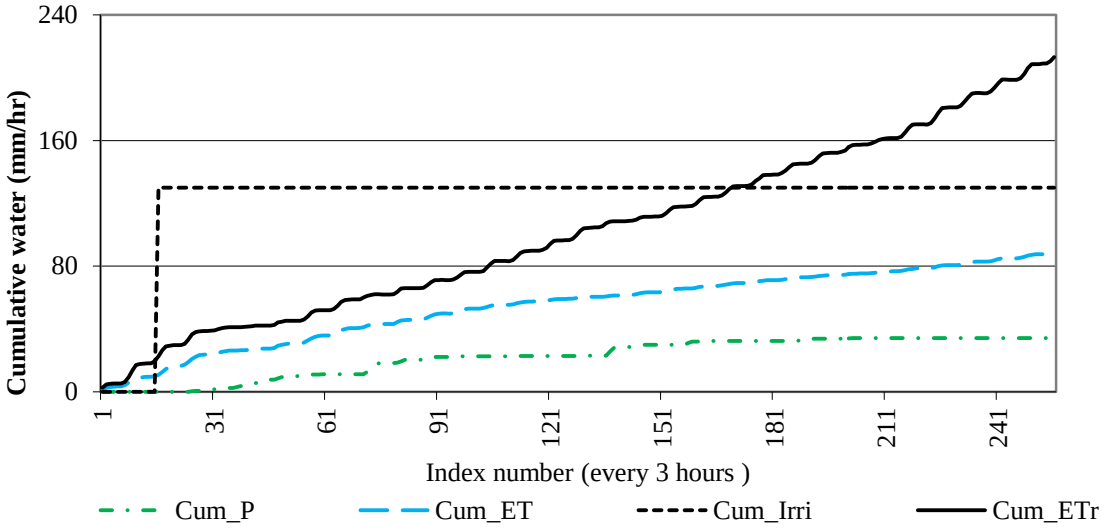

Fig. 2.26. Cumulative results of precipitation (Cum_P), ET (Cum_ET), irrigation (Cum_Irri), and reference ET (Cum_ETr) for an irrigated agricultural pixel A2 (Land use 82, NDVI: 0.12 to 0.32 and $f_{c:}$ 0.05 to 0.27) from 05/17/2008 to 06/18/2008

4.2.4 Degree of Agreement and Distribution of Error

After ET was extrapolated between the two satellite overpass dates, a comparison between simulated and METRIC ET was conducted. The degree of agreement between the results is evaluated using different statistical techniques which were discussed in section 4.1. This was done to validate the model and to reduce the error between simulated and METRIC ET, it is necessary to analyze the effects of individual variables and conditions on the simulation process. Assuming the trend in ET from BATANS is correct, a triangular interpolation method may be used to adjust these errors to all points within the simulation period. Figure 2.27 shows the triangular method of error distribution, assuming that there is

no error at the beginning of the simulation and maximum error at the end of simulation, the next satellite overpass date.

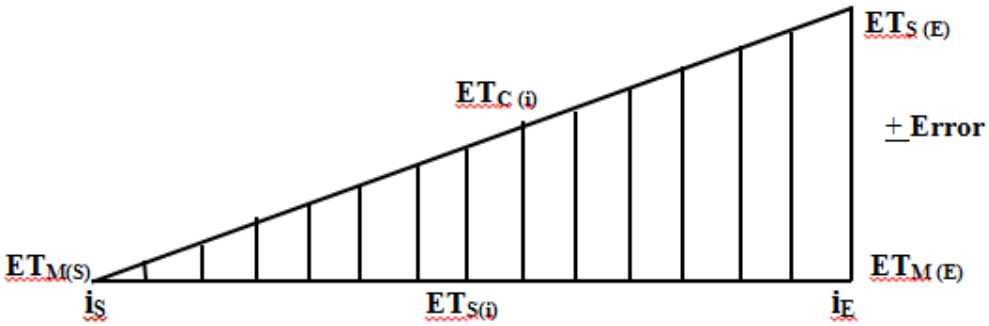

Fig. 2.27. Error distribution using triangular interpolation method

where $ET_{M(S)}$ is the METRIC ET at the start of the simulation (mm/hr), $ET_{C\ (i)}$ is corrected ET for every three hour time step (i) (mm/hr), $ET_{S\ (i)}$ is simulated ET for every three hours' time step (i) (mm/hr), $i_{(S)}$ is the start index of current satellite overpass date, and $i_{(E)}$ is the end index of next satellite overpass date.

In this process, error (E_{rr}) between the simulated ET ($ET_{S\ (E)}$) and METRIC ET ($ET_{M(E)}$) is computed for the next satellite overpass time in mm/hr (06/18/2008). Once a corrected ET at the next satellite overpass time is obtained, ET is adjusted linearly. The assumption was made that the error grows at a constant rate. Index number (i) is a measure of the distance between the current and the next satellite overpass date for every three hours. Simulated ET (ET_s) for every three hour time step is corrected using the second term of eqn. (21), where height is associated with error in ET (mm/hr).

$$ET_{C(i)} = ET_{S(i)} - E_{rr}\left(\frac{i - i_{(S)}}{i_{(E)} - i_{(S)}}\right) \tag{21}$$

E_{ss} and T are written in separate equations so that their errors may be computed and corrected. After correction, METRIC and the corrected ET have identical values with an R^2 value of 1 at the end of the simulation (06/18/2008). Figure 2.28 shows the error map at the

end of the simulation period. As per assumption, the maximum error occurs on the end of the simulation period (06/18/2008), and it is simply the difference between the simulated and METRIC ET.

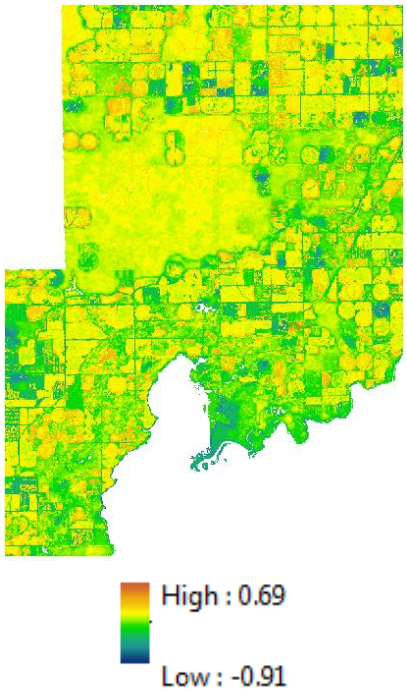

Fig. 2.28. Error map (mm/hr) at the end of simulation period i.e. 06/18/2008 approximately at 11 am in southern Idaho, near American Falls

4.3 Correction of Hourly and Daily Evapotranspiration (ET)

In the following section, the adjusted ET from the above procedure is examined. Figure 2.29 shows the comparison of simulated ET to the corrected ET for the irrigated agricultural pixel A1. The simulated ET needs very little correction in pixel A1, as BATANS is able to simulate relatively accurate ET in higher NDVI irrigated agricultural land although it struggles with low NDVI pixels.

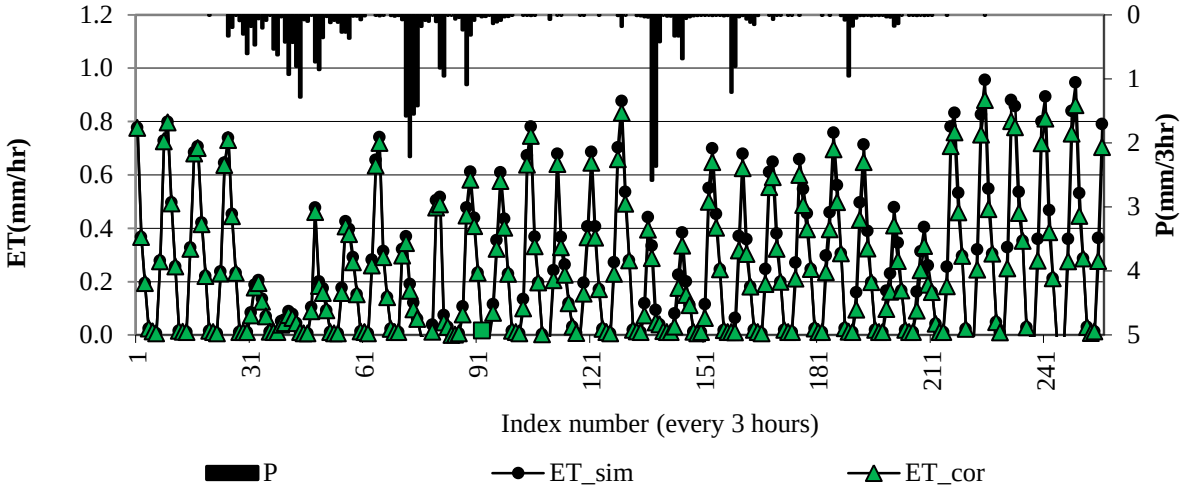

Fig. 2.29. Simulation results of combined ET before correction (ET_sim) and after correction (ET_cor) for an irrigated agricultural pixel A1 (Land use 82, NDVI: 0.71 to 0.83 and f_c: 0.86 to 1) from 05/17/2008 to 06/18/2008

Figure 2.30 shows the desert pixel D1, which also needed a small correction to match METRIC ET in most of the time steps within the simulation period. BATANS was able to simulate relatively accurate ET in the sage brush desert and grassland regions, even if the temperature differences in these land use classes were high.

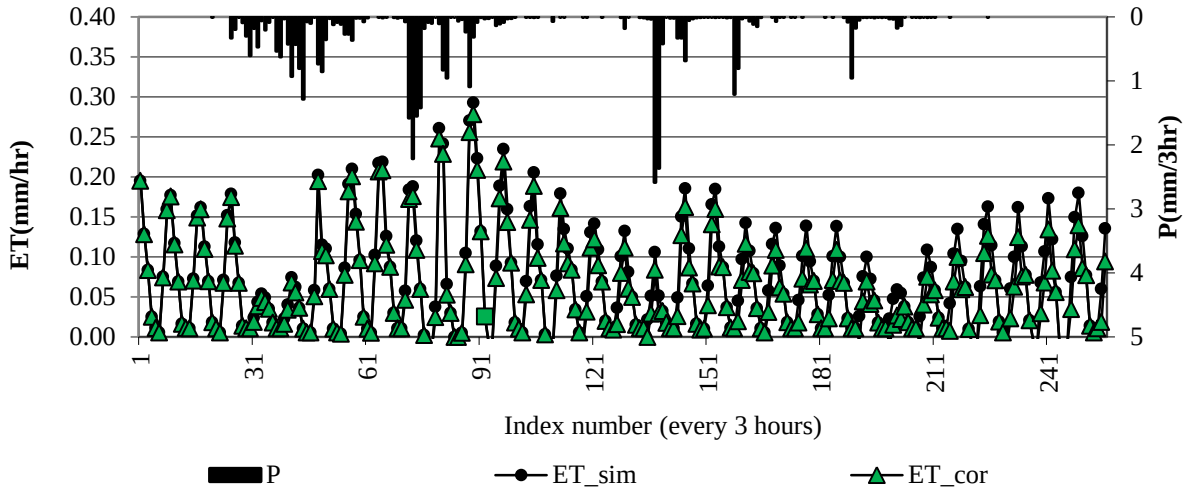

Fig. 2.30. Simulation results of combined ET before correction (ET_sim) and after correction (ET_cor) for a desert pixel D1 (Land use 52, NDVI: 0.2 to 0.17, f_c: 0.28) from 05/17/2008 to 06/18/2008

Irrigated agricultural Pixel A2 needs substantial correction because the simulated model has lower values of ET than METRIC ET. Figure 2.31 shows that the simulated ET elevated about 0.8 mm/hr after the irrigation and ET increased rapidly after precipitation events even though the f_c in this pixel is low. This indicates that the influence of NDVI by f_c in the simulation result is not the cause of low ET in this pixel at the end of the simulation period. Simulated ET is lower than METRIC ET at the end of the simulation period because of the possible mismatch in irrigation, as there is no irrigation and precipitation at the end of the simulation period.

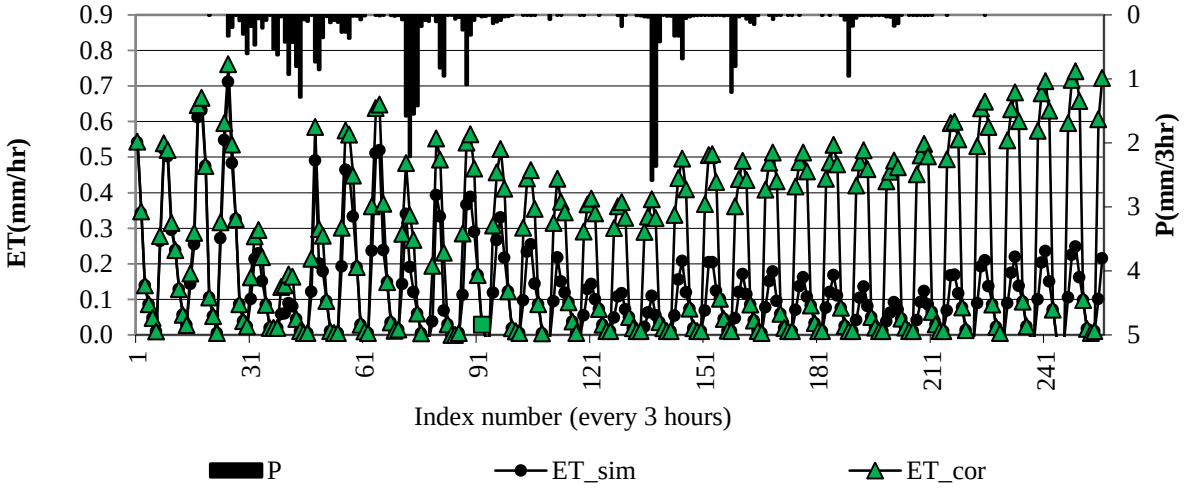

Fig. 2.31. Simulation results of combined ET before correction (ET_sim) and after correction (ET_cor) for an irrigated agricultural pixel A2 (Land use 82, NDVI: 0.12 to 0.32 and f_c: 0.05 to 0.27) from 05/17/2008 to 06/18/2008

As indicated earlier section, the main objective of BATANS is to extrapolate ET in between the satellite overpass dates. The METRIC model computes daily ET in between the satellite overpass dates with the mathematical spline interpolation of ET_rF. Figure 2.32 shows the daily ET_rF between the satellite overpass dates before and after the correction and the METRIC interpolated ET_rF for agricultural pixel A1. Simulated ET_rF is able to incorporate the variations in the meteorological conditions compared to METRIC ET_rF. At the same time, the correction of ET_rF is achieved using the previously discussed error distribution procedure.

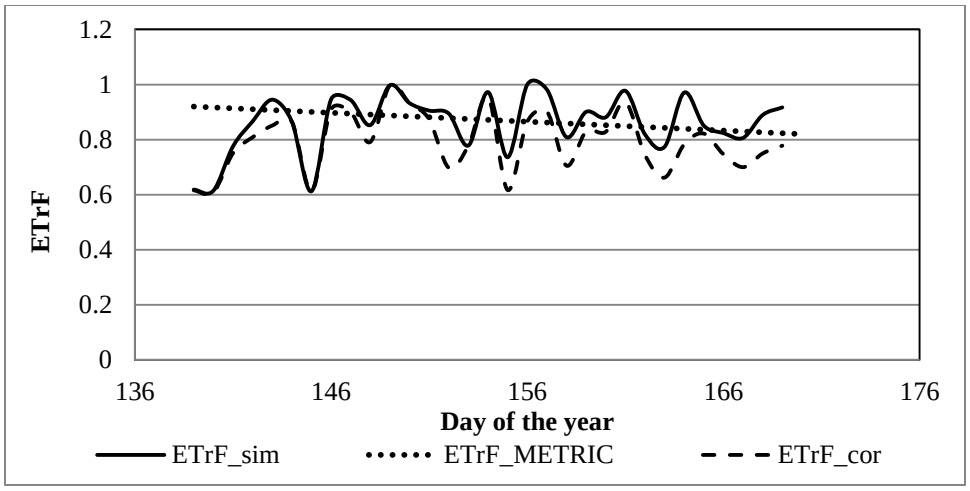

Fig. 2.32. Simulation results of daily ET_rF before correction (ET_rF_sim) and after correction (ET_rF_cor) and daily METRIC ET_rF (ET_rF_METRIC) for an irrigated agricultural pixel A1 (Land use 82, NDVI: 0.71 to 0.83 and f_c: 0.86 to 1) from 05/17/2008 to 06/18/2008

Figure 2.33 shows the simulated ET_rF, corrected ET_rF and METRIC ET_rF for the irrigated agricultural pixel A2. After the correction, simulated ET_rF is similar to METRIC ET_rF at the end of the simulation period. These inconsistencies are possibly due to the mismatch in irrigation time, as discussed in an earlier section, daily simulated ET_rF at the end of the simulation period is low. However, ET_rF from METRIC shows higher values at the start and end of the simulation period.

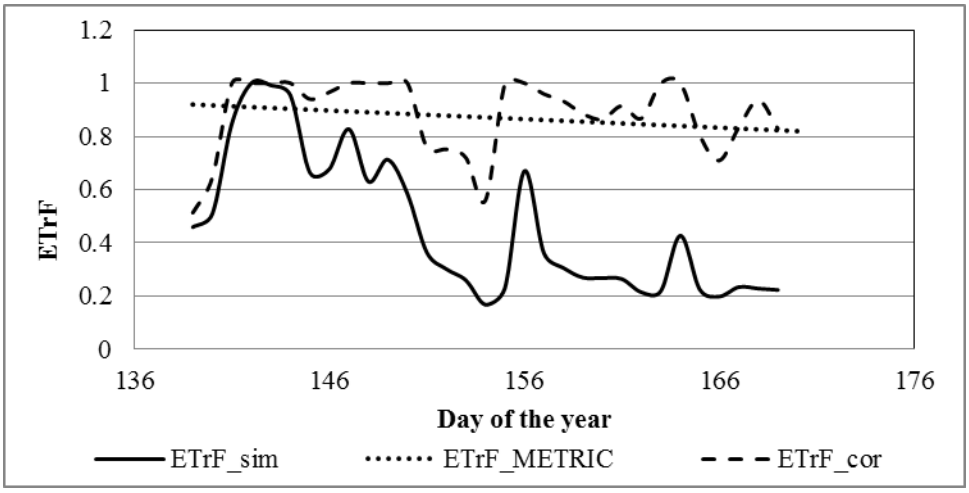

Fig. 2.33. Simulation results of daily ET_rF before correction (ET_rF_sim) and after correction (ET_rF_cor) and daily METRIC ET_rF (ET_rF_METRIC) for an irrigated agricultural pixel A2 (Land use 82, NDVI: 0.12 to 0.32 and f_c: 0.05 to 0.27) from 05/17/2008 to 06/18/2008

5.0 Conclusions

A two source surface energy balance model was developed to extrapolate ET between the two satellite overpass dates, when no Landsat image or thermal based surface temperature map was available. The extrapolation is driven by NARR reanalysis data sets and parameterized and initialized using the Landsat based METRIC ET data set. The developed model was tested in southern Idaho from 05/17/2008 to 06/18/2008. It was able to simulate ET every three hours for the simulation period and produce reasonable values. A scatter plot of surface energy fluxes between the simulation and METRIC showed some variation in data, but the means of the fluxes were similar; within one standard deviation for most fluxes. The irrigation model supplied water to the known irrigated agricultural lands when soil moisture was below a threshold. However, the pattern of irrigation and actual irrigation time in the field was stochastic in nature. A mismatch in the irrigation timing caused by the assumption of constant rooting depth possibly created differences between the simulated and METRIC ET when NDVI was low and the opportunity for differences in evaporation due to

differences in irrigation timing were high. The Jarvis-type function was able to simulate lower values of r_{sc} in irrigated agricultural areas.

The soil water balance model was able to track soil moisture at the root zone and surface. The simulated surface temperature matched closely to the thermal based temperature in agricultural areas. Simulated surface temperature from the aerodynamic equation with aerodynamic resistance was not able to explain the high temperatures in the desert. METRIC ET was the target ET at the end of the simulation period and the distribution of error was done according to the difference from METRIC ET. Any mismatch between simulated ET and METRIC ET at the end of the simulation period was corrected for each time step, preserving the pattern of ET with a linear time-based-proportioning method.

References

Allen R. G., 2013. Irrigation Water Requirements. Personal communication.

Allen, R. G., Pereira, L. S., Raes, D., and Smith, M., 1998. Crop evapotranspiration; Guidelines for computing crop water requirements. FAD Irrigation and Drainage Paper No. 56, Rome, Italy.

Allen, R.G., Tasumi, M. and Trezza, R., 2007. Satellite-based energy balance for mapping evapotranspiration with internalized calibration (METRIC) – Model. *ASCE J. Irrigation and Drainage Engineering* 133(4):380-394.

Bastiaanssen, W. G. M., Menentia, M., Feddesb R.A. and Holtslagc, A. A. M., 1998. A remote sensing surface energy balance algorithm for land (SEBAL). 1. Formulation .Journal of Hydrology 212–213 (1998) 198–212.

Budyko, M. I., 1956. Heat Balance of the Earth's Surface, Gidrometeoizdat, Leningrad, 255 pp. (in Russian).

Choudhury, B. J. and Monteith, J. L., 1988. A four layer model for the heat budget of homogenous land sufaces. Q.J.R. Meterological Soc.

Colaizzi, P. D., Kustas, W. P., Anderson, M. C., Agam, N., Tolk, J. A., Evett, S. R., Howell, T. A., Gowda, P. H. and O'Shaughnessy, S. A., 2012. Two-source energy balance model estimates of evapotranspiration using component and composite surface temperatures. Adv. Water Res.

Crow, W. T., Kustas, W. P. and Prueger, J. H., 2006. Monitoring root-zone soil moisture through the assimilation of a thermal remote sensing-based soil moisture proxy into a water balance model. Elsevier Science.

Deardorff, J. W., 1977. A parameterization of ground surface moisture content for use in atmosphere prediction model. J. Appl. Met. 16, 1182-1185.

Deardorff, J. W., 1978. Efficient prediction of ground surface temperature and moisture with inclusion of a layer of vegetation, J. Geophys. Res. 83(C4): 1889–1903.

Dhungel, R. and Allen, R., 2014a. Parameterization of soil moisture and vegetation characteristics with a two source surface energy balance model using NARR and METRIC data sets at satellite overpass time. Ph.D. Dissertation, University of Idaho.

Dickinson, R. E., 1984. Modeling evapotranspiration for the three-dimensional global climate models. Hansons, JE., and Takahashi, T. (eds.), Climate Processes and Climate Sensitivity, Amer. Geophys. Union, Washington, DC, pp.58-72.

Er-Raki, S., Chehbouni, A., Hoedjes, J., Ezzahar, Duchemin, J., B., and Jacob, F., 2008. Improvement of FAO-56 method for olive orchards through sequential assimilation of thermal infrared-based estimates of ET. Agric. Water Mgmt. 97(11): 1769-1778.

http://directives.sc.egov.usda.gov/OpenNonWebContent.aspx?content=18359.wba <accessed 2013>.

http://landcover.usgs.gov/classes.php <accessed oct. 2013>.

http://nomads.ncdc.noaa.gov/ <accessed oct. 2011>.

Hunsaker, D. J., Pinter Jr., P. J., Barnes, E. M., and Kimball, B. A., 2003. Estimating cotton evapotranspiration crop coefficient with a multispectral vegetation index, Irrigation Sci., 22, 95–104.

Irannejad , P. and Shao, Y., 1998. Description and validation of the atmosphere–land–surface interaction scheme ALSIS with HAPEX and Cabauw data. Global and Planetary Change 19 1998 87–114.

Jarvis, P. G., 1976. The interpretation of the variation in leaf water potential and stomatal conductance found in canopies in the field. Philos Trans R Soc Lond B 273: 593–610

Johnson, C. G. and Swanson, D. K., 2005. Bunchgrass Plant Communities of the Blue and Ochoco Mountains: A Guide for Managers.

Lee, D. H. and Abriola, L. M., 1999. Use of the Richards equation in land surface parameterizations. J. Geophys. Res., 104 (1999), pp. 27519–27526.

Legates, D. R. and McCabe Jr, G. J.., 1999. Evaluating the Use of "Goodness-of-Fit" Measures in Hydrologic and Hydroclimatic Model Validation, Water Resour. Res., 35(1), 233–241.

Li, F., Kustas, W. P., Prueger, J. H., Neale, C. M. U. and Jackson, T. J., 2005. Utility of remote sensing based two-source energy balance model under low and high vegetation cover conditions. J. Hydrometeorol. 6, 878–891.

Manabe, S., 1969. Climate and the ocean circulation - Part 1: The atmospheric circulation and the hydrology of the earths surface. Mon. Wea. Rev. 97, 739774.

McNaughton, K. G., and van den Hurk, B. J. J. M., 1995. A ‘Lagrangian’ revision of the resistors in the two-layer model for calculating the energy budget of a plant canopy. Boundary-layer Meteorol. 74:261–288.

Mesinger, F. and Coauthors, 2006. North American Regional Reanalysis. Bull. Amer. Meteor. Soc., 87, 343-360.

Milly, P. C. D., 1992. Potential evaporation and soil moisture in general circulation models. J. climate, 5, 209-226.

Noilhan, J. and Mahfouf, J. F., 1996. The ISBA land surface parameterization scheme. Global and Plan. Change, 13, 145-159.

Norman, J. M., Kustas, W. P., Humes, K. S., 1995. Source approach for estimating soil and vegetation energy fluxes in observations of directional radiometric surface temperature. Agric. For. Meteorol. 77, 263-293.

Raupach, M. R., 1989. A practical Lagrangian method for relating concentrations to source distributions in vegetation canopies. Quart. J. R. Meteorol. Soc. 115:609–632.

Richards, J. H. and Caldwell, M. M., 1987. Hydraulic lift: substantial nocturnal water transport between soil layers by Artemisia tridentata. Oecologia. 73(4): 486-489.

Robson, S. and Kingery, J., 2006. Idaho Native Plants for Roadside Restoration and Revegetation Programs.

Schaake, J. C., Koren, V. I., Duan, Q. Y., Mitchell, K., and Chen, F., 1996. Simple water balance model for estimating runoff at different spatial and temporal scales, J. Geophys. Res., 101(D3), 7461 – 7475.

Sellers, P. J., Mintz, Y., Sud, Y. C., and Dalcher, A., 1986. A simple biosphere model (SiB) for use within general circulation models, *J. Atmos. Sci*., 43, 505-531.

Shuttleworth, W. J. and Wallace, J. S., 1985. Evaporation from sparse crops-an energy combination theory. Quart. J.R. Met. Soc.

Sun, S.F., 1982. Moisture and heat transport in a soil layer forced by atmospheric conditions, M.S. thesis, Dept. of Civil Engineering, University of Connecticut, 72 pp.

Wang, Q., and Peng, M.S., 2010. Evaluation and Improvement of High-resolution Mesoscale Models on Boundary Layer Simulations Using Ground-based Observations. Ft. Belvoir : Defense Technical Information Center, 30 SEP 2009.

Yang, Z. L., Dickinson, R. E., Henderson-Sellers, A. and Pitman, A.J., 1995. Preliminary study of spinup processes in land surface models with the first stage data of Project

for Intercomparison of Land Surface Parameterization Schemes Phase 1(a). J. Geophys. Res. 100:16553–16578.

Chapter 3: Comparisons between the FAO-56 Soil Water Evaporation Model and HYDRUS-1D Evaporation Model over a Range of Soil Types

By

Ramesh Dhungel and Richard G. Allen

Abstract

A simple 'slab' evaporation model by the United Nations Food and Agriculture Organization (FAO-56) was compared against the more sophisticated finite element Hydrus-1D model to determine the relative performance of the simple FAO-56 model over a range of soil types, time series and wetting conditions. The FAO-56 model was applied with and without a skin evaporation enhancement. Soil water balances and estimated evaporation rates from the FAO-56 evaporation model with the skin evaporation enhancement matched closely with those simulated by the Hydrus-1D model for several soil types. In a separate test, simulations from both FAO-56 and Hydrus-1D models had good agreement with evaporation measured from a weighing lysimeter. Both hourly and daily timesteps were evaluated with the FAO-56 model. Both timesteps sufficiently explained the observed evaporation rates and estimations by the Hydrus-1D model that employs a timestep-optimization strategy. The root mean square error of daily average evaporation estimates by the original and enhanced FAO-56 models were 0.67 mm/day and 0.27 mm/day respectively, when compared to Hydrus-1D for a silt loam soil and an h_{ini} (h_{ini}) of -3 m. The R^2 of the FAO-56 model with and without skin evaporation enhancement vs. the Hydrus-1D model was about 0.88 and 0.22 respectively when applied to daily calculation timestamps for an h_{ini} of -3 m. The R^2 for hourly data summed to daily averages varied from 0.82 to 0.90 for the silt loam soil over a

range of estimates of readily evaporable water, REW. In general, the FAO-56 model with skin enhancement and implicit stage 1 – stage 2 transition produces estimates of daily E that are similar to those of Hydrus-1D using both daily and hourly calculation timesteps for the FAO-56 model. This is a useful finding and indicates that models incorporating the FAO-56 procedure should generally provide accurate accounting for E.

1.0 Overview

Water balance is important in many hydrologic studies for quantifying the amount of surface water or ground water that is evaporated, transpired or contributes to ground water recharge. Water balance computations are important in agricultural areas to understand and quantify the water available for crop production in both temporal and spatial dimensions. Efficient use of water in agricultural fields is enhanced by the accurate calculation of evapotranspiration (ET). Evaporation of water from bare soil is an important, but challenging component of ET estimations, and is routinely estimated in operational models.

The FAO-56 soil water balance model Allen et al., 1998, 2005 has been widely used as an approximate estimate of evaporation (Hunsaker et al., 2002, Howell et al., 1995, Burt et al., 2002, Mutiziger et al., 2005, Allen, 2011). The FAO-56 model computes a soil water balance of the upper soil profile (0.10 to 0.15 m), under the assumption that the soil surface layer functions as an evaporative slab that gains and loses water from precipitation, infiltration, and evaporation events. The slab model functions as a fully mixed layer so that small additions of precipitation (P) get mixed completely into the slab. The complete mixing can incorrectly dampen evaporation spikes following small wetting amounts as compared to measured values (Allen, 2011). Therefore, Allen (2011) extended the basic FAO-56 slab model to incorporate an additional shallow skin layer at the soil surface that can hold small

amounts of precipitation near the surface that can release the water quickly as stage 1 evaporation.

Comparisons between the original and extended FAO-56 model outputs with lysimeter measurements and against using the more theoretical and rigorous Hydrus-1D model of Simunek et al. (2008) provides a useful insight into the behavior of the FAO-56 model and extension for both small and extended evaporation events. The Hydrus-1D model computes soil water flow by solving the Richards Equation (eqn. (12)) with specified boundary conditions. The main objective is to compare the relatively simple FAO-56 model, enhanced with skin evaporation, to the Hydrus-1D model outputs under different environmental conditions and soil types. The following section describes the FAO-56 model with the skin evaporation enhancement and the Hydrus-1D model.

1.1 FAO-56 with Skin Evaporation Enhancement

The FAO-56 evaporation model is a simple slab model intended for use in routine operational models used in irrigation scheduling or for determining crop water requirements (Allen et al. 1998, 2005). The model has low data requirements, requiring only field capacity and wilting point of the surface soil layer and weather-based reference ET. The model can be operated on hourly or daily time steps. The evaporation rate is expressed as a function of the water content, or depletion from the soil slab that is generally assumed to be 0.10 to 0.15 m in depth. The amount of water stored in the slab is the sum of the water stored at the end of the previous period plus any rainfall or irrigation inputs and less evaporation. Water stored in the soil slab is constrained between water content at air dry and field capacity (θ_{fc}). The air dry content is generally approximated as one-half of the water content at the wilting point (θ_{wp}) (Allen et al., 1998). The maximum storage is termed total evaporable water (TEW, eqn.

(5)).

The FAO-56 model follows a two stage approach where stage 1 is defined as an energy limited stage where evaporation is at a maximum rate limited by energy availability at the soil surface, and stage 2 is a falling rate stage that occurs when the cumulative depth of evaporation (depletion) from the soil surface layer exceeds the maximum evaporation depth occurring during stage 1. That maximum evaporation depth (mm) during stage 1 is known as readily evaporable water (REW) and is the maximum depth of water that can be evaporated from the soil surface layer without hydraulic restriction. Stage 1 evaporation generally follows an irrigation or rainfall event. During stage 1, where depletion from the soil surface layer (D_e) is less than REW:

$$E_1 = K_{emax}\, ET_r \tag{1}$$

where E_1 is the evaporation rate during stage 1, and K_{emax} describes the potential rate of evaporation, relative to the reference ET. ET_r is reference evapotranspiration (ET) which changes hourly or daily according to weather conditions. Reference ET is defined as the ET rate from an extensive surface of uniform, well watered vegetation and represents a near maximum, surface-energy-controlled ET rate. Values for K_{emax} range from 1.05 to 1.2 when applied with a clipped grass reference, ET_o, and 0.8 to 1.0 when applied to the taller alfalfa reference, $ET_{r,}$ (Allen et al., 2005). The higher values for K_{emax} apply when a dry soil slab has been heated by solar radiation prior to the wetting event.

In stage 2 drying, where D_e > REW, the evaporation rate is assumed in the FAO-56 model to decrease in proportion to the water remaining in the top soil layer:

$$E = K_e ET_r = K_r\, K_{e\,max} ET_r \tag{2}$$

$$K_e = K_r\, K_{e\,max} \tag{3}$$

$$K_r = \min\left[\frac{(TEW - D_{e(i-1)})}{(TEW - REW)}, 1.0\right] \quad (4)$$

where K_r is a soil evaporation reduction coefficient that is multiplied by the potential evaporation rate. $D_{e\ (i-1)}$ is the cumulative depth of evaporation (depletion) from the soil surface layer at the end of time step (i-1). The minimum of the two values separated by the comma in the 'min [ ]' function restricts K_r to less than or equal to 1.0. Figure 3.1 shows the soil water evaporation of stage 1 and stage 2 of the FAO-56 model expressed as K_r. Units for TEW, REW and $D_{e\ (i-1)}$ are in mm.

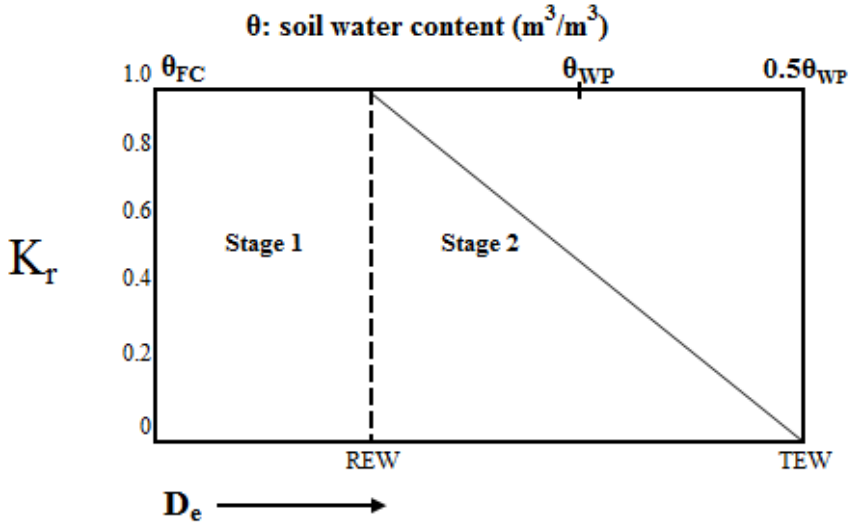

Fig. 3.1. Soil water evaporation from Stage 1 and Stage 2 in the FAO-56 model (Allen et al., 1998)

The FAO-56 estimates TEW from the soil slab using data for θ_{fc} and θ_{wp}, soil parameters that are commonly available:

$$TEW = 1000(\theta_{fc} - 0.5\theta_{WP})Z_e \ \min\left[\sqrt{\frac{ET_o}{5}}, 1.0\right] \quad (5)$$

where Z_e is the assumed effective depth of the surface soil layer that dries completely by evaporation, m. The 'min [ ]' function selects the minimum of the two values separated by

the comma. In Allen et al., (1998, 2005), the value of TEW during winter or other cool periods was reduced by the $(ET_o/5)^{0.5}$ multiplier to approximate reductions in potential drying depth during those periods when less radiation energy is available for heating the soil surface layer and supplying energy for evaporation. Consequently, the effective depth of drying decreases.

Ritchie et al. (1989) proposed potential values for REW based on soil texture, with values ranging from 4 to 10 mm. Allen and Robison (2007) proposed estimating REW from TEW as:

$$\mathrm{REW} = \min \begin{bmatrix} 2 + \dfrac{\mathrm{TEW}}{3}, \\ 0.8\ \mathrm{TEW} \end{bmatrix} \tag{6}$$

where TEW and REW are in mm.

The FAO slab model is designed for application in a dual evaporation (E) + transpiration (T) process where calculation of T is determined separately. However, because evaporation is the focus of this paper, the following equations governing E assumed that the soil surface is completely bare and that T is zero. In the soil water balance used to estimate K_r, cumulative depletion depth (D_{ei}) , mm, at the end of timestep i , applied to hourly or daily timesteps is (Allen 2011):

$$0.0 \le \mathrm{D_{e_i}} = \mathrm{D_{e_{i-1}}} - [(1 - \mathrm{f_b})(\mathrm{P_i} - \mathrm{RO_i} + \mathrm{I_i}) + \mathrm{f_b}(\mathrm{P_{i+1}} - \mathrm{RO_{i+1}} + \mathrm{I_{i+1}})] + \mathrm{E_i} \le \mathrm{TEW} \tag{7}$$

where $D_{e\ i-1}$ is cumulative depth of evaporation (depletion) from the soil surface layer at the end of timestep i-1, P_i is precipitation at the surface during time step i (mm), RO_i is surface runoff (mm), I_i is irrigation depth that, in eq. (7) is assumed to infiltrate over the entire soil surface. Parameter f_b is the fraction of the P and I occurring during a time step that contributes to E during the same time step (f_b = 0 to 1), and 1- f_b is the fraction of P and I whose wetting effect does not impact E until the next time step. E_i is the evaporation rate for

timestep i computed from eqn. (1) or (2). Infiltration in excess of $D_{e\ i,}$ is passed to below the slab layer into the soil profile below. No return of that water is permitted. Allen et al. (1998, 2005) and Allen (2011) give modifications to eqn. (7) for situations where vegetation is present.

Evaporation rates associated with light wetting events (less than 5-10 mm) are treated by the FAO-56 model skin evaporation enhancement of Allen (2011). That enhancement accounts separately for surface wetness of the skin of the soil surface where the stage 1 evaporation is assumed to be stored. The depletion of REW is accounted for by an additional state variable D_{REW} that represents depletion from the skin layer. The water balance for the skin layer is computed similar to eqn. (7) as:

$$0.0 \leq D_{REW_i} = D_{REW_{i-1}} - [(1 - f_b)(P_i - RO_i + I_i) + f_b(P_{i+1} - RO_{i+1} + I_{i+1})]C_{eff} + E_i \leq REW \quad (8)$$

Most variables in eqn. (8) are the same as for eqn. (7). D_{REWi} is constrained between 0 and REW. Infiltration in excess of D_{REW} is passed below the skin layer and mixed into the evaporation slab. The spatial infiltration efficiency factor (C_{eff}) represents the effectiveness of the skin layer in capturing and retaining P and I additions without any bypass flow. In most applications, the value for C_{eff} is set to 1.0 assuming that water flows deeper in soil only after fully recharging the skin layer.

Allen (2011) modified eqn. (3) when applied to daily timesteps to improve the estimated transition from stage 1 to stage 2 drying and the impact on the value for K_e on the day of the transition:

$$K_e = f_w[F_t + (1 - F_t)\ K_r]\ K_{e\ max} \quad (9)$$

where F_t is the fraction of the timestep interval that resides in stage 1:

$$F_t = \min \begin{bmatrix} \frac{REW - D_{e_{(i-1)}})}{K_{emax}\, ET_{ref}}, \\ 1.0 \end{bmatrix} \quad (10)$$

F_t ranges from 0 to 1.

K_e is modified by the skin evaporation enhancement of Allen (2011) as:

$$K_e = \min \begin{bmatrix} [F_t + (1 - F_t)\, K_r]\, (K_{c\,max} - K_s\, K_{cb}), \\ f_{ew}\, K_{c\,max} \end{bmatrix} \quad (11)$$

The use of eqn. (10) and (11) simplifies the coding and calculation of E and makes the procedure continuous through the transition from stage 1 to stage 2 drying.

1.2 Hydrus-1D Model

Hydrus-1D is a numerical model that solves a modified Richard's equation using a finite element method for both saturated and unsaturated water flow in one dimension in a partially saturated rigid porous media. The Modified Richards' assumes that the air phase is not significant in liquid flow and that water flow due to thermal gradients can be neglected (Šimůnek, J., 2008). Equation 12 describes the Richards' equation for partially rigid porous media.

$$\frac{\partial \theta}{\partial t} = \frac{\partial}{\partial x}\left[K(h)\left(\frac{\partial h}{\partial x} + Cos\gamma\right)\right] - S \quad (12)$$

where θ is the volumetric water content, t is time, h is water pressure head (soil water head), x is the spatial coordinate (positive upward) i.e. x = L at soil surface and x = 0 at the bottom of the soil profile, S is a sink (root extraction) term, γ is the angle between the flow direction and the vertical axis (i.e., $\gamma = 0^0$ for vertical flow, 90^0 for horizontal flow), and K(h) is the unsaturated hydraulic conductivity function (Šimůnek, J., 2008).

The van Genuchten equation is a commonly used parametric model for relating volumetric water content (θ_v) to the matric potential (ψ_m). A statistical pore-size distribution model of Mualem [1976] was used to develop the van Genuchten [1980] equation. The van Genuchten equation is shown in eqn. (13).

$$\theta_h = \theta_r + \left[\frac{\theta_s - \theta_r}{1 + (|\alpha h|)^n}\right]^m \qquad h < 0 \tag{13}$$

$$\theta_h = \theta_s \qquad h \geq 0 \tag{14}$$

$$k(h) = K_s S_e^l \left[1 - (1 - S_e^{1/m})^m\right]^2 \qquad h < 0 \tag{15}$$

$$m = 1 - {}^1\!/_n \qquad n > 1 \tag{16}$$

where θ_r and θ_s are the residual and saturated water contents, respectively, h is the pressure head at the soil surface and α, n and m are parameters directly dependent on the shape of the water retention curve θ (ψ) curve for a specific soil type and condition, S_e is effective saturation, l is a pore-connectivity parameter, and m is the parameter for the soil water retention function.

1.2.1 Initial and Boundary Conditions of Hydrus-1D

Hydrus-1D (Šimůnek, 2008) uses an initial boundary condition for the solution of Richards's equation:

$$h(x, t) = h_i(x) \quad \text{at } t = t_0 \tag{17}$$

where h_i is initial water pressure head at x at the beginning of the simulation (t_0). The actual evaporative flux is computed by Richards's equation using system dependent boundary

condition. Actual evaporative flux is assumed equal to the potential evaporative flux if the pressure head is greater than some minimum pressure at the soil surface (hCritA) that is defined from equilibrium conditions between soil water and atmospheric vapor. Neumann boundary condition is applied to compute surface pressure at this condition. This limits the absolute value of the flux by satisfying the following two conditions (Šimůnek, J., 2008):

$$\left|-\mathrm{K(h)}\left(\frac{\partial \mathrm{h}}{\partial \mathrm{x}}+1\right)\right| \leq \mathrm{E_{max}} \qquad \text{at } \mathrm{z}=\mathrm{L} \tag{18}$$

$$\mathrm{h_A} \leq \mathrm{h} \leq \mathrm{h_S} \qquad \text{at } \mathrm{z}=\mathrm{L} \tag{19}$$

where E_{max} is the maximum potential rate of infiltration or evaporation under the current atmospheric conditions (E_{max} = E_1 from eqn. (1)) and h_A and h_S are the minimum and maximum pressure heads allowed under the prevailing soil conditions, L is the z-coordinate (depth of the soil profile) of the soil surface above a certain reference plane. The minimum pressure head (h_A) can be calculated from the relative humidity (H_r). Generally, the maximum value of the head allowed (h_s) is set at zero.

$$\mathrm{H_r} = \exp\left(-\frac{\mathrm{h_A Mg}}{\mathrm{RT}}\right) \tag{20}$$

$$\mathrm{h_A} = -\frac{\mathrm{RT}}{\mathrm{M\,g}}\ln(\mathrm{H_r}) \tag{21}$$

where M is the molecular weight of water (M = 0.018015 kg mol^{-1}), g is the gravitational acceleration (9.807 m s^{-2}), and R is the gas constant (R = (=8.314 J $mol^{-1}K^{-1}$). If h_s is positive during rainfall, the model creates a layer of water ponded on the surface. Excess water on the surface is immediately removed, which is one of the assumptions in the Hydrus-1D model.

In Hydrus-1D model, one of the system independent boundary must be specified at the soil

surface (x=L) or at the bottom of the profile (x=0) (Šimůnek, 2008).

$$h(x,t) = h_0(t) \quad \text{at } x = 0 \text{ or } x = L \tag{22}$$

$$-K\left(\frac{\partial h}{\partial x} + \cos\alpha\right) = q_0(t) \quad \text{at } x = 0 \text{ or } x = L \tag{23}$$

$$\left(\frac{\partial h}{\partial x} = 0\right) \text{ at } x = 0 \tag{24}$$

where h_0 is the surface boundary condition for the pressure head (L) and q_0 is water flux boundary condition at the bottom of the soil profile (L/T).

2.0 Materials and Methods

Comparisons between the original and enhanced FAO-56 evaporation models and the Hydrus-1D is done in two parts. Section 1 compares model estimates against evaporation measured by weighing lysimeter for a silt loam soil in southern Idaho. Section 2 compares the models and conducts a sensitivity analysis for theoretical soil types. Daily and hourly data sets were used to run the Hydrus-1D and FAO-56 models to evaluate the impact of timestep length on evaporation estimates.

2.1 Hydrus-1D and FAO-56 Model Setup

Soil hydraulic parameters recommended by the Hydrus-1D manual for its generalized silt loam, silt and sandy clay soils (Šimůnek, J., 2008) were used in the simulations. As summarized in Table 3.1, a 3 m soil depth was used for simulations with Hydrus-1D to insure that the upper soil profile was not impacted by the lower boundary condition. The 3 m profile was divided into 1001 vertical nodes representing 3 mm layers, to reduce numerical linearization error. The single porosity van Genuchten Mualem model without hysteresis was used for simulation with a single soil material. The atmospheric boundary layer with surface layer option was used as an upper boundary condition which permits water to build up on the

surface. A -150 m minimum pressure head was permitted at the soil surface. The lower boundary condition was chosen as a free drainage condition. Transpiration was assumed to be zero as all simulations were conducted for a bare soil condition. The computed reference ET_o representing a grass reference was used to approximate a potential evaporation rate in the Hydrus-1D model, using K_{emax} = 1.2 in Section 1 of the study. In section 2, a reference ET_r representing the tall reference crop of ASCE-EWRI (2005) was utilized, using K_{emax} = 1 as recommended by Allen (2011).

Tables 3.1 and 3.2 summarize the soil hydraulic properties for the three soil types used in the Hydrus-1D model and parameters used in the FAO-56 for the silt loam soil. The FAO-56 model is recommended to be applied using a 0.1 to 0.15 m depth of surface soil water (Z_e) subjected to drying by evaporation (Allen et al., 1998, 2011) while the Hydrus-1D model simulates a soil water balance for a deeper depth and considers upward flow toward the surface. In this study, Z_e was taken as 0.1 m for the FAO-56 model.

Table 3.1. Standard soil hydraulic parameters for Hydrus-1D simulations

Soil Properties	Symbol	Units	Sandy Clay Loam	Silt Loam	Silt
Residual soil water content	θ_r	m^3/m^3	0.1	0.067	0.034
Saturated soil water content	θ_s	m^3/m^3	0.39	0.45	0.46
Parameter α in the soil water retention function [L^{-1}]	α	mm^{-1}	0.0059	0.002	0.0016
Parameter n in the soil water retention function	n		1.48	1.41	1.37
Saturated hydraulic conductivity, K_s [LT^{-1}]	K_s	mm/day	314.5	108	60
Tortuosity parameter in the conductivity function	Tr		0.5	0.5	0.5

(Source: Hydrus-1D Šimůnek, J., 2008)

Table 3.2. Standard input data for a silt loam soil for the FAO-56 model

Soil Properties	Symbol	Units	Silt Loam
Field Capacity water content	θ_{fc}	m^3/m^3	0.36
Wilting Point water content	θ_{wp}	m^3/m^3	0.22
Depth of Surface Soil Layer subjected to Drying by Evaporation	Ze	m	0.1
Total Evaporable Water (calculated)	TEW	mm	25
Readily Evaporable Water	REW	mm	8

(Source: FAO-56, Allen et. al, 1998.)

3.0 Results and Discussions

3.1 Comparison of FAO-56 Original, FAO-56 Enhanced, and Hydrus-1D Models to Lysimeter

This section involved the comparison of the FAO-56 models and the Hydrus-1D model using evaporation data measured by a weighing lysimeter under a bare soil condition. The lysimeter was managed by Dr. J.L. Wright of the USDA-ARS (ret.) and was located near Kimberly, Idaho (latitude 42.54^o, longitude -114.35^o, elevation 1195 m). Data for a bare soil surface condition were collected from August 1st to September 24th, 1977. The weighing lysimeter was 1.83 m on a side and 1.2 m deep and was filled with repacked Portneuf silt loam soil during its construction in 1968. Details on the lysimeter installation and management and soil characteristics are given in Wright (1968, 1981). Total precipitation (precip.) plus irrigation (Irri.) during the observation period was 241 mm and total reference evapotranspiration was 239 mm. A daily evaporation coefficient (K_e) was calculated by dividing actual evaporation (E) over daily time periods by the associated reference evapotranspiration (ET_o). K_{emax} in the FAO-56 models was set to 1.2 for stage 1 evaporation estimation to be congruent with the use of the grass ET_o following recommendations by Allen et al., (1998) and Allen (2011). Weather data were collected at the USDA-ARS research center near Kimberly over a grassed surface (Wright 1981). TEW and REW were

set at 25 mm and 8 mm respectively for the silt loam soil texture and Z_e was set at 0.1 m for the FAO-56 model. The parameters of the FAO-56 were held constant for the silt loam soil setting, as recommended values for REW and TEW fall in the range for the silt loam soil for wide variety of soils. $K_{e\ max}\ ET_o$ was used to represent the potential E in Hydrus to be consistent with the maximum value set for FAO-56 simulations.

Figure 3.2 shows K_e estimated from the original FAO-56, enhanced FAO-56 and the Hydrus-1D models compared against lysimeter measurements for daily timesteps where the Hydrus-1D model was applied for both silt loam and sandy clay loam soils to serve as a means of bracketing the specific Portneuf silt loam of the lysimeter. Two different h_{ini} s of -3 m and -10 m were also used to bracket the likely h_{ini} of the lysimeter at the beginning of the drying events. The sandy clay loam of Hydrus has a slightly larger soil water retention parameter α as compared to the silt loam soil while the saturated hydraulic conductivity is 50 % larger than that of silt loam. The Hydrus-1D manual recommended 0.1 m^3/m^3 residual soil water content for a sandy clay loam texture and 0.067 m^3/m^3 for silt loam soil.

Figure 3.2 shows that the Hydrus-1D runs simulated relatively large evaporation spikes (K_e reaching 1.2) following small precipitation events that were on the order of < 5 to 10 mm whereas the original FAO-56 slab model did not show a substantial increase in K_e for those same precipitation events. This observation is most obvious during the period of 09/14/1977 to 09/24/1977 with small precipitation events of less than 5 mm. In contrast, the FAO-56 model enhanced with skin evaporation produced substantially increased estimates for K_e following the small wetting events, with behavior similar to K_e from Hydrus-1D. On the 09/16/1977 date having a light precipitation events of only a few mm, the lysimeter observed K_e = 0.24 while the original FAO-56 estimated K_e = 0.05, and the enhanced FAO-

56 model and Hydrus-1D, for all soil types, estimated 1.2. This occurred because of timing assumptions made for the daily precipitation additions.

On 08/26/1977, K_e based on lysimeter measurements was about 1.7, which is uncharacteristically high. The cause of that value, which substantially exceeds the value imposed in the models for $K_{e\ max}$, is uncertain. It was likely caused by a combination of random lysimeter error, an increase in evaporation on the first day of drying due to the presence of additional sensible heat energy available from the hot soil slab for evaporation and potentially by an underestimation of the reference ET for that day. The values for K_e from Hydrus-1D and the enhanced FAO-56 were at the upper limit of 1.2.

K_e from the Hydrus silt loam run with h_{ini} of -3 m tended to K_e during drying events. When h_{ini} was lowered to -10 m for the silt loam soil, K_e decreased during drying event but was still slightly larger than lysimeter measurements and slightly above estimates by the enhanced FAO-56 model (fig. 3.2 and 3.3). Hydrus runs for the sandy clay loam soil with h_{ini} of -3 m followed lysimeter measurements during drying events relatively closely, with slight underestimation at times. K_e computed from Hydrus-1D for the two silt loam simulations ran greater than that produced by the original FAO-56 slab model over most of the simulation period and K_e computed for the sandy clay loam simulation was lower than that by the original FAO-56 model.

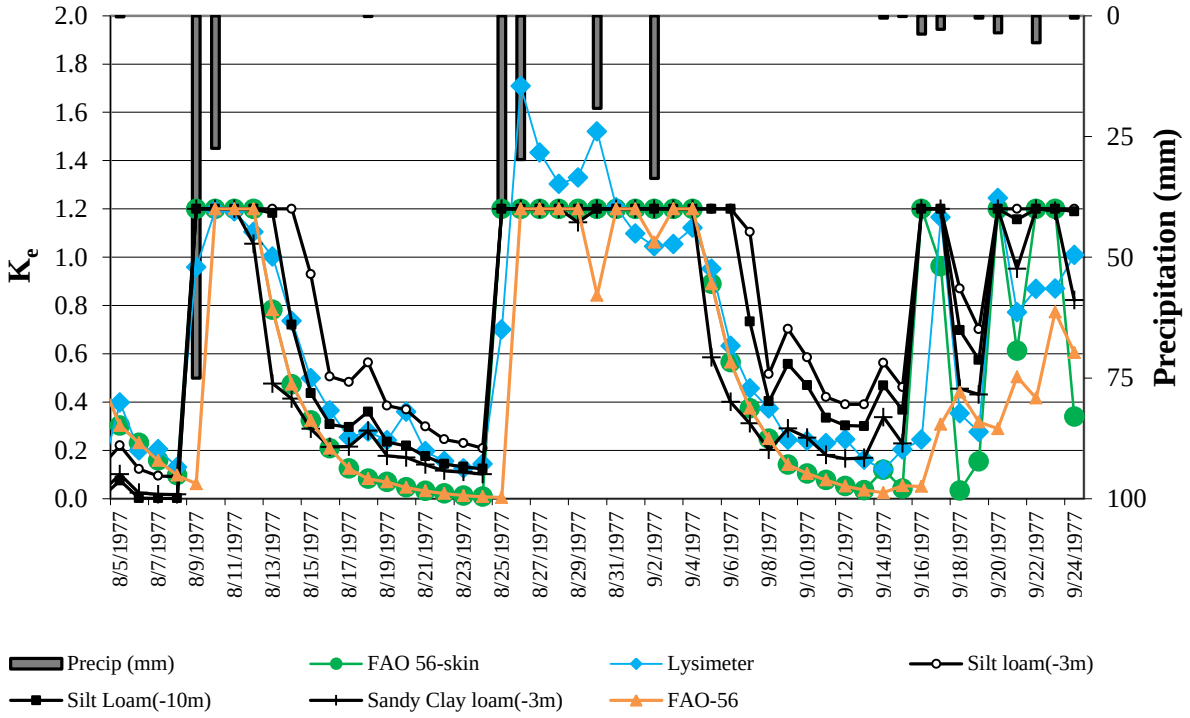

Fig. 3.2. Daily average K_{er} based on the alfalfa reference from (a) the original FAO-56 model and (b) the enhanced (skin evaporation) FAO-56 and from the Hydrus-1D for silt loam soil and sandy clay loam (h_{ini} = -3 m and -10 m respectively) over a one-year period at Kimberly, Idaho with daily calculation timesteps

Figure 3.3 shows the data of fig. 3.2 plotted in terms of daily average evaporation rate where Hydrus was operated using an h_{ini} = -3 m. As with the K_e comparisons, all models matched relatively closely to weighing lysimeter data, although the FAO method tended to reduce more quickly to lower evaporation values late in drying periods as compared to the lysimeter. This effect could be corrected by using a larger value for TEW, for example, 30 mm rather than 25 mm, as was shown by Allen (2011). Evaporation estimation improved with the skin enhancement where the original FAO-56 model estimated smaller values for E following light wetting events due to assumed mixing of the evaporation layer. The skin enhancement, with the more shallow 'reservoir' at the surface, made the small water additions immediately available for evaporation at higher rates. The Hydrus-1D simulations for the silt

loam soil slightly over-predicted evaporation during drying events as with the K_e calculations. Simulations for the sandy clay loam with its higher saturated hydraulic conductivity (314 mm/day) caused Hydrus-1D to estimate less evaporation in drying period compared to the silt loam soil. It is because soil with higher saturated hydraulic conductivity tends to have faster infiltration at drying period.

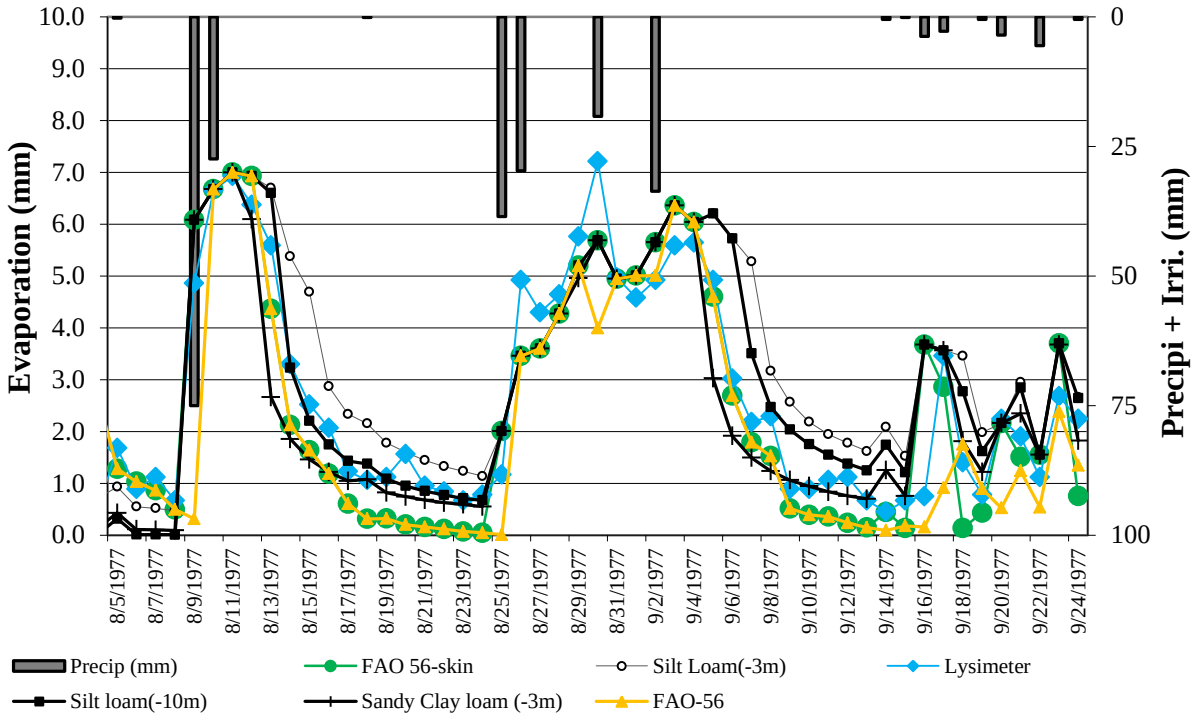

Fig. 3.3. Daily average evaporation from (a) the original FAO-56 model and (b) the enhanced (skin-evaporation) FAO-56 model and from the Hydrus-1D for silt loam soil and sandy clay loam (h_{ini} = -3 m and -10 m respectively) over a one-year period at Kimberly, Idaho with daily input data

Figure 3.4 shows the results of the previous simulations expressed as a scatter plot of daily evaporation between the FAO-56 model vs. the lysimeter data before and after application of skin evaporation enhancement. The R^2 was 0.83 before the enhancement while it increased to 0.88 after enhancement. The root mean square error decreased from 1.1 mm/day to 0.85 mm/day. A majority of evaporation points fell below the 1:1 line with the

original FAO-56 model, whereas, after enhancement, these points approached the 1:1 line, with the increased R^2.

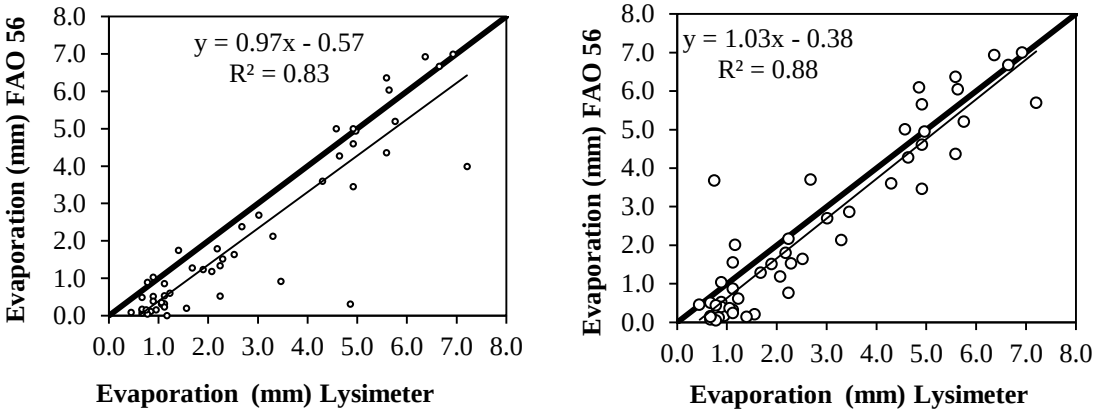

a) b)

Fig. 3.4. Scatter plot of daily evaporation from (a) the original FAO-56 model and (b) enhanced (skin-evaporation) FAO-56 model compared against lysimeter measurements for a bare silt loam soil near Kimberly, Idaho with daily data during August and September 1977

Figure 3.5 shows a scatter plot of daily evaporation from Hydrus-1D model vs. the lysimeter data for silt loam and sandy clay loam soils. The R^2 was 0.78 and 0.81 for silt loam and sandy clay loam soil respectively using -3 m h_{ini} at all nodes. The RMSE was 1.1 mm/day and 0.93 mm/day for the silt loam and sandy clay loam. The scatterplot shows the slight overestimation of evaporation from Hydrus-1D for the silt loam soil and conversely the underestimation for the sandy loam soil. Hydrus-1D simulations for the silt loam tended to estimate higher than the lysimeter during dry down periods as previously noted. Some of the overestimation may be due to using a relatively 'wet' h_{ini} for the entire soil profile which enabled an extended period of upward flux of water to be simulated during the surface drying.

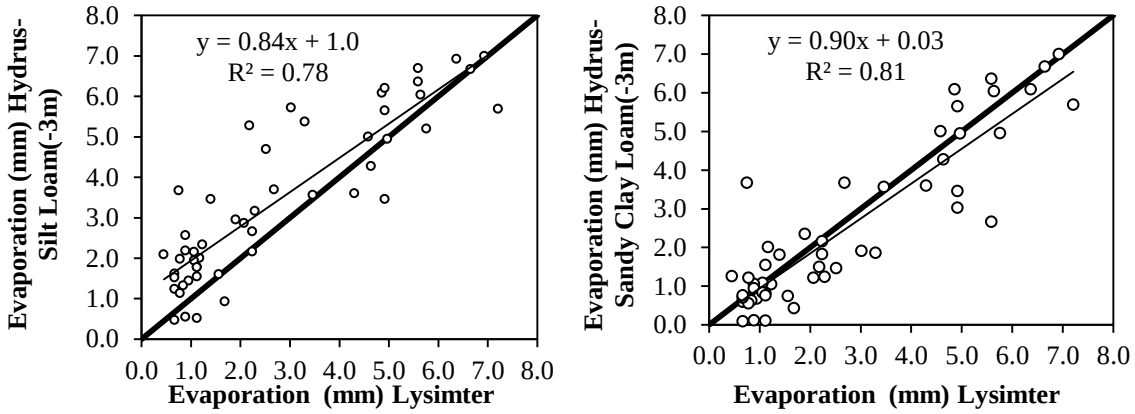

a) b)

Fig. 3.5. Scatter plot of daily evaporation from Hydrus-1D for (a) silt loam soil (b) sandy clay loam soil for h_{ini} = -3 m vs. lysimeter measurements near Kimberly, Idaho with daily input data during August

Table 3.3 summarizes statistics for the comparison of original FAO-56; enhanced FAO-56 and Hydrus-1D models vs. Lysimeter, along with cumulative evaporation rate. The lowest cumulative evaporation estimation came from the original FAO-56 model (106 mm) while the highest value came from Hydrus-1D for the silt loam soil (173 mm) with the initial pressure head of -3 m. Cumulative evaporation from the enhanced FAO-56 model was about 123 mm, and the lysimeter measured 139 mm. Hydrus-1D for sandy clay loam estimated about 127 mm.

Table 3.3. Summary of comparisons between the FAO-56 models, Hydrus-1D and lysimeter for daily precipitation and reference evaporation inputs for the Kimberly, Idaho data

FAO-56 vs. Lysimeter							
Model	**Parameters**	**Param. Values**	**Cumulative ET**	**Slope**	**Intercept**	**R^2**	**RMSE**
			mm				**mm/day**
Original FAO-56	REW	8 mm	106	0.97	-0.57	0.83	1.1
Enhanced FAO-56	TEW	25 mm	123	1.03	-0.38	0.88	0.85
Lysimeter			139				
Hydrus-1D vs. Lysimeter							
Model	**Parameters**	**Param. Values**	**Cumulative ET, mm**	**Slope**	**Intercept**	**R^2**	**RMSE**
Hydrus-Silt Loam(-3 m)	Initial Pressure head	-3 m	173	0.84	1.09	0.78	1.18
Hydrus-Sandy Clay Loam(-3 m)		-3 m	127	0.90	0.03	0.81	0.93

3.2 Comparison of Results between FAO-56 and Hydrus-1D Models with Daily Data for Theoretical Soils

In the previous section, Hydrus-1D simulations for the silt loam soil slightly over predicted ET during drying events and slightly under predicted for the sandy clay loam when compared to lysimeter measurements. In this section, simulations are described where both FAO-56 and the Hydrus-1D models are applied using specific soil parameters for three common soils in Hydrus-1D model runs and for a silt loam soil for FAO-56 model runs. The most common soil type in southern Idaho is silt loam (Westermann and Tindall, 1995, City of American Falls, 2009). The intent of this exercise was to evaluate the sensitivity of E from Hydrus-1D to soil texture and behavior of the FAO model over an extended period of four seasons, as well as impact of the skin enhancement. The one-year period included a range of evaporative demands and wetting sequences. The product K_{emax} ET_r was used to represent an upper evaporation limit for both the FAO-56 and the Hydrus-1D models. Reference evaporation was calculated using the ASCE Penman-Monteith equation for the tall (alfalfa)

reference for both the FAO-56 and the Hydrus-1D model runs. Calculations were made using the RefET model (Allen, 2010) using daily and hourly weather data. Weather and precipitation data were acquired from the Twin Falls AgriMet weather station (lat. = 42.54611 N, long. = 114.34527 W, elev. = 1195 m) for year 2002. The annual cumulative reference evapotranspiration was 1560 mm and 1470 mm for daily and hourly calculation time steps respectively, with annual precipitation of 154 mm.

Model run scenarios were conducted using the Hydrus-1D model for three h_{ini} profiles. Simulations were made with an h_{ini} of -3.0 m representing approximate field capacity, -10.0 m (-1.0 atmosphere) and -0.5 m (representing near saturation). The FAO-56 recommends a REW value for silt loam soil of 8 -11 mm, with 8 mm used in these simulations, and TEW as 25 mm when Z_e = 0.1m. The computed evaporation coefficient (K_{er}) was based on the alfalfa reference, with a K_{emax} = 1.0 representing a maximum evaporation rate. Hourly simulation results from the Hydrus-1D model were summed to daily values prior to making comparisons with FAO-based simulations and prior to computing K_{er} by dividing E by ET_r to avoid numerical division errors while computing K_{er} caused by small or zero values for evaporation and reference ET during night time.

3.2.1 FAO-56 vs. Hydrus-1D model with Initial Pressure Head of -3 m

This scenario compared simulated K_e from the original and enhanced FAO-56 models with simulations by the Hydrus-1D model for silt loam and sandy clay loam soil for h_{ini} of -3 m, representing the field capacity water content. Results presented in fig. 3.6a show the daily K_e time series during the simulation year. K_e is expressed as K_{er} in the figures, representing the reference ET_r basis. As previously demonstrated, the original FAO-56 model with the mixed evaporation slab did not produce the characteristic short-duration evaporation spikes

associated with small precipitation events that were simulated by the enhanced FAO-56 and Hydrus-1D model (fig. 3.6a ad 3.6b). For example, on 05/21/2002, following a 2.5 mm precipitation, the K_{er} value computed by the original FAO-56 remained near zero, while the Hydrus-1D model for a silt loam soil texture estimated K_e =1.0 which is the upper limit specified for the model. With the skin evaporation enhancement, the FAO-56 model also estimated K_{er} = 1.0 (fig. 3.6b). Likewise, on 09/17/2202, the original FAO-56 model estimated K_{er} = 0.03 while the Hydrus-1D model and enhanced FAO-56 model both estimated K_{er} = 0.8. In nearly all cases, the FAO-56 model with skin-evaporation enhancement and Hydrus-1D model predicted similar K_{er} following precipitation events, and with similar decay of K_{er} with time of drying. Residual K_{er} during long drying periods during late November and December was estimated higher with the Hydrus-1D model when potential evaporation rates were low and upward flux from the wet soil profile was simulated to support a K_{er} averaging about 0.15. As in the lysimeter comparison, the K_{er} from the Hydrus-1D model for sandy clay loam soil was smaller during the winter months compared to the silt loam soil texture (fig. 3.6b) while matching simulations for the silt loam texture during the rest of the year (fig. 3.6b).

The FAO-56 model has no provision for simulating upward flux from below the evaporation slab. Instead, the average impact of upward flux is accounted for by specifying a larger depth for Z_e, based on field observation of total evaporation between wetting events. Comparisons with Hydrus-1D results for an initial pressure condition near field capacity suggests that an upward flux provision may not be necessary for estimating evaporation from the soil surface, provided an appropriate value for Z_e (for example, Z_e = 0.1 – 0.15 m) is used in the FAO-56 model to represent the effective depth of the evaporative layer.

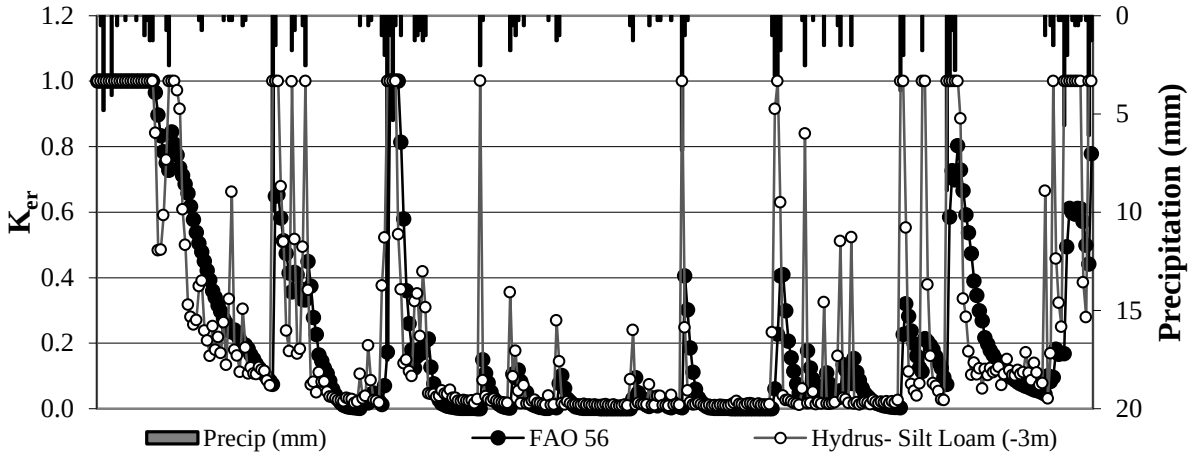

a)

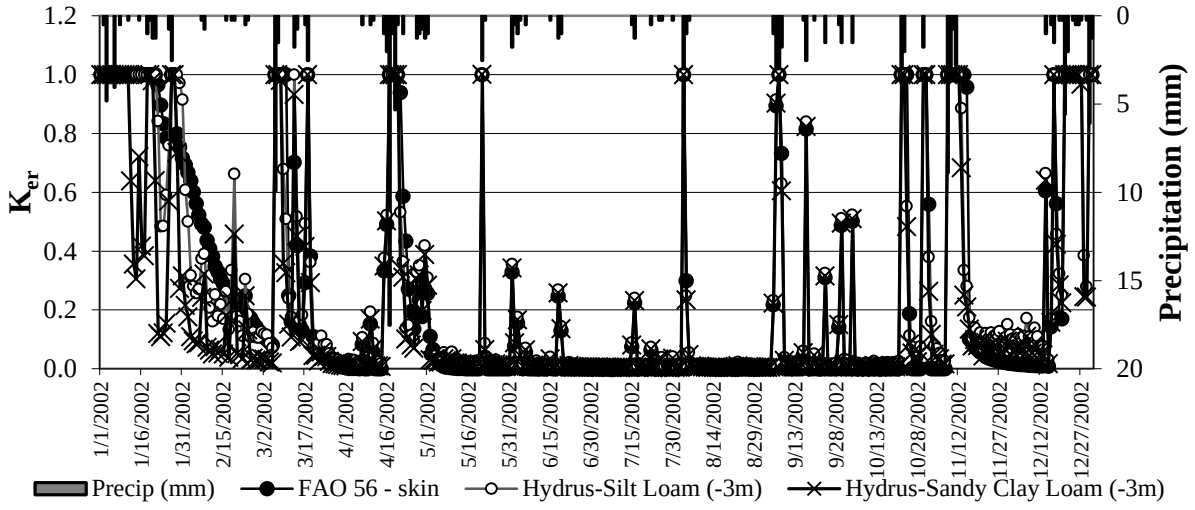

b)

Fig. 3.6. Daily average K_{er} based on the alfalfa reference from (a) the original FAO-56 model and (b) the enhanced (skin evaporation) FAO-56 and from the Hydrus-1D for silt loam and sandy clay loam textures using h_{ini} = -3 m over a one-year period at Kimberly, Idaho with daily precipitation and weather data inputs

Figure 3.7 shows daily evaporation rate from the models associated with the K_{er} shown in fig. 3.6, with h_{ini} = -3.0 m in the Hydrus-1D run. As with the K_{er} comparison, the original FAO-56 (fig. 3.7a) did not produce the same increase in evaporation rate following relatively small precipitation events (5 to 10 mm) as did the enhanced FAO-56 and Hydrus-1D models (fig. 3.7b). On a number of days following precipitation events, estimated E was

nearly identical between the Hydrus-1D and enhanced FAO-56 model due to the use of the same value for K_{emax} and as an upper limit on potential E (fig. 3.7b).

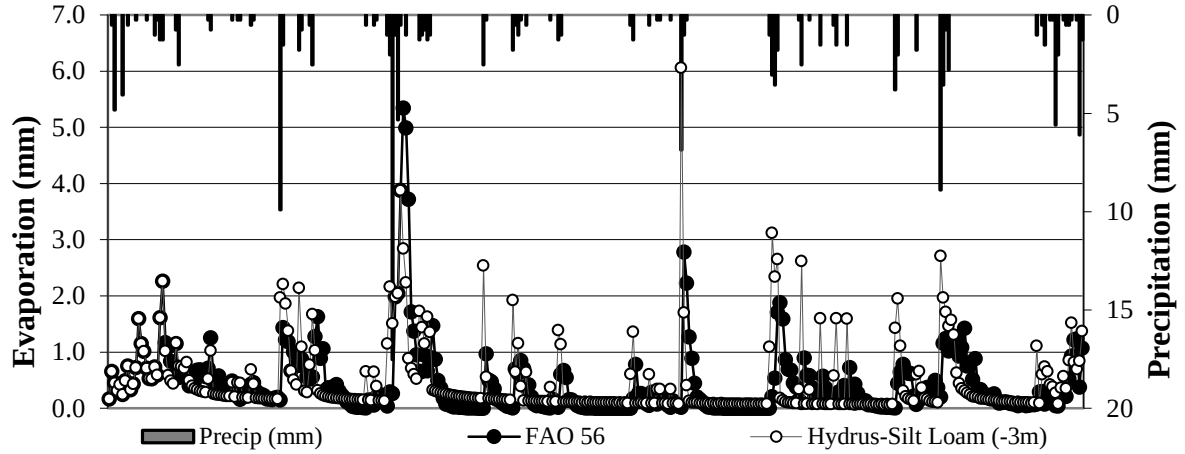

a)

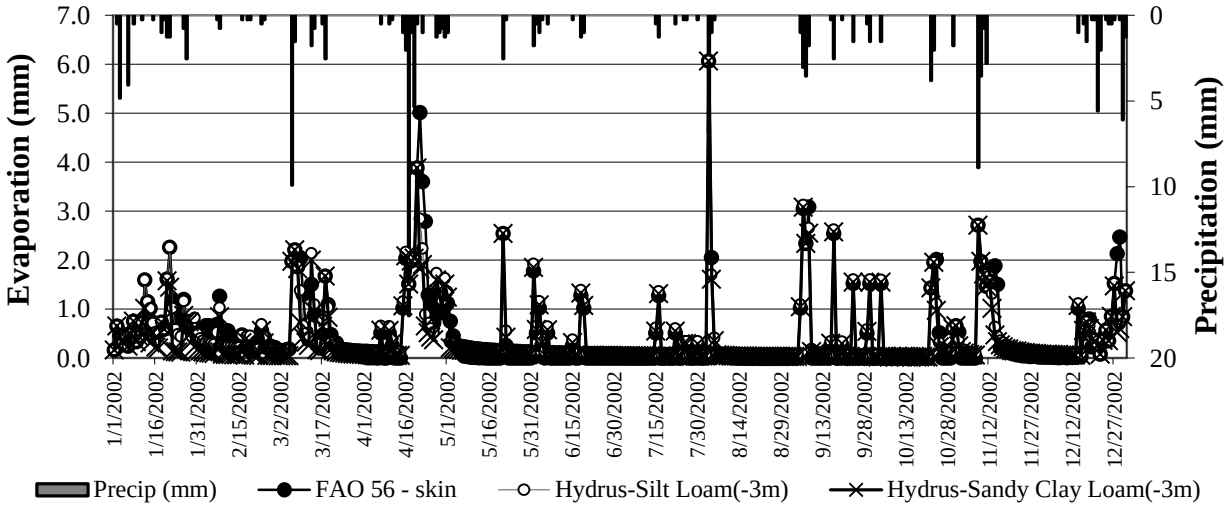

b)

Fig. 3.7. Daily evaporation based on the alfalfa reference from (a) the original FAO-56 model and (b) the enhanced (skin evaporation) FAO-56 and from the Hydrus-1D for silt loam and sandy clay loam textures using h_{ini} = -3 m over a one-year period at Kimberly, Idaho with daily precipitation and weather data inputs

Cumulative evaporation matched closely among the models for the silt loam soil throughout the year, where cumulative evaporation over the year totaled 166 mm and 175 mm for the enhanced FAO-56 and the Hydrus-1D models respectively (fig. 3.8). The

cumulative evaporation from Hydrus-1D for sandy clay loam was smaller i.e. 142 mm. The enhanced FAO-56 and Hydrus-1D model for the silt loam texture exceeded the 154 mm of recorded precipitation due to evaporation of assumed initial water stored in the soil profilem.

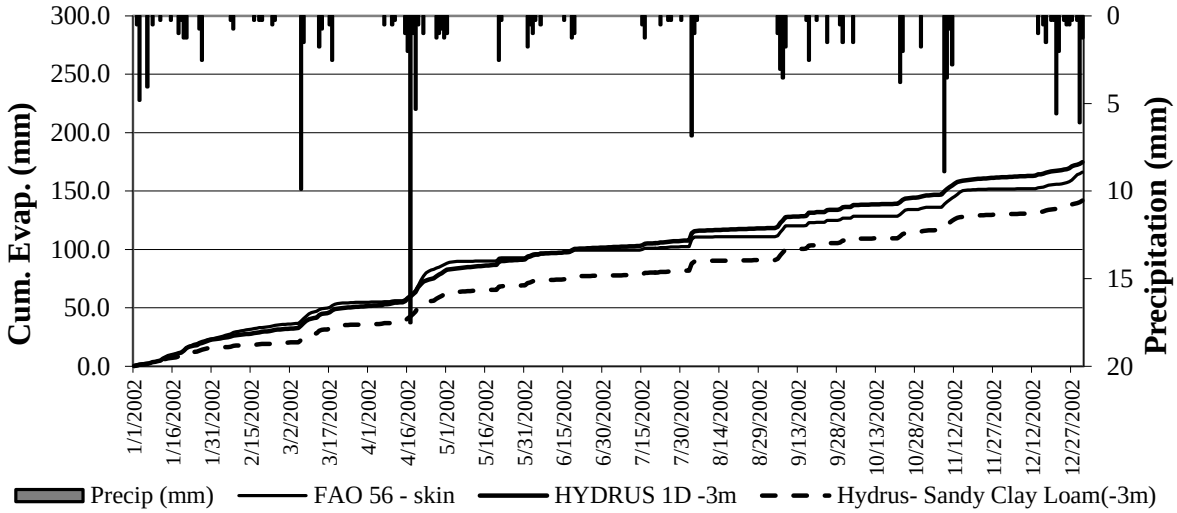

Fig. 3.8. Commutative evaporation based on the alfalfa reference from the FAO-56 model with the skin evaporation enhancement and from the Hydrus-1D for silt loam and sandy clay loam soil (h_{ini} = - 3 m) over a one-year period at Kimberly, Idaho with daily calculation timesteps

Figures 3.9a and 3.9b show scatter plots of daily averaged evaporation amounts estimated by the original FAO-56 (fig. 3.9a) and by the enhanced FAO-56 model (fig. 3.9b) vs. daily averaged evaporation amounts from the Hydrus-1D model with h_{ini} = -3 m for the silt loam texture. There was significant improvement in the agreement between E estimated from the FAO-56 with the skin evaporation enhancement and Hydrus-1D (fig. 3.9b) where the coefficient of determination (R^2) increased from 22% to 88%. With the enhancement, some of the evaporation estimates fell above the 1:1 line, but with a majority of estimates were located near the 1:1 line. The RMSE between the original FAO-56 and the Hydrus-1D for the silt loam texture with h_{ini} = -3 m was about 0.67 mm/day, whereas after the enhancement, the RMSE decreased by more than 50% to 0.27 mm/day. There are different

parameters in the Hydrus-1D model as well as the FAO-56 that can create variability in the evaporation computation. However, standard values were used with both models for this exercise.

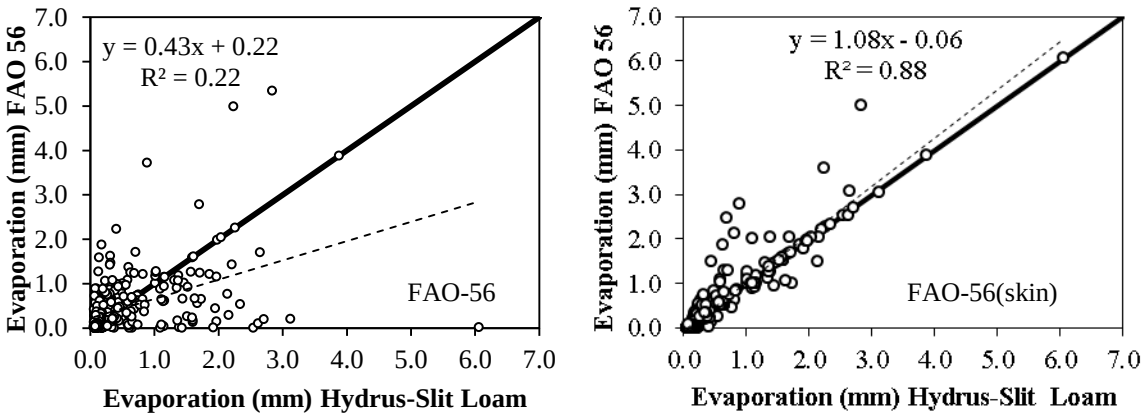

a) b)

Fig. 3.9. Scatter plot of daily evaporation from (a) the original FAO-56 model and (b) enhanced (skin-evaporation) FAO-56 model vs. daily evaporation estimated by the Hydrus-1D using an h_{ini} = -3 m for a bare silt loam soil over a one-year period at Kimberly, Idaho with a daily precipitation and weather data inputs

3.2.2 FAO-56 vs. Hydrus-1D Model with Initial Pressure Head of -0.5 m and -10 m

In this scenario, simulations were conducted for initial pressure heads of -0.5 m (near saturation) and -10 m (1 atmosphere). Because of the relatively wet soil water profile assumed by the h_{ini} of -0.5 m for all profile nodes, the Hydrus-1D model estimated slightly larger values for evaporation for the silt loam texture throughout the simulation period as compared to both the original and enhanced FAO-56 models. The higher estimation by Hydrus-1D was due to upward flow from the wet soil profile and higher initial water storage coupled with relatively higher hydraulic conductivity. The total cumulative evaporation from the Hydrus-1D model decreased when h_{ini} was reduced to -3.0 m (Table 3.4).

The second Hydrus-1D run using an h_{ini} of -10 m at all nodes explored the influence of a relatively dry initial soil profile on simulated evaporation in the dry Idaho climate. In

this scenario, Hydrus-1D produced smaller K_{er} during the initial months (January to February) as compared to the FAO-56 model and as compared to previous Hydrus-1D runs using -0.5 m and -3 m. The K_{er} from Hydrus-1D model decayed more quickly following wetting events due to the dry subsoil and less water storage. The results matched closely with those from the FAO-56 and with Hydrus-1D model simulations for all h_{ini} except for the winter months. The results of simulations by Hydrus-1D model for h_{ini} = -10 m are summarized in table 3.4.

Table 3.4. Summary of comparisons between the FAO-56 models and Hydrus-1D model for daily precipitation and weather data from Kimberly Idaho for year 2002 and a silt loam soil texture where regressions are expressed against Hydrus-1D for three initial pressure heads

Model	Parameters	Values	Cumulative ET	Slope	Intercept	R^2	RMSD
			mm				mm/day
Original FAO-56	REW	8 mm	158	0.43	0.22	0.22	0.67
Enhanced FAO-56	TEW	25 mm	166	1.08	-0.06	0.88	0.27
Hydrus-Silt Loam Soil	Initial Pressure head	-3 m	175				
Original FAO-56	REW	8 mm	158	0.45	0.16	0.26	0.68
Enhanced FAO-56	TEW	25 mm	166	1.05	-0.17	0.88	0.30
Hydrus-Silt Loam	Initial Pressure head	-0.5 m	220				
Enhanced FAO-56	REW	8 mm	166	1.06	0.03	0.83	0.33
	TEW	25 mm					
Hydrus- Silt Loam	Initial Pressure head	-10 m	146				

Annual measured precipitation = 154 mm

3.3 Comparison of Results between FAO-56 and Hydrus-1D Model with Hourly Timesteps

A second set of analyses was conducted using hourly precipitation and weather data and hourly calculation timesteps with the FAO-56 models. The Hydrus-1D utilizes its own automated determination of calculation timestep depending on the rate of change of state variables. The same generalized silt loam soil texture was utilized for the models, with a

TEW of 25 mm and REW of 8 mm used in FAO-56 simulations. The hourly estimates for E from both the Hydrus-1D model and the FAO-56 model were summed to daily values prior to making comparisons to avoid calculating large ratios for K_{er} during periods of near zero ET_r during nighttime and early morning periods, the Hydrus-1D model was run using h_{ini} = -0.5 m and -3.0 m.

The hourly results followed similar trends observed for the daily data and calculation timesteps for both initial pressure heads. For the h_{ini} -3.0 m condition, cumulative annual evaporation from the enhanced FAO-56 model and the Hydrus-1D models totaled 162 mm and 169 mm respectively over the annual period. The R^2 between the original and enhanced FAO-56 model and Hydrus-1D models was 0.54 and 0.83 respectively (Table 3.5). Even though the R^2 increased significantly, the RMSD did not change noticeably following the skin evaporation enhancement for h_{ini} of -3.0 m (Table 3.5), where the RMSD between the original FAO-56 with hourly calculation timesteps and the Hydrus-1D was about 0.38 mm/day and 0.378 mm/day after the enhancement. For a h_{ini} of -0.5 m in Hydrus-1D, the FAO-56 model after enhancement produced cumulative evaporation of 162 mm, showing a slight increase compared to the original FAO-56 model (Table 3.5). The R^2 between the FAO-56 models and Hydrus-1D run prior to and following enhancement was 0.58 and 0.82 respectively. Total cumulative annual evaporation estimated by Hydrus-1D increased by about 40 mm when h_{ini} was increased from -3.0 to -0.5 m. The h_{ini} = -0.5 m represents a very wet condition near saturation.

Table 3.5. Summary of comparisons between the FAO-56 models and Hydrus-1D model for hourly precipitation and weather data and hourly calculation time steps for a silt loam soil texture at Kimberly, Idaho during year 2002

Model	Parameters	Values	Cumulative ET	Slope	Intercept	R^2	RMSD
			mm				mm/day
Original FAO-56	REW	8 mm	157	0.85	0.03	0.54	0.38
Enhanced FAO-56	TEW	25 mm	162	1.41	-0.206	0.83	0.378
Hydrus-Silt Loam	Initial Pressure head	-3 m	169				
Original FAO-56	REW	8 mm	157	0.83	-0.054	0.58	0.40
Enhanced FAO-56	TEW	25 mm	162	1.33	-0.33	0.82	0.39
Hydrus-Silt Loam	Initial Pressure head	-0.5 m	212				

Annual measured precipitation = 154 mm

3.4 Sensitivity Analyses on REW and Soil Type

3.4.1 Daily Calculation Timesteps

A sensitivity analysis was conducted to evaluate the influence of simulating different soil types in the Hydrus-1D model. As in section 3.1 with the lysimeter comparisons, Hydrus-1D simulations for a sandy clay loam soil with initial pressure head of -3 m had less evaporation compared to the silt loam soil. The Hydrus-1D model with h_{ini} = -3.0 m produced an R^2 = 0.89 and 0.81 for the silt and sandy clay loam soils respectively, when compared to the enhanced FAO-56 model. The RMSD value for the silt soil was about 0.26 mm/day between the enhanced FAO-56 model and the Hydrus-1D model with -3 m h_{ini}. For the sandy clay loam soil, RMSD increased to 0.34 mm/day for h_{ini} = -3.0 m showing increased departure between the two model types.

Sensitivity analyses were carried out on the enhanced FAO-56 model to assess the sensitivity to changes in the model parameter REW describing the depth of evaporation associated with stage 1 drying. REW is often estimated from observations but can be a somewhat subjective estimate. A second set of sensitivity analyses was conducted for the silt

loam soil by changing values for both REW and TEW in the enhanced FAO-56 model. When REW was decreased to 5 mm, the agreement with Hydrus-1D for -3.0 m h_{ini} was slightly improved (R^2 = 0.90). RMSD was also the lowest among the other daily simulations with a value of 0.23 mm/day. Cumulative evaporation from the enhanced FAO-56 model decreased by only 2 mm since the value for TEW remained unchanged, and the FAO-56 is constrained by a conservation water balance. Decreasing REW for the silt loam soil decreased the differences between the model and Hydrus-1D run and increased R^2. Some of the evaporation estimates that fell above 1:1 line earlier came closer to the 1:1 line with the smaller value for REW. When REW was increased to 11 mm, the R^2 value decreased slightly to 0.85 and the RMSD value increased to 0.32 mm/day.

Field capacity and wilting point soil water contents were changed to vary the values for TEW for the silt loam soil but there were no significant changes in results, primarily due to the relatively small depths of wetting events that tended to capture and hold most of the precipitation for all levels of TEW tested. In regions having relatively large depths of precipitation per wetting event, the sensitivity of estimated cumulative evaporation to TEW is expected to be much greater. R^2 values ranged from 0.8 to 0.9 and RMSD ranged from 0.23 mm/day to 0.34 mm/day between the enhanced FAO-56 model and the Hydrus-1D model over a wide range of the simulations with different soil types and ranges of REW and TEW. With daily calculation time steps, the cumulative ET from the enhanced FAO-56 model was 159 mm and R^2 was about 0.85 compared to Hydrus-1D when TEW was decreased about 25% (i.e. 18 mm) with REW set at 8 mm. The agreement between the models was slightly reduced and RMSD was increased to 0.32 mm/day. The R^2 and RMSD slightly improved for daily calculation timesteps with decreased REW.

Sensitivity was also explored for the impact of using smaller vertical nodes in the Hydrus-1D model, where a grid size of half millimeter was specified. Differences in results from runs employing the 3 mm node distance were very small. Table 3.6 summarizes the results of the sensitivity analyses.

Table 3.6. Summary of sensitivity analyses on impacts of soil texture in Hydrus-1D simulations with comparisons against the enhanced FAO-56 model using daily weather and precipitation inputs

Model	Parameters	Values	Cumulative ET	Slope	Intercept	R^2	RMSD
			mm				mm/day
Silt Soil							
Enhanced FAO-56	REW	8 mm	166	1.08	-0.08	0.89	0.26
	TEW	25 mm					
Hydrus-1D	Initial Pressure head	-3 m	182				
Sandy Clay loam Soil							
Enhanced FAO-56	REW	8 mm	166	1.057	0.044	0.81	0.34
	TEW	25 mm					
Hydrus-1D	Initial Pressure head	-3 m	142				
Silt Loam Soil							
Enhanced FAO-56	REW	5 mm	164	1.001	-0.029	0.90	0.23
	TEW	25 mm					
Hydrus-1D	Initial Pressure head	-3 m	175				
Enhanced FAO-56	REW	8 mm	159	1.119	-0.099	0.85	0.32
	TEW	18 mm					
Hydrus-1D	Initial Pressure head	-3 m	175				
Enhanced FAO-56	REW	11 mm	166	1.105	-0.073	0.85	0.32
	TEW	25 mm					
Hydrus-1D	Initial Pressure head	-3 m	175				

Annual measured precipitation = 154 mm

3.4.2 Hourly Calculation Timesteps

Sensitivity analyses were also carried out on REW in the enhanced FAO-56 model

for hourly precipitation data and calculation timesteps. The REW was lowered to a value of 3 mm, which represents a very quick drying surface and short duration of stage 1 drying (when K_{er} = 1). R^2 improved to 0.89 as compared to R^2 = 0.82 for REW = 8 mm when compared to the Hydrus-1D model with an h_{ini} of -0.5 m. Similarly, when compared to the Hydrus-1D run for an h_{ini} of -3.0 m, the R^2 increased from 0.83 to 0.90 when lowering REW to 3 mm. The RMSD decreased to the value of 0.26 mm/day and 0.22 mm/day for h_{ini} of -0.5 m and -3 m respectively. Decreasing REW seems to have a greater impact for hourly timestep calculation as compared to using daily timesteps due to finer resolution in simulating the duration of stage 1 drying and the particular shape of the drydown curve vs. time. For example, on the 4th of August, evaporation computed from the enhanced FAO-56 reduced from 6.6 mm/day when REW was 8 mm to 3.6 mm/day with REW of 3 mm/day. The evaporation estimated by Hydrus-1D was 2.8 mm/day for -0.5 m h_{ini} and 2.7 mm/day for -3.0 m h_{ini}. Table 3.7 summarizes the results of hourly timesteps data for the reduced REW.

Table 3.7. Summary of sensitivity analyses on reducing REW in the enhanced FAO-56 model for hourly simulations for a silt loam soil texture vs the Hydrus-1D model for weather data from Kimberly, ID during 2002

Model	Parameters	Values	Cumulative ET	Slope	Intercept	R2	RMSD
			mm				mm/day
FAO-56	REW	3 mm	161	-0.121	1.219	0.90	0.22
	TEW	25 mm					
Hydrus-Silt Loam	Initial Pressure head	-3.0 m	169				
FAO-56	REW	3 mm	161	-0.225	1.146	0.89	0.26
	TEW	25 mm					
Hydrus-Silt Loam	Initial Pressure head	-0.5 m	212				

Annual measured precipitation = 154 mm

Figure 3.10 shows a scatterplot of daily evaporation computed using daily timesteps and vs. using hourly timesteps data summed to daily values for enhanced FAO-56 model for

h_{ini} -3.0 m for silt loam soil. The results showed that daily timesteps evaporation generated small variations to hourly timesteps values with R^2 of 0.86 and RMSD of 0.28 mm/day.

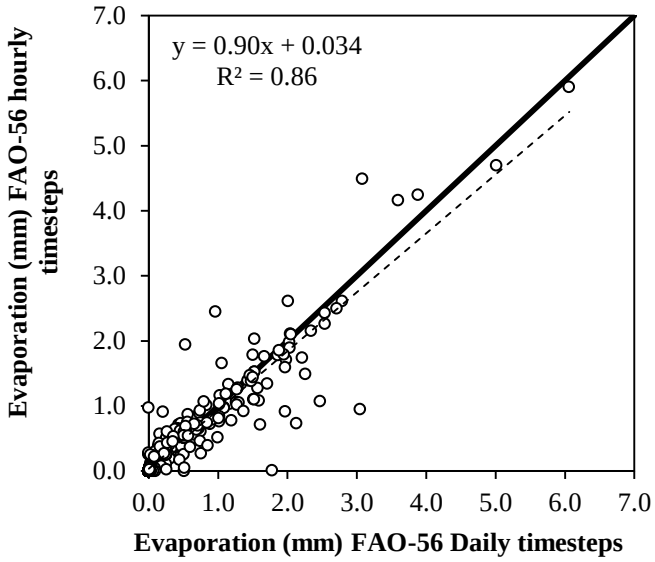

Fig. 3.10. Scatter plot of daily evaporation from the enhanced FAO-56 model with hourly calculation timesteps summed daily and daily calculation timesteps for h_{ini} = - 3 m for a bare silt loam soil over a one-year period at Kimberly, Idaho

4.0 Conclusions

The study illustrated the benefits of the skin layer evaporation enhancement of Allen (2011) incorporated into the FAO-56 model in simulating E during the hours or days immediately following shallow wetting events. The improved behavior was confirmed by comparison of model results to field lysimeter measurements for bare soil conditions and against the Hydrus-1D model. The simple FAO-56 model enhanced with skin evaporation layer was relatively successful in producing short-lived evaporation spikes associated with small precipitation events when compared to the more complex numerical solutions used in the Hydrus-1D model and with the lysimeter data. Sensitivity analyses indicated that overall accuracy of the evaporation coefficient K_{er} for smaller precipitation events in the FAO-56 model are somewhat sensitive to the values for TEW and REW terms. The coefficient of

agreement for K_{er} was slightly higher for daily timesteps as compared to hourly calculation time steps with the FAO-56 model. Otherwise, simulation results were similar in all applications, indicating that daily calculation timesteps are sufficient when using the skin evaporation enhancement that implicitly identifies the transition time between stage 1 and stage 2 drying. The evaporation of initial water stored in the soil profile and initial water potential h_{ini} of the soil played an important role in total cumulative E estimated by Hydrus-1D and the duration of drydown following wetting events. The simulation results showed that Hydrus-1D simulations to be relatively sensitive to saturated hydraulic conductivity. In general, the FAO-56 model with skin enhancement and implicit stage 1 – stage 2 transition estimation produces estimates of daily E that are similar to those of Hydrus-1D using daily or hourly calculation timesteps for the FAO-56 model. This is a useful finding and indicates that models incorporating the FAO-56 procedure will generally provide accurate accounting for E.

References

Allen R.G., 2011. Skin layer evaporation to account for small precipitation events-An enhancement to the FAO-56 evaporation model. Agricultural Water Management.

Allen, R. G., Pereira L. S., Raes, D., and Smith, M., 1998. Crop evapotranspiration: Guidelines for computing crop requirements." Irrigation and Drainage Paper 56, FAO, Rome, Italy.

Allen, R.G., Pereira, L.S., Smith, M., Raes, D. and Wright, J. L., 2005. FAO-56 dual crop coefficient method for estimating evaporation from soil and application extensions. J. Irrig. Drain Eng. ASCE 131 (1), 2–13.

Burt, C. M., Mutziger, A. J., Howes, D. J., and Solomon, K. H., 2002. Evaporation from irrigated agriculture land in California. A study funded by the CALFED and the California State University! Agricultural Research Initiative. Available on the web page (http:// www.itrc.orglreports!reportsindex.html). Irrigation Training and Research Center. California Polytechnic State Univ. San Luis Obispo, Calif

FAO-56 modeled evaporation from bare soil. J. Irrig. Drain. Engrg. ASCE 131 (1), 59–72.

Howell, T. A., Steiner, J. L., Schneider, A. D., and Evett, S. R., 1995. Evapotranspiration of irrigated winter wheat-Southern Plains. Trans. ASAE, 38(3), 745-759.Trans. ASAE, 38(3), 745~759.

http://websoilsurvey.nrcs.usda.gov/app/WebSoilSurvey.aspx) <accessed 2012>.

http://www.groundwatersoftware.com/v9_n5_hydrus.htm <accessed 2010>.

http://www.pc-rogress.com/en/Default.aspx?HYDRUS 1D-faq-01-10 <accessed 2010>.

Hunsaker, D. J., Pinter, P. J. and Cai, H., 2002. Alfalfa basal crop coefficients for FAO-56 procedures in the desert regions of the southwestern U.S.Transactions of the ASAE, 45 (6) (2002), pp. 1799–1815.

Mutziger, A. J., Burt, C. M., Howes, D. J. and Allen, R. G., 2005. Comparison of measured and FAO-56 Modeled Evaporation from Bare Soil.

Šimůnek, J., Šejna, M., Saito, H., M. Sakai, and van Genuchten, M. T., 2008. The HYDRUS-1D Software Package for Simulating the One-Dimensional Movement of Water, Heat, and Multiple Solutes in Variably-Saturated Media. Department of environmental sciences, University of California Riverside, Riverside, California.

Weeks B., and Wilson, G. W., 2006. Prediction of evaporation from soil slopes. Canadian Geotech J. 43: 815-829.

Wright, J. L., 1982.

Wright, J. L., 1991.

Appendix-A: Parameters and Variables in BATANS

Parameters and Variables

Fraction of vegetation cover is computed assuming a linear relationship between normalized difference vegetation index (NDVI) and fraction of vegetation cover using eqn. (1).

$$f_c = \frac{NDVI - NDVI_{min}}{NDVI_{max} - NDVI_{min}} \quad (1)$$

where f_c is fraction of vegetation cover, NDVI is normalized difference vegetation index, $NDVI_{max}$ is the maximum value of NDVI which is taken as 0.80 and $NDVI_{min}$ is the minimum value of NDVI which is 0.15.

Actual vapor pressure is computed from pressure and specific humidity using eqn. (2).

$$e_a = \frac{P\, q_a}{(0.378\, q_a + 0.622)} \quad (2)$$

where e_a is actual vapor pressure (kPa), P is pressure (kPa) and q_a is specific humidity (kg/kg).

Height of vegetation is computed according leaf area index suggested by Allen et al., 2010 (eqn. (3)).

$$h_c(m) = \begin{cases} 2.5 * \text{ LAI for forest} \\ 0.8 \text{ for sagebrush desert} \\ 0.15 * \text{ LAI Otherwise} \end{cases} \quad (3)$$

where h_c is height of vegetation (m) and LAI is leaf area index.

Zero plane displacement is computed from eqn. (4) (Choudhury and Monteith, 1988).

$$d = 1.1\, h_c \ln(1 + X^{\frac{1}{4}}) \quad (4)$$

where d is zero plane displacement (m) and X is parameter for calculating zero plane displacement.

X parameter of the zero plane displacement is calculated using eqn. (5).

$$X = c_d LAI \tag{5}$$

where c_d is mean drag coefficient for individual leaves which is used as a 0.2 (Shaw and Pereira, 1982; Choudhury and Monteith, 1988). Shuttleworth and Gurney, 1990 recommends the value of c_d as 0.07.

Attenuation coefficient is computed using eqn. (6) (Choudhury and Monteith, 1988).

$$n = \begin{cases} 2.5 \text{ if } h_c < 1m \\ 4.25 \text{ if } h_c > 10m \\ 2.31 + 0.194\ h_c \text{ Otherwise} \end{cases} \tag{6}$$

where n is attenuation coefficient.

Rooting depth which is approximately used as 1 or 2 m according to land use classes according to eqn. (7).

$$d_{root} = \begin{cases} 2.0 \text{ for land use classes } 41, 42, 43, 52 \text{ and } 90 \\ 1.0 \text{ otherwise} \end{cases} \tag{7}$$

where d_{root} is rooting depth (m).

Soil Portion Surface Energy Balance

Outgoing long wave radiation of soil portion is computed using eqn. (8).

$$R_{L\_s\uparrow} = {T_s}^4\ \sigma\ \varepsilon_{o\_s} \tag{8}$$

where $R_{L\_s\uparrow}$ is outgoing longwave radiation of soil portion (W/m^2), T_s is surface temperature of soil portion (K), ε_{o_s} is broad band emissivity of soil portion, and σ is Stefan-Boltzmann constant ($W/m^2/K^4$).

Surface temperature of soil portion is computed inverting sensible heat flux equation of soil portion as an initial guess (eqn. (9)).

$$T_s = \frac{H_s\ (r_{ah} + r_{as})}{\rho_a\ c_p} + T_a \tag{9}$$

where H_s is sensible heat flux of soil portion (W/m^2), r_{ah} is aerodynamic resistance from vegetation height to blending height (s/m), r_{as} is aerodynamic resistance between the substrate and vegetation height (s/m), c_p is the specific heat capacity of air (J/kg K), ρ_a is the atmospheric density (kg/m^3), and T_a is air temperature at blending height (K).

Soil surface net radiation of soil portion is computed from eqn. (10).

$$R_{n\_s} = R_{s\downarrow} - \alpha_s R_{s\downarrow} + R_{L\downarrow} - R_{L\_s\uparrow} - \left(1 - \varepsilon_{o\_s}\right) R_{L\downarrow} \tag{10}$$

where R_{n_s} is net radiation of soil portion (W/m^2), $R_{s\downarrow}$ is incoming shortwave radiation (W/m^2), $R_{L\downarrow}$ is incoming longwave radiation (W/m^2), $R_{L\_s\uparrow}$ is outgoing longwave radiation of soil portion (W/m^2), and α_s is soil portion albedo.

When the surface is fully covered with vegetation, the understory aerodynamic resistance ($r_{as\ (fc\ =1))}$ between z_{os} and $d + z_{om}$ is computed as according to Choudhury and Monteith (1988) using eqn. (11).

$$r_{as(fc=1)} = \frac{h_c \exp(n)}{n\, K(h)} \left[\exp\left(\frac{-n\, z_{om}}{h_c}\right) - \exp\left[-n\left[\frac{d + z_{om}}{h_c}\right]\right]\right] \tag{11}$$

where $r_{as\ (fc=1)}$ is aerodynamic resistance between the substrate and vegetation height (s/m) of fully vegetated portion (f_c =1), z_{om} is roughness length of momentum (m), and K (h) is eddy diffusion coefficient of momentum correction.

The eddy diffusion coefficient of momentum correction (K (h)) from z_{om} to h_c has been computed using eqn. (12) (Choudhury and Monteith, 1988).

$$K(h) = \frac{k^2\, u_z\, (h_c - d)}{\ln\left(\frac{z - d}{z_{om}}\right) - \psi_{m\_30m}} \tag{12}$$

where K(h) is eddy diffusion coefficient of momentum correction, ψ_{m_30m} is stability correction of momentum for blending height, z is height of measurements of wind speed and

air temperature at blending height (m), and u_z is wind speed at blending height (m/s).

When the surface is completely bare, the aerodynamic resistance ($r_{as\ (fc=0)}$) from z_{os} to $d + z_{om}$ can be written using eqn. (13).

$$r_{as\ (fc=0)} = \frac{\left[\ln\left(\frac{z}{z_{os}}\right) - \psi_{m\_30m}\right]\left[\ln\left(\frac{d + z_{om}}{z_{os}}\right) - \psi_{h_d+zom}\right]}{k^2\, u_z} \tag{13}$$

where $r_{as\ (fc=1)}$ is aerodynamic resistance between the substrate and vegetation height (s/m) for soil portion (f_c =0), ψ_{hd+zom} is stability correction of heat from z_{om} to $d + z_{om,}$ and z_{os} is minimum roughness length (m).

Finally, aerodynamic resistance for a partial surface is computed by weighting by f_c in a parallel combination of resistances (eqn. (14)).

$$r_{as\ (int)} = \frac{1}{\frac{f_c}{r_{as(f=1)}} + \frac{1 - f_c}{r_{as(f=0)}}} \tag{14a}$$

$$r_{as\ (int)} = \frac{1}{\frac{f_c{}^m}{r_{as(f=1)}} + \frac{1 - f_c{}^m}{r_{as(f=0)}}} \tag{14b}$$

where r_{as} (int) is aerodynamic resistance between the substrate and vegetation height (s/m) of partial surface, m is an exponent on f_c where m is 0.5 or 0.2 to give more weight to the r_{as} from the vegetation component to increase r_{ah} and in turn increase T_c.

Ground heat flux of soil portion is estimated either from H_s or R_{n_s} using eqn. (15) (Allen et al., 2012). The comma in the 'max ()' function selects the maximum of the two values.

$$G_s = \max(0.4\, H_s, 0.15 R_{n\_s}) \tag{15}$$

where G_s is ground heat flux of soil portion (W/m^2).

The heat flux of water is computed using eqn. (16) (Allen et al., 2012). Surface energy balance of water portion is carried out in the soil portion of surface energy balance replacing LE_s to LE_w equation. r_{as} is assumed to be zero and r_{ah} is computed from z_{om} to blending height. The calculation procedure of r_{ah} of water portion is shown in table A.1.

$$G_w = 0.9R_{n\_s} - 40 \tag{16}$$

where G_w is heat flux of water (W/m^2).

Finally, the sensible heat flux of soil portion is computed as a residual from the surface energy balance of soil portion using eqn. (17).

$$H_s = R_{n\_s} - G_s - LE_s \tag{17}$$

where LE_s is latent heat flux of soil portion (W/m^2).

Vegetation Portion Surface Energy Balance

Outgoing long wave radiation of vegetation portion is computed using eqn. (18).

$$R_{L\_c\uparrow} = {T_c}^4 \, \sigma \, \varepsilon_{o\_c} \tag{18}$$

where $R_{L\_c\uparrow}$ is outgoing long wave radiation of vegetation portion (W/m^2), T_c is surface temperature of vegetation portion (K), and ε_{o_c} is broad band emissivity of vegetation portion.

Surface temperature of vegetation portion is computed from eqn. (19).

$$T_c = \frac{H_c \ (r_{ah} + \ r_{ac})}{\rho_a \ c_p} + T_a \tag{19}$$

where H_c is sensible heat flux of vegetation portion (W/m^2) and r_{ac} is bulk boundary layer resistance of the vegetative elements in the vegetation (s/m).

Net radiation of vegetation portion (R_{n_c}) is computed using eqn. (20).

$$R_{n\_c} = R_{s\downarrow} - \alpha_c \, R_{s\downarrow} + R_{L\downarrow} - R_{L\_c\uparrow} - \left(1 - \varepsilon_{o\_c}\right) R_{L\downarrow} \tag{20}$$

where α_c is albedo of vegetation portion and $R_{L\_c\uparrow}$ is outgoing longwave radiation of vegetation portion (W/m^2).

Sensible heat flux of vegetation portion is computed and updated as a residual using eqn. (21). It is assumed that there is no ground heat flux in the vegetated portion.

$$H_c = R_{n\_c} - T\,\lambda_c \tag{21}$$

where λ_c is latent heat flux of vaporization of vegetation portion (J/kg) and T is transpiration (mm/hr).

The bulk boundary layer resistance of the vegetative elements in the vegetation is computed using eqn. (22).

$$r_{ac} = \frac{r_b}{\frac{2\,LAI}{f_c}} \tag{22}$$

where r_{ac} is bulk boundary layer resistance of the vegetative elements in the vegetation (s/m) and r_b is mean boundary layer resistance per unit area of vegetation (s/m).

Mean boundary layer resistance per unit area of vegetation (r_b) is taken as 25 s/m (Denmead 1976, Uchijima 1976 and Shuttleworth and Wallace, 1985). rb/ 2 is mean leaf boundary layer resistance of amphistomatous leaves per unit surface vegetation (Ahuja et al, 2000). The value of r_{ac} in close vegetation is less than 10 s/m (Ahuja et al, 2000). Sensitivity showed that the surface energy flux parameters are less sensitive with r_b. r_b varied from 1 to 18 s/m with seasonal mean of 10 s/m for long leaf width corn (Farahani and Baush, 1995).

Combined Section

Monin Obukhov length is computed from the combined value of sensible heat flux (H) using eqn. (23). H is computed combining soil and vegetation portion with adjusted f_c.

$$L = -\frac{c_p T_a \rho_a {u_*}^3}{kgH} \tag{23}$$

where L is Monin Obukhov length (m), H is combined sensible heat flux (W/m^2), u_* is

friction velocity (m/s), g is acceleration due to gravity i.e. 9.81 (m/s^2), k is von Karman constant i.e. 0.41.

For computing r_{ah} from d + z_{om} to z, a standard equation of aerodynamic equation eqn. (24) is used and modified for different scenarios as in table A.1.

$$r_{ah} = \frac{\left[\ln\left(\frac{z-d}{z_{om}}\right) - \psi_{m\_30m}\right]\left[\ln\left(\frac{z-d}{Z_1}\right) - \psi_{h\_30m} + \psi_h\left(\frac{Z_1}{L}\right)\right]}{k^2\, u_z} \quad (24)$$

where ψ_{h_30m} is stability correction of heat for blending height and Z_1 is integration constant (m).

For the smooth transition of r_{ah}, integration constant (Z_1) was interpolated based on fraction of cover of vegetation (f_c). When f_c is equal to 1, Z_1 is Z_{1_full} i.e. 0.1 * z_{om}. For the partial covered area with $f_c < 0.6$, Z_1 is Z_{1_par} i.e. $h_c - d$. For smooth transition, when f_c is in between 0.6 to 1, linear interpolation is done between Z_{1_par} and Z_{1_full}.

$$Z_1 = \begin{cases} Z_{1\_full} = 0.1\, z_{om} & \text{if } f_c = 1 \\ Z_{1\_par} = h_c - d & \text{if } f_c < 0.6 \\ Z_{1\_inter} = Z_{1\_par} - \left(\frac{Z_{1\_par} - Z_{1\_full}}{1 - 0.6}\right)(f_c - 0.6) & \text{otherwise} \end{cases} \quad (25)$$

In a fully vegetated surface scenario, the transfer begins at the top of the vegetation and integration constant Z_1 is z_{oh} i.e 0.1 $z_{om.}$ Stability correction of heat integration constant i.e height (ψ_h (z_{oh}/L)) is neglected as it is small compared to other integration constants (scenario 1, table A.1). But in partially covered vegetated surface scenario, integration constant Z_1 becomes (h_c - d) which is significant i.e. ψ_h {(h_c – d)/L} and it has been included in r_{ah} equation (scenario 2, table A.1). For water bodies, d and (ψ_h (z_{oh}/L) is considered as zero (scenario 3, table A.1) as integration is done from z_{om} to blending height.

Table A.1. Computation strategy for aerodynamic resistance (r_{ah}) from vegetation height to blending height

Scenario	Cover type	d	z_{om}	Z_1	Height of measurement	$\psi_h\left(\frac{Z_1}{L}\right)$
1	Fully covered with vegetation	d	z_{om}	z_{oh}	d + z_{om} to z	Neglected
2	Partially covered with vegetation	d	z_{om}	h_c - d	d + z_{om} to z	$\psi_h\left(\frac{h_c - d}{L}\right)$
3	Water Bodies	0	z_{om}	z_{om}	z_{om} to z	0

Aerodynamic resistance (r_{ah}) for fully vegetated and partially vegetated conditions is shown in eqn. (26).

$$r_{ah} = \begin{cases} \frac{\left[\ln\left(\frac{z-d}{z_{om}}\right) - \psi_{m\_30m}\right]\left[\ln\left(\frac{z-d}{z_{oh}}\right) - \psi_{h\_30m}\right]}{k^2 u_z} & \text{if } f_c = 1 \\ \frac{\left[\ln\left(\frac{z-d}{z_{om}}\right) - \psi_{m\_30m}\right]\left[\ln\left(\frac{z-d}{h_c-d}\right) - \psi_{h\_30m} + \psi_{h\_h_c-d}\right]}{k^2 u_z} & \text{Otherwise} \end{cases} \quad (26)$$

Parameter X of stability correction for 30 m is computed from eqn. (27).

$$X_{30m} = \left[1 - 16\frac{(z-d)}{L}\right]^{0.25} \quad (27)$$

Correction of momentum for 30 m (ψ_{m_30m}) is computed from eqn. (28).

$$\psi_{m\_30m} = \begin{cases} 2\ln\left\{\left[\frac{(1+X_{30m})}{2}\right]\right\} + \ln\left[\frac{\left(1+X_{30m}{}^2\right)}{2}\right] + 2\text{atan}X_{30m} - \frac{\pi}{2} & \text{if } L < 0 \\ -5\left(\frac{30}{L}\right) & \text{Otherwise} \end{cases} \quad (28)$$

Correction of heat for 30 m (ψ_{h_30m}) is computed from eqn. (29).

$$\psi_{h\_30m} = \begin{cases} 2\ln\left(\frac{1+X_{30m}{}^2}{2}\right) & \text{if } L < 0 \\ -5\left(\frac{30}{L}\right) & \text{Otherwise} \end{cases} \quad (29)$$

Parameter X for d + z_{om} is computed from eqn. (30).

$$X_{d+zom} = \left[1 - 16\frac{(d + Z_{om})}{L}\right]^{0.25} \quad (30)$$

Correction of heat for d + z_{om} (ψ_{hd+zom}) is computed from eqn. (31).

$$\psi_{h_d+zom} = \begin{cases} 2\ln\left(\frac{1 + X_{d+zom}{}^2}{2}\right) \text{ if } L < 0 \\ -5\left(\frac{d + Z_{om}}{L}\right) \text{ Otherwise} \end{cases} \quad (31)$$

Parameter X for h_c – d is computed from eqn. (32).

$$X_{h_c-d} = \left[1 - 16\frac{(h_c - d)}{L}\right]^{0.25} \quad (32)$$

Correction of heat for h_c – d (ψ_{hhc-d}) is computed from eqn. (33).

$$\psi_{h\_h_c-d} = \begin{cases} 2\ln\left(\frac{1 + X_{h_c-d}{}^2}{2}\right) \text{ if } L < 0 \\ -5\left(\frac{h_c}{L}\right) \text{ Otherwise} \end{cases} \quad (33)$$

References

Ahuja, L., Rojas, K. W. and Hanson, J. D., 2000. Root Zone Water Quality Model: Modelling Management Effects on Water Quality and Crop Production. Water Resources Publication.

Farahani, H.J., & Bausch, W.C., 1995. Performance of Evapotranspiration models for maize –bare soil to closed canopy. Transactions of the ASAE, 38(4), 1049-1059.

Denmead, O.T., 1976. Temperate Cereals. In: J.L. Monteith (Editor), Vegetation and the Atmosphere, Vol. 2. Academic Press, London, pp. 1—33.

Uchijima, Z., 1976. Maize and rice. Vegetation and the Atmosphere Vol. 2, J. L. Monteith (Eds.), 33-64.